Dissertation zur Erlangung des Doktorgrades

der Fakultät für Chemie und Pharmazie

der Ludwig-Maximilians-Universität München

CD44 signaling in Müller cells affects photoreceptor function and survival in healthy and diseased retinas

Monika Ayten (geb. Dinauer)

aus

Marktoberdorf, Deutschland

2023

Erklärung

Diese Dissertation wurde im Sinne von § 7 der Promotionsordnung vom 28. November 2011 von Frau Prof. Dr. Susanne Friederike Koch betreut.

Eidesstattliche Versicherung

Diese Dissertation wurde eigenständig und ohne unerlaubte Hilfe erarbeitet.

München, 21.07.2023

Monika Ayten

……

(Monika Ayten)

Dissertation eingereicht am 25.07.2023

1. Gutachterin: Prof. Dr. Susanne Friederike Koch
2. Gutachter: Prof. Dr. Martin Biel

Mündliche Prüfung am 05.10.2023

Acknowledgements

I would like to begin by expressing my gratitude to my supervisor, Prof. Susanne Koch, who has given me this opportunity and believed in me. She has accompanied me on this journey, provided guidance, and encouraged me when needed. I've thoroughly enjoyed being part of her research group and engaging in stimulating scientific discussions. Apart from that I've also cherished the moments outside of the lab, our conversations, and the shared laughter – something we both seem to excel at!

Furthermore, I would also like to take this opportunity to thank my research group colleagues Jacqueline, Hanaa, Nundi, Felia, and Michelle. They have always been there, whether it was for scientific exchange, help in the lab, or simply enjoying some lighthearted moments together. Moreover, they have always been ready to lend a sympathetic ear when it was needed.

Additionally, I would like to extend my thanks to my examination committee for their critical evaluation of my doctoral thesis and their participation in my examination.

I would also like to express my gratitude to Susi, who have been there in the background, always willing to offer words of encouragement. I am thankful for your friendship, understanding, and the positive energy you bring into my life.

At this moment, it's finally time to express my heartfelt gratitude to my parents, Isolde and Helmut. They have consistently supported my decisions and have been there for me throughout my life. I am forever grateful for their unwavering love and presence. Their sacrifices and belief in me have shaped who I am today, and I owe them a debt of gratitude that words cannot fully express. Thank you, Mom and Dad, for everything you have done for me. I would also like to thank my siblings Stefanie and Konrad, for the fact that I can always rely on them, no matter what.

A special thanks is also dedicated to my grandma, as she has always been a very important part of my life and supported me in every possible way.

I would also like to thank my parents-in-law, Meral and Edi, who have been companions and sources of encouragement for years. They have become incredibly important in my life, and I am very grateful for my second family.

Now, I would like to express my deepest gratitude to the most significant person in my life: Yasin, my husband, best friend, supporter, listener, and backbone of my life. From the very beginning, he has supported me wholeheartedly and encouraged me to move to Munich. He celebrated every high with me and stood by my side through every low. I'm thankful for his unwavering belief in me, even when I doubted myself. His faith in my abilities has been a driving force in my personal growth. Thank you for being my anchor, I cherish you more than words can express.

Table of Contents

List of Figures

List of Tables

Abbreviations

ANOVA	Analysis of variance
Arr3	Cone arrestin
ATP	Adenosine triphosphate
BC	Bipolar cell
Bp	Base pair
cDNA	Complementary DNA
cGMP	Cyclic guanosine monophosphate
CNG	Cyclic nucleotide-gated
CNS	Central nervous system
DNA	Desoxyribonucleic acid
ddH_2O	Double-distilled water
EAAT	Excitatory amino acid transporter
ECM	Extracellular matrix
ECS	Extracellular solution
ERG	Electroretinogram
GAPDH	Glyceraldehyde 3-phosphate dehydrogenase
GCL	Ganglion cell layer
GDP	Guanosine diphosphate
GFAP	Glial fibrillary acidic protein
GLT	Glutamate transporter
GLUL	Glutamine synthetase
GLUT	Glucose transporter
GMP	Guanosine monophosphate
GTP	Guanosine triphosphate
h	hour
HA	Hyaluronic acid

IL-6	Interleukin-6
ILM	Internal limiting membrane
INL	Inner nuclear layer
IPM	Interphotoreceptor matrix
IS	Inner segments
kDa	Kilodalton
KG	α-ketoglutarate
LC-MS	Liquid chromatography mass spectrometry
MACS	Magnetic-activated cell sorting
MC	Müller cell
min	minute
NF-κB	Nuclear factor kappa B
OLM	Outer limiting membrane
ONL	Outer nuclear layer
OPL	Outer plexiform layer
OSs	Outer segments
OXPHOS	Oxidative phosphorylation
PBS	Phosphate-buffered saline
PCR	Polymerase chain reaction
PDE	Phosphodiesterase
PEP	Phosphoenolpyruvate
PFA	Paraformaldehyde
PKC-α	Protein kinase C-alpha
PKM2	Pyruvate kinase M2
pw	Postnatal week
qRT-PCR	Quantitative real-time PCR
RFU	Relative fluorescence unit

RGC	Retinal ganglion cell
RHO	Rhodopsin
RNA	Ribonucleic acid
RP	Retinitis pigmentosa
RPE	Retinal pigment epithelium
SCGN	Secretagogin
SDS-PAGE	Sodium dodecyl sulfate-polyacrylamide gel electrophoresis
sec	second
ST	$Pde6b^{STOP}$
TAE	Tris-acetate-EDTA buffer
TBS	Tris-buffered saline
TCA cycle	Tricarboxylic acid cycle
TNFα	Tumor necrosis factor α
WT	Wildtype

Summary

Retinitis pigmentosa (RP), a group of inherited retinal disorders, is characterized by progressive degeneration of photoreceptor cells and several other pathological changes. For example, Müller cells, the main macroglia cells in the retina, undergo reactive gliosis. Gliotic Müller cells exhibit impaired supportive functions, such as glutamate uptake, and increased levels of CD44. CD44, a cell surface transmembrane glycoprotein, is preferentially localized in the microvilli of Müller cells and the receptor for hyaluronic acid. However, the function of CD44 in RP is not known.

We validated that CD44 was upregulated in Müller cells from several RP mouse models. To gain a more detailed understanding of CD44's role in healthy and diseased RP retinas, we analyzed *Cd44*$^{-/-}$ and *Cd44*$^{-/-}$ *Pde6b*$^{STOP/STOP}$ mice, respectively. The morphological characterization revealed that the loss of CD44 in both healthy and diseased retinas had detrimental effects on retinal morphology. Specifically, CD44 ablation led to a decreased outer nuclear layer thickness, shorter cone inner and outer segments, inner retinal remodeling, reduced retinal function, and increased inflammatory response. Additionally, proteomic analysis showed that the glutamate transporter 1 (EAAT2) was significantly downregulated in the Müller cell fraction from *Cd44*$^{-/-}$ and *Cd44*$^{-/-}$ *Pde6b*$^{STOP/STOP}$ mice compared to *Cd44*$^{+/+}$ and *Pde6b*$^{STOP/STOP}$ mice, respectively. This downregulation of EAAT2 was accompanied by higher glutamate levels, suggesting impaired glutamate homeostasis. Glutamate, as an important energy substrate, is closely linked to photoreceptor metabolism, and, in this context, we observed that PKM2, a key enzyme in glycolysis, was upregulated in photoreceptors of both *Cd44*$^{-/-}$ and *Cd44*$^{-/-}$ *Pde6b*$^{STOP/STOP}$ retinas.

These novel findings demonstrate the significance of CD44 in maintaining retinal health and protecting photoreceptor cells from degeneration in the context of RP.

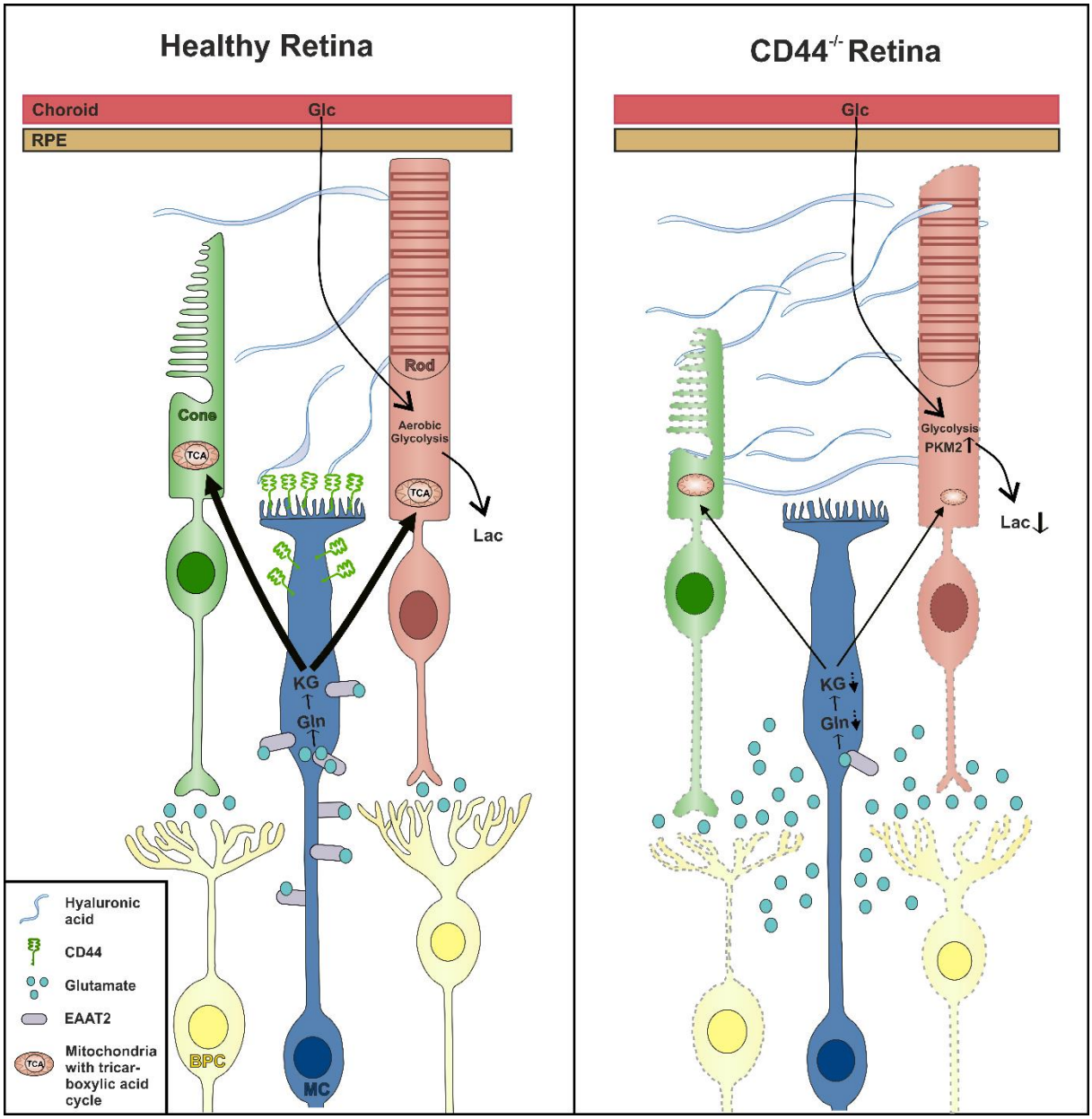

Fig. 1: Graphical Abstract

1 Introduction

1.1 Neuronal organization of the retina

Vision, as one of the five senses, is widely regarded as the most crucial [1], which is why maintaining a healthy and properly functioning eye is of utmost importance. Vision begins with the conversion of light energy from photons into electrochemical stimuli in the retina, a tissue that comprises a variety of different neuronal cell types. The retina has a layered structure, with light-sensitive rod and cone photoreceptors located in the outermost part, the outer nuclear layer (ONL), next to the retinal pigment epithelium (RPE) and choroidal blood vessels. Rods are highly sensitive to light and therefore responsible for vision under dim-light conditions (scotopic vision), while the cone photoreceptors are essential for daylight vision and critical for visual acuity and color discrimination (photopic vision). The inner nuclear layer (INL) contains rod and cone bipolar cells, horizontal cells, glial cells, and amacrine cells. Here, the visual signal detected by the photoreceptors is transmitted to the bipolar cells. This signaling is modulated by horizontal cells, which provide inhibitory feedback to rods, cones and bipolar cells [2]. The amacrine cells in turn mediate signals from rod bipolar cells via cone bipolar cells to ganglion cells, which then form the innermost retinal layer (**Fig. 2**). The bundled axons of retinal ganglion cells form the optic nerve and eventually transmit the detected light signal to the brain. The glial cells localized in the INL include three different cell types, namely astrocytes, Müller cells, and microglia, which are involved in maintaining retinal homeostasis [3–7]. Microglia are the primary resident immune cells of the retina and distributed in a ramified state within the plexiform layers [8]. Each of these cell type-specific tasks requires a different amount of energy, which makes the retina an extremely metabolically active organ. At the same time, it is also highly susceptible to inadequate oxygen and metabolite supply, which is why metabolism is closely linked to neuronal function and the survival of retinal neurons [9, 10].

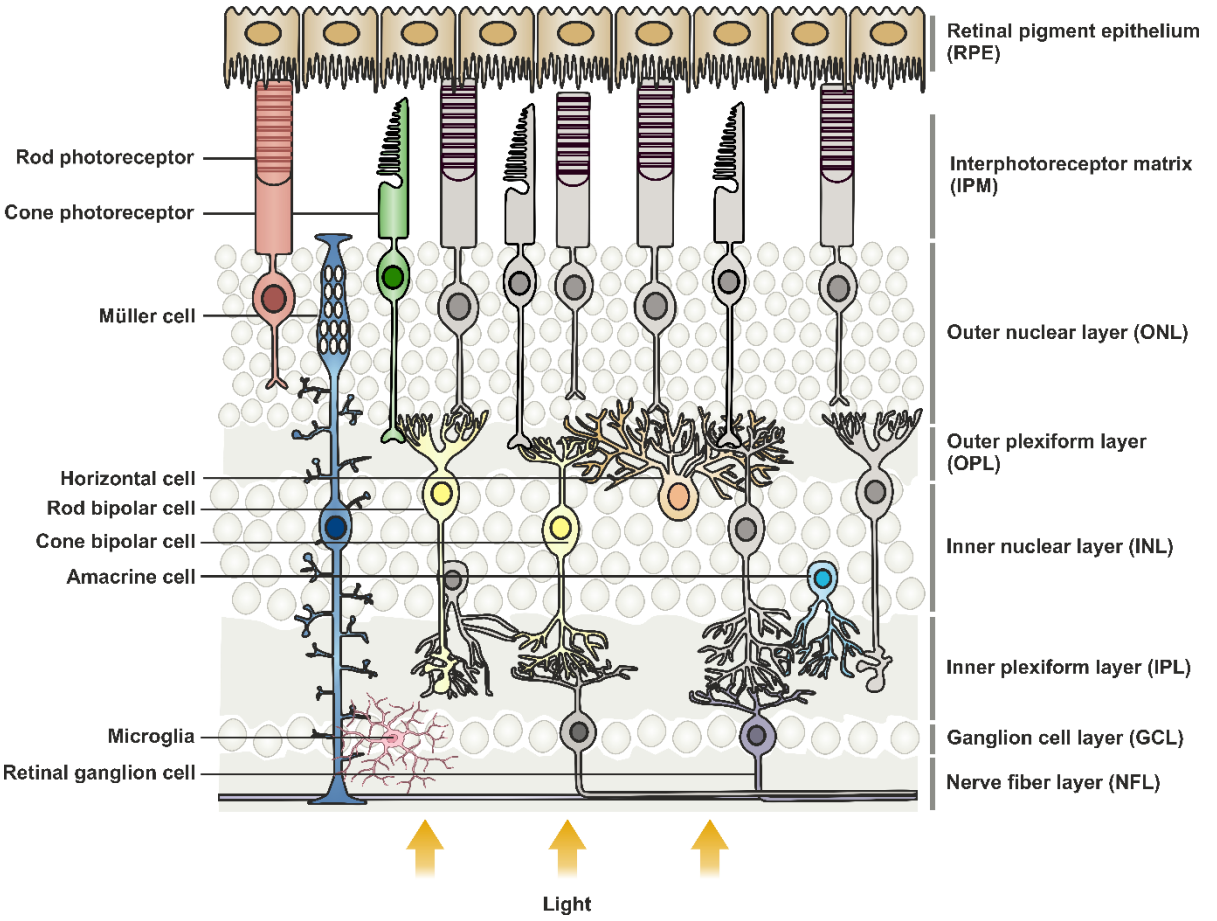

Fig. 2: Schematic representation of the multilayered retina.
The retina is located at the back of the eye, and is responsible for visual processing, converting light energy into neuronal signals that are sent to the brain to create images. It has a multilayered structure, as it contains three layers of cell bodies, the outer nuclear layer (ONL), the inner nuclear layer (INL), and the ganglion cell layer (GCL), as well as two layers of synapses, the outer plexiform layer (OPL) and inner plexiform layer (IPL). The retina also consists of many different cell types such as the photoreceptors (rods and cones), rod and cone bipolar cells, horizontal cells, amacrine cells, glial cells (Müller cells and microglia), and ganglion cells.

1.1.1 Retinal Energy Metabolism

The retina has a very high metabolic demand, which is composed of a high catabolic demand of the photoreceptors for sustaining the dark current on the one hand and an exceptionally high anabolic energy demand on the other hand. This is because rod and cone photoreceptors must daily renew the outermost part of their outer segments (OSs). This renewal includes the shedding of the OSs and the subsequent formation of new OS discs, which requires many lipids and proteins to maintain adequate OS length.

Those energy requirements are met almost exclusively by glucose supplied by the choroidal blood vessels, adjacent to the retinal pigment epithelium (RPE). Glucose diffuses from the choroid through the monolayered RPE and the interphotoreceptor matrix (IPM) [11] to the photoreceptors. This

nutrient transport is facilitated by glucose transporters (GLUTs) expressed in RPE cells, and photoreceptors. In the photoreceptors, glucose is used to produce lactate in the presence of oxygen, which is also known as aerobic glycolysis (Warburg effect). Glycolysis generates much less adenosine triphosphate (ATP) than oxidative phosphorylation (OXPHOS), but photoreceptors rely on glycolysis because of their strong need for anabolic intermediates formed during this process [12, 10]. It has been suggested that in healthy retinas, RPE cells use photoreceptor-produced lactate as fuel to minimize their consumption of glucose, and thus maximize the passage of glucose from the choroidal blood to the photoreceptors [10, 13, 14]. Furthermore, in addition to RPE cells, Müller cells also utilize lactate as an energy source and introduce it into the tricarboxylic acid (TCA) cycle and OXPHOS for ATP production (**Fig. 3**) [14, 15, 10].

Photoreceptors, RPE, and Müller cells are structurally, functionally, and metabolically coupled, and dependent on each other for survival. In fact, it has been shown that small deviations from this finely tuned and close metabolic interaction between photoreceptors and RPE can lead to massive changes and even starvation and death of photoreceptors. For this reason, alterations and dysregulations of retinal metabolism contribute to the development of various retinal diseases such as age-related macular degeneration, diabetic retinopathy and also inherited retinal degenerations such as retinitis pigmentosa (RP) [10, 13, 16, 17].

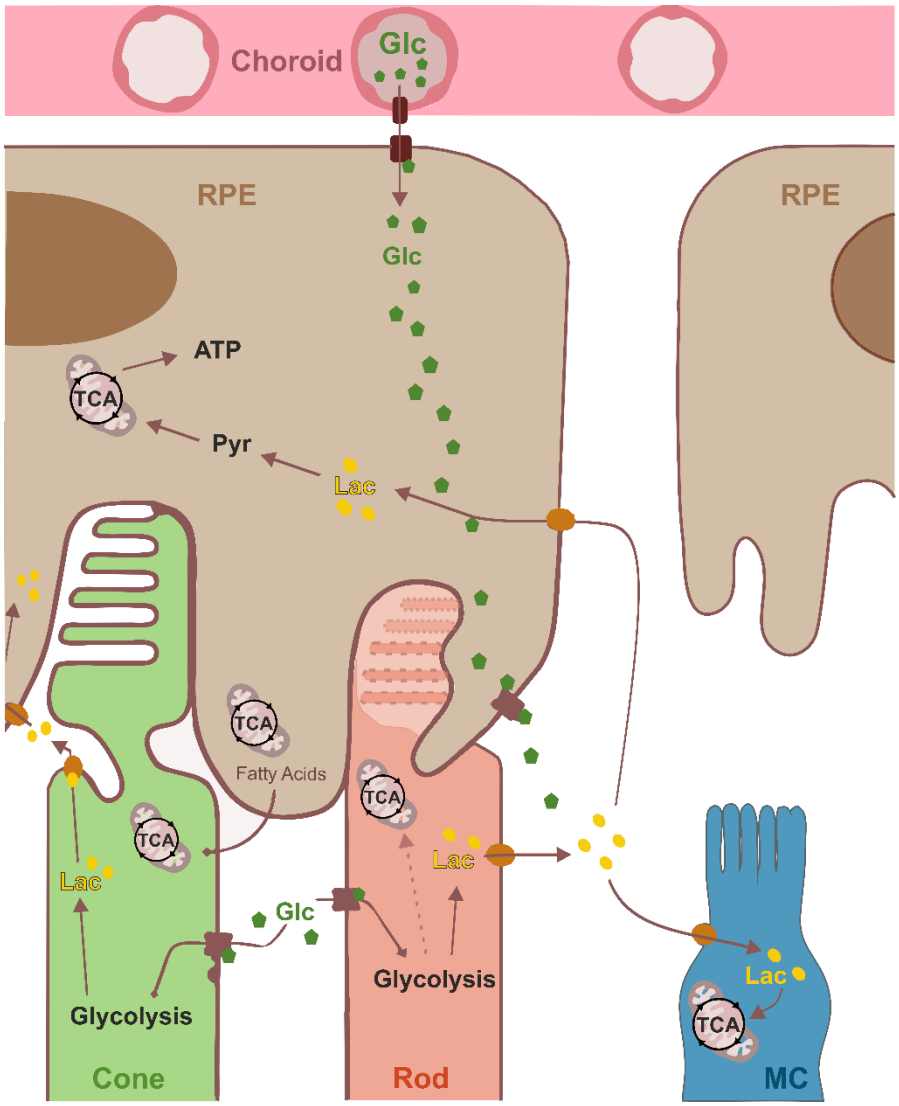

Fig. 3: Schematic drawing of the metabolic landscape between choroid, RPE, photoreceptors and Müller cells in the vertebrate retina.

Glucose (Glc) is transported from the choroidal blood vessels to the retinal pigment epithelium (RPE) and shuffled unmetabolized to the photoreceptors. Glucose is taken up via GLUT1 transporters and converted to lactate (Lac) via aerobic glycolysis, which also generates anabolic intermediates for outer segment (OS) renewal. Lactate from aerobic glycolysis is transported by photoreceptors into the interphotoreceptor matrix (IPM), where it is taken up by Müller cells (MC) and RPE cells. Lactate can be reconverted to pyruvate (Pyr) and serve as a fuel for the tricarboxylic acid (TCA) cycle and oxidative phosphorylation (OXPHOS) to generate adenosine triphosphate (ATP) in MC and RPE cells. Additionally, RPE cells supply photoreceptors with fatty acids, that can be metabolized in the mitochondria and support TCA cycle and OXPHOS.

1.1.2 Visual phototransduction and intraretinal signal processing

Patients with photoreceptor degeneration suffer from impaired visual function due to disturbed phototransduction, the process transducing light into electrochemical stimuli. The phototransduction cascade takes place in the outer segments of rod and cone photoreceptors (**Fig. 4**). In cones, it begins with the long, middle or short wavelength-sensitive cone opsin [18]. In rods, it starts with the photopigment rhodopsin, which is highly abundant in the outer segment disc membranes and consists of the protein opsin and the chromophore 11-*cis*-retinal. Once a photon reaches the outer retina, it is absorbed by rhodopsin, leading to the isomerization of 11-*cis*-retinal to all-*trans*-retinal. This triggers conformational changes of opsin leading to its active state metarhodopsin II. Metarhodopsin II activates the heterotrimeric G-protein transducin by catalyzing the exchange of bound guanosine diphosphate (GDP) with guanosine triphosphate (GTP) on transducin's α-subunit (Tα-GTP). Subsequently, the complex dissociates into Tα-GTP and the remaining βγ-subunit. Tα-GTP now interacts with PDE6, a tetrameric protein that consists of the similar catalytic subunits α and β and two identical γ subunits. Tα-GTP stimulates PDE6 activity by binding to its inhibitory γ-subunit, which is subsequently displaced from the active site of PDE6, activating the protein and consequently hydrolyzing cyclic guanosine monophosphate (cGMP) to GMP. The decrease of cGMP concentration in the photoreceptor cytoplasm leads to closure of the cyclic nucleotide-gated (CNG) ion channels located in the rod plasma membrane of the OSs. Closure of CNG channels stops the Na^+ and Ca^{2+} ion influx and causes hyperpolarization of the cell. The hyperpolarization is a graded effect and is determined by the amount of light absorbed and the number of activated visual pigments. A minor decrease in cGMP concentration causes the closure of some CNG channels, whereas a large decrease eventually leads to the closure of all channels, resulting in rod cell saturation. The hyperpolarization relays visual information generated at the OSs to the synaptic terminals of photoreceptors, where it reduces the release of the neurotransmitter glutamate from the synaptic terminals and signals the presence of light to bipolar cells [19–21]. Cones form synapses onto two different types of bipolar cells, the ON bipolar type, which depolarizes in response to light, and the OFF bipolar, which hyperpolarizes in light. On the other hand, rods connect to only one rod bipolar cell type, which is a depolarizing ON, bipolar cell type. After an increase in light intensity, glutamate release drops and activated ON and OFF cone bipolar cells directly excite ON and OFF ganglion cells, respectively. In contrast, activated rod bipolar cells stimulate amacrine cells, which in turn connects to the two cone bipolar cell types and convey the signal to ganglion cells. Once the ganglion cells are activated, their axons transmit the signal to the brain [22] .

In the dark, a so-called dark current is maintained in rods since high concentrations of cytoplasmic cGMP keep the CNG channels open. This allows Na^+- and Ca^{2+}-ions to move into the outer segments

which cause a depolarization and a membrane potential of -40 mV. In this state, rods continually release their neurotransmitter glutamate into the synaptic cleft [19, 23–25].

The precise regulation of cGMP levels is essential for normal functioning of the visual transduction cascade, which is why a persisent imbalance in cGMP metabolism disrupts the visual signaling pathway and eventually leads to photoreceptor cell death and retinal degeneration (e.g. retinitis pigmentosa) [26].

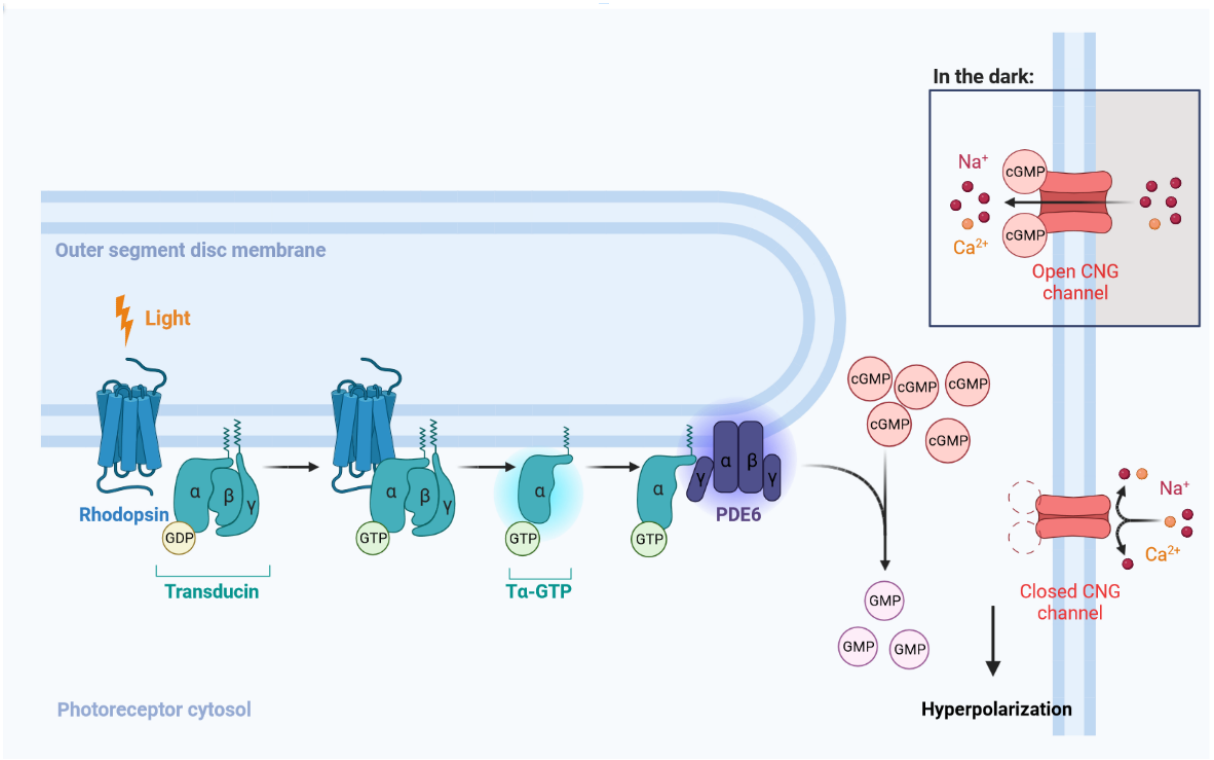

Fig. 4: Visual phototransduction cascade in rod photoreceptors.
The photopigment rhodopsin, GDP-bound transducin, and phosphodiesterase 6 (PDE6) are located at the disc membranes of rod photoreceptor outer segments. In the dark, the cyclic nucleotide-gated (CNG) channels are open leading to a constant Na^+- and Ca^{2+}-influx that causes rod photoreceptor depolarization. Under light conditions, photons are absorbed by rhodopsin, which undergoes a conformational change and activates GDP-bound transducin. The activated α-subunit of transducin (Tα-GTP) binds to PDE6, which hydrolyzes cGMP to GMP. The lower intracellular levels of cGMP cause the closure of CNG channels and results in hyperpolarization of the cell. Created in BioRender.com

1.2 Retinitis pigmentosa

Retinitis pigmentosa (RP) is the most common inherited retinal disorder with a worldwide prevalence of 1:4000 [27, 28]. RP is characterized by initial night blindness, due to degeneration of rod photoreceptors and, after several years, loss of daylight vision due to secondary cone dysfunction [27].

1.2.1 Genetic alterations

Mutations in more than 80 different causative genes can lead to RP [27], which illustrates the genetic heterogeneity of the disease. RP can be inherited in an autosomal dominant, autosomal recessive, X-linked or mitochondrial manner [29–32]. While RP in a non-syndromic form of the disease is limited to the eye, there are also syndromic forms that affect multiple organs [31]. The underlying mutations can affect a variety of genes with different functions in the retina. For example, genes involved in phototransduction, cell trafficking, rhodopsin recycling, structural and transmembrane proteins or transcription factors may be affected [28, 29]. Most mutant genes are expressed in the rod photoreceptors, leading to their progressive death [33, 29]. Although cone photoreceptors are not affected by the mutation, they also degenerate at late stages of the disease, leading to complete blindness [28, 34].

The gene encoding the β-subunit of PDE6 (PDE6B) was one of the first genes identified as a cause of autosomal recessive RP in humans [35], accounting for approximately 4 % of cases [36].

1.2.2 Symptoms and disease progression

RP is a variable disorder, with some patients developing vision loss in childhood, while others remain asymptomatic into adulthood. In most cases, RP typically manifests with night blindness in adolescence and subsequent loss of peripheral vision in young adulthood. These symptoms reflect the functions of the rod photoreceptors, as they degenerate first. As the disease progresses, the visual field narrows further, resulting in tunnel vision, and in the final stages of the disease, central vision is eventually lost due to cone degeneration, leading to blindness. In fact, it is the secondary cone loss that leads to color and daylight vision loss and can affect one's quality of life [28, 37, 38, 27].

1.2.3 Retinal remodeling

In RP the loss of rod and cone photoreceptors, leads to progressive structural and functional changes in inner retinal neurons and glia cells, known as retinal remodeling. The remodeling consists of three phases. Phase I is the pre-degeneration period, characterized by an initiation of photoreceptor stress and delocalization of visual pigments.

During phase II, photoreceptor death is accompanied by glial remodeling. The signature event of phase II is the formation of thick membranes, also known as "glial scars", by Müller cell processes and proliferated astrocytes and microglia onto both retinal surfaces. In the subretinal space Müller cell processes grow through the outer limiting membrane (OLM) where they form a subretinal scar that

isolates the retina from the RPE and choroid [39–42]. In addition, the bipolar cell dendrites shorten massively, resulting in loss of glutamatergic input. As long as cones or remnants of cone cell bodies are present, the cone bipolar cells remain.

Phase III is characterized by life-long remodeling that changes the basic topology of the retina by migration of bipolar and amacrine cells into the ganglion cell layer. In addition to migration events, there are also neuronal morphologic changes and neuronal cell death, vascular remodeling, altered glial metabolism, and RPE invasion into the neural retina [40, 43–46]. Overall, neuronal remodeling and glial seal formation may defeat therapies. A promising finding in this context is that retinal injury in lower vertebrates causes a subset of Müller cells to differentiate into neural progenitor cells that replenish lost photoreceptors and other neurons, thereby restoring vision [46–48]. This emphasizes the importance of expanding our knowledge of Müller cell function and responses in both healthy and diseased retinas. Such an understanding could have important implications for the development of novel therapeutic approaches for the treatment of retinal diseases.

1.3 Müller cells in healthy and diseased retina

There are two types of glial cells in the mammalian retina, microglia and macroglia, and macroglia can be divided into astrocytes and Müller cells. Müller cells are the principal and most common glial cell in the retina of vertebrates and play key roles in supporting neuronal functions [49–51, 8].

1.3.1 Morphology of Müller cells

Müller cells have a unique, cylindrical, and fiber-like morphological structure and span the entire thickness of the retina. The somata of Müller cells are located in the inner nuclear layer (INL) and the two processes radiate from there in two opposite directions (**Fig. 5**). The end feet of Müller cells create the internal limiting membrane (ILM), which is the boundary between the retina and the adjacent vitreous. On the opposite side, the apical part of the Müller cells forms the OLM. The OLM is located between the ONL and the inner segments of the photoreceptors. In addition, the apical processes have numerous microvilli that extend into the subretinal space. Müller cells also possess many complex side branches, establishing connections with all other cell types within the retina (**Fig. 5**).

Considering that the human retina contains 4 to 5 million Müller cells and their close proximity and interactions with other retinal cell types, it is important to further investigate the functions of these glial cells [49, 50, 52–54].

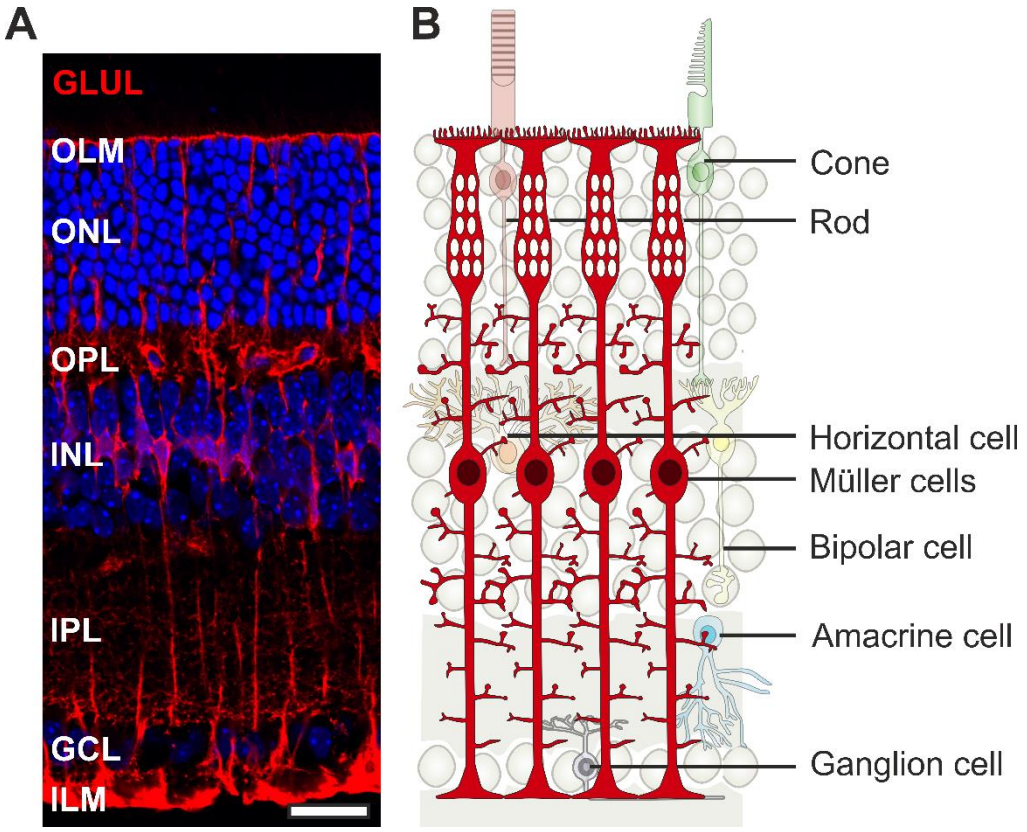

Fig. 5: Müller cells in the vertebrate retina.
(A-B) Müller cells in the vertebrate retina form a dense and regular pattern. They have an elaborate radial morphology, span the entire retinal thickness, and interact with all retinal cell types. **(A)** Representative image of retinal section immunostained for glutamine synthetase (GLUL) to visualize Müller cells. Müller cell processes form the outer limiting membrane (OLM) and the internal limiting membrane (ILM). Scale bar, 20 µm. **(B)** Schematic drawing of Müller cells (red) in the retina. The morphology is characterized by vertical processes, that span throughout the retina. The ILM is formed by Müller glia end feet and separates the retina from the vitreous. The OLM is a cellular structure composed of junctional complexes between Müller cells and photoreceptor inner segment plasma membranes. Müller cells have numerous apical microvilli and horizontal branches that enable interaction with other retinal cell types.

1.3.2 Role of Müller cells in retinal physiology

Müller cells have a wide variety of tasks to perform. This begins with retinal development, as Müller cells are essential for the guidance and maintenance of cellular organization throughout the retina. Although they are the last cell types to differentiate in retinal development (**Fig. 6**), they are crucial for the proper wiring of the neuronal circuits and for maintaining neuroretinal architecture. The absence of Müller glial cells during development leads to retinal disorganization and photoreceptor migration into the subretinal space [50, 55, 56].

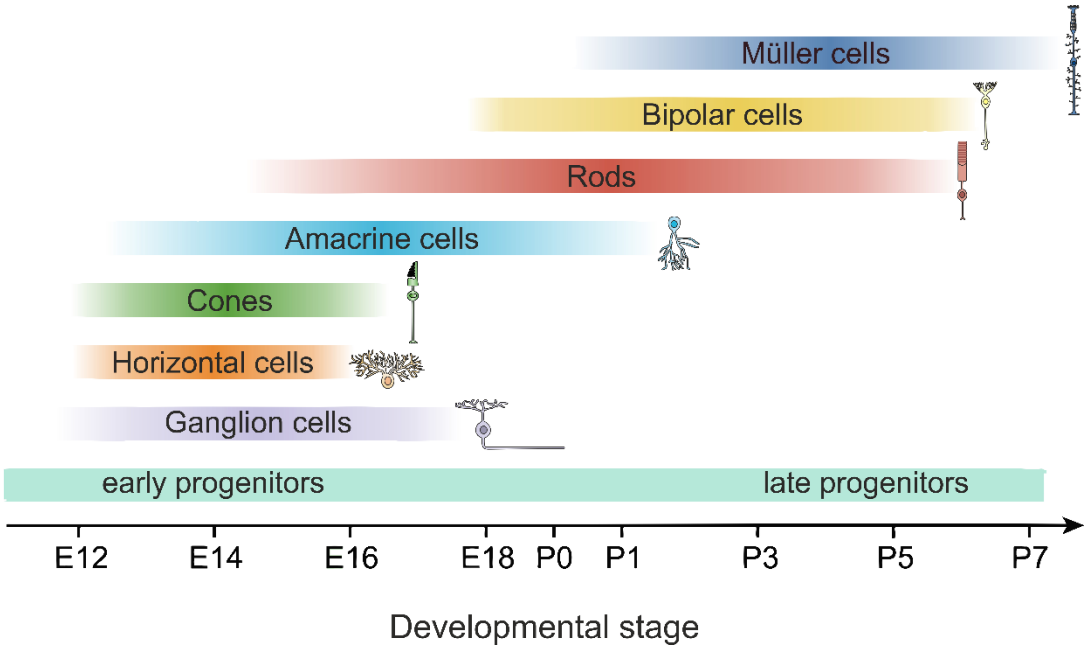

Fig. 6: Developmental timeline of cell fate determination in the vertebrate retina.
Multipotent progenitor cells sequentially become retinal cells during development. Early retinal progenitors first produce retinal ganglion cells, followed by cone photoreceptors, horizontal cells, and amacrine cells in an overlapping manner. These cells are formed before birth (embryonic phase). In the postnatal phase, late retinal progenitors produce most of the rod photoreceptors, bipolar cells, and lastly Müller cells.

After maturation, Müller cells play a crucial role in maintaining retinal potassium homeostasis due to the expression of numerous K^+ channels (Kir4.1) on their plasma membrane, which renders them highly permeable to K^+. This potassium uptake and regulation by Müller cells is very important, because even slight changes in potassium concentration can disrupt the retinal microenvironment and affect the excitability of bipolar cells [50, 57–59]. Together with the K^+ channels, Müller cells express aquaporin-4 water channels. This co-expression led to the assumption that Müller cells can compensate for osmotic differences between the retina, blood, and vitreous by simultaneous in- or effluxes of water and K^+. Additionally, the aquaporin channels present in Müller cells facilitate the removal of excess water from the inner retinal tissue. This is necessary because water accumulates in the retina due to its influx from the blood vessels and the vitreous humor. By facilitating the efficient removal of water, Müller cells actively contribute to the maintenance of adequate hydration levels within the retina. This mechanism ensures optimal retinal function and helps prevent the occurrence of edema or swelling [50].

Müller cells also play a very important regulatory role in neurotransmitter recycling and thereby supporting the synaptic activity. Glutamate is the main excitatory neurotransmitter in the retina, released from rod photoreceptors into the outer retina in darkness (chapter 1.1.2). There are also two types of bipolar cells that release glutamate in the inner retina: the ON-bipolar cells release the

neurotransmitter during light exposure and the OFF-bipolar cells secrete glutamate in the dark. This glutamate release is essential for intact transmission of the visual signal to the brain, but if reuptake is impaired, glutamate can accumulate leading to excitotoxicity. To circumvent this and keep glutamate levels at bay, Müller cells express high-affinity glutamate transporters (GLT), so-called excitatory amino acid transporters (EAATs). This enables them to take up glutamate, particularly in the inner retina [60, 61]. After entering the Müller cell, glutamine synthetase (GLUL), a Müller cell-specific enzyme, rapidly converts glutamate to glutamine by amidation. Glutamine is subsequently released from Müller cells and taken up by presynaptic neurons, deaminated to glutamate by phosphate-activated glutaminase (PAG) and stored in synaptic vesicles. This glutamate-glutamine circuit is necessary to protect retinal neurons from excitotoxicity and to recycle glutamate, to maintain a neurotransmitter reservoir [61, 62]. In addition, glutamate itself can also serve as fuel for Müller cells and retinal neurons, as they are able to convert glutamate into α-ketoglutarate (α-KG). α-KG, an intermediate of the TCA cycle, plays a crucial role in increasing mitochondrial ATP production and is also utilized by photoreceptors in periods of metabolic stress (**Fig. 7**) [60, 61, 10]. This plethora of different tasks, including their architectural and metabolic support functions, demonstrate that Müller cells play an important role in maintaining retinal homeostasis. If these finely tuned processes are disturbed, either by changes in the Müller cells themselves or by neuronal degeneration leading to gliotic Müller cells, this has an impact on the overall retinal health [49].

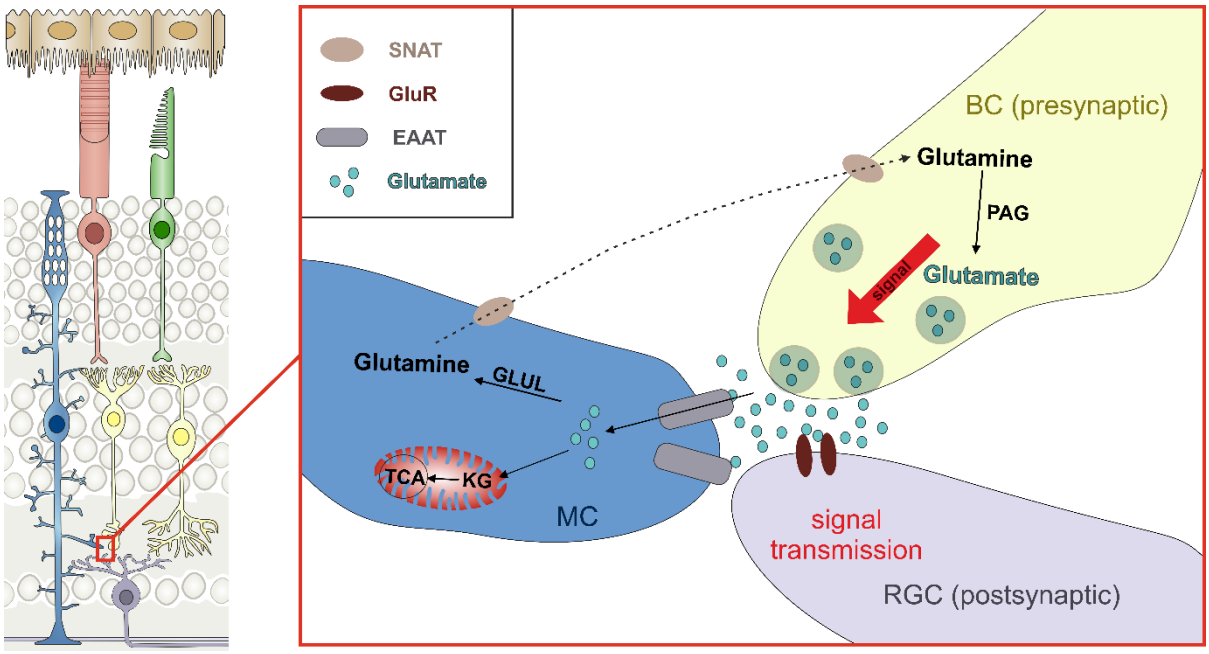

Fig. 7: Schematic drawing of the contribution of Müller cells to glutamate homeostasis in the inner retina of vertebrates.
The excitatory neurotransmitter glutamate is released from neurons in the inner retina, e.g., bipolar cells (BC) and stimulates glutamate receptors (GluR) at postsynaptic retinal ganglion cells (RGC). Müller cells reuptake the free glutamate from the synaptic cleft by excitatory amino acid transporters (EAATs). The ingested glutamate is then converted to glutamine by glutamine synthetase (GLUL) and transported back to the neurons via sodium-coupled neutral amino acid transporters (SNATs). Back in the neurons, glutamine is reconverted to glutamate by phosphate-activated glutaminase (PAG) and stored in synaptic vesicles. Additionally, glutamate also serves as source of energy for Müller cells and neurons, as it can be converted to α-ketoglutarate (KG) and drives the tricarboxylic acid (TCA) cycle to generate ATP.

1.3.3 Alterations of Müller cells in the diseased retina

In response to retinal injury or under disease conditions, Müller cells are one of the first cells in the retina to respond by becoming activated a process termed gliosis. The release of cytokines from activated microglia can initiate this Müller cell activation [39, 63]. Reactive Müller cell gliosis can lead to unspecific or specific reactions to pathogenic stimuli including morphological, biochemical, and physiological changes of Müller cells. While the specific response may vary depending on the insult, there are usually three unspecific independent responses. The most common one is the upregulation of intermediate filaments such as glial fibrillary acidic protein (GFAP), Vimentin, and Nestin. GFAP is virtually not expressed in the healthy Müller cells, and is immediately upregulated in response to stress, making GFAP a good and highly sensitive marker for a variety of retinal injuries and diseases. The other most prominent unspecific gliotic responses are the Müller cell hypertrophy and proliferation [64–67].

Reactive gliosis has both Müller cell-mediated supportive effects on neuronal survival and cytotoxic effects on retinal neurons. The gliotic response, particularly in the early post-injury period, is thought to be neuroprotective as Müller cells can compensate for increased potassium levels, uptake excess glutamate which is neurotoxic and secrete antioxidants, growth factors, and neurotrophic factors that promote photoreceptor survival [67].

On the other hand, Müller cell gliosis may also contribute to retinal neurodegeneration especially at later stages or in more severe cases of reactive gliosis, when the blood-retinal-barrier breaks down [67]. This contribution can be caused by many different pathways, for instance the release of the proinflammatory cytokines tumor necrosis factor α (TNFα), nuclear factor kappa B (NF-κB) or interleukin-6 (IL-6) [67–70]. Furthermore, an impairment of glutamate removal is described leading to excitotoxic effects on neurons. In addition, edema may result from downregulation of the Kir4.1 potassium channels and aquaporins, which inhibits the removal of K^+ and water, and therefore leads to swelling of glia and thus impeding glio-neuronal interaction and promoting edema development [67, 71].

Furthermore, it has been shown that the interplay of Müller cells and microglia can also have detrimental consequences for CNS neurons. In degenerative states Müller cells and microglia can send mutual and reciprocal signals that amplify local inflammation in a positive feedback cycle [63, 72].

In the last stage of retinal remodeling, Müller cells and Microglia re-enter the proliferation cycle and form glial scars (chapter 1.2.3), which are the main reason why the central nervous system is not able to regenerate [50, 64, 39].

All these gliotic changes in Müller cells may be detrimental to photoreceptor survival and may additively exacerbate existing disease. Many different RP forms are also associated with changes of microglia and macroglia cells. In some, increased microglial activity and gliosis is seen even before the characteristic onset of photoreceptor degeneration [73–75]. Considering the fact that damaged Müller cells in lower vertebrates are able to regenerate into functional neurons, whereas mammalian Müller cells cannot [70, 76, 77], and that Müller cells play a key role in maintaining the integrity, function and survival of retinal neurons, it is important to expand our knowledge of common cellular alterations in Müller cells in the context of inherited retinal diseases.

1.4 Upregulation of CD44 protein expression in Müller cells of RP mouse models

Müller cells respond to retinal degeneration by undergoing reactive gliosis. Additionally, it has been reported that the expression of CD44 antigen (CD44), a Müller cell specific protein, is dramatically increased in retinas of the retinal degeneration slow (rds) mouse model, after onset of photoreceptor degeneration [78, 79].

1.4.1 CD44 structure and physiological functions

The CD44 gene is located on chromosome 11 and comprised of 19 exons in humans, whereas in mice the gene is located on chromosome 2 (20 exons). There are several variant isoforms of CD44, but the standard isoform of CD44 with 85-95 kDa is encoded by the first five and last five exons and is found in various tissues including the CNS, lung, lymphocytes, and cancer tissues [80–82]. The CD44 variant isoforms have a much more limited distribution [81]. CD44 is a transmembrane glycoprotein and the cellular receptor for components of the extracellular matrix (ECM) particularly hyaluronic acid (HA) or collagen and laminin (**Fig. 8**) [83].

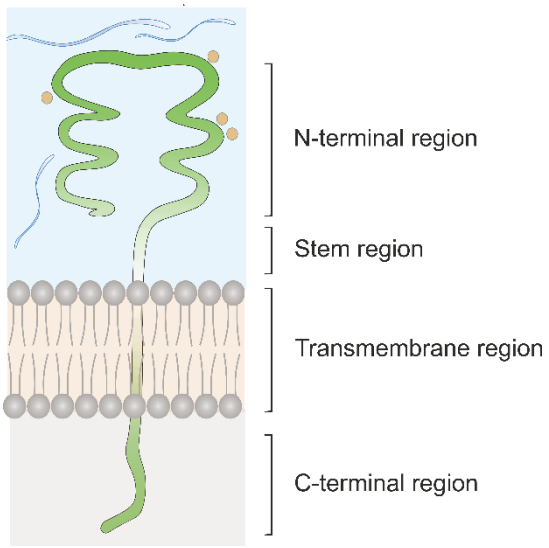

Fig. 8: CD44 protein structure.
CD44 protein has four characteristic regions, consisting of the N-terminal extracellular region, the stem region, the transmembrane region and the C-terminal cytoplasmatic region. The N-terminal region is the ligand-binding domain, where especially the cell's ability to bind hyaluronic acid (HA) is finely regulated. The stem region is variable in variant isoforms of CD44 due to alternative splicing. The C-terminal region supports the binding of intracellular proteins with functions in cytoskeleton organization and signalling.

As a member of the cell adhesion molecule family, CD44 plays a key role in cellular communication and adhesion between cells and the ECM. In addition, it is involved in various other physiological functions

including lymphocyte homing/activation, leukocyte activation, and cytokine release. On the other hand, it can also promote pathological processes such as migration, invasion, proliferation, cellular growth and tumor metastasis [81, 84].

Cells show two different states for the ligand affinity of CD44. There is the low-affinity state for ligands when the cells are resting and the high-affinity, active state of CD44. The active state must be induced by soluble factors such as cytokines. The activation of CD44 leads to initiation of intracellular signalling pathways, e.g. extracellular signal-regulated kinase 1/2 (ERK1/2), AKT, or TGF-β signalling [82, 85, 86].

In parallel with the observed upregulation of CD44 expression in Müller cells in RP retinas [78, 79, 79], elevated protein expression has also been reported in many different types of cancer. CD44 signalling within tumors is associated with tumorigenicity, tumor initiating potential, aggressiveness, metastasis, and therapy resistance [82, 84].

1.4.2 Role of CD44 in the retina

In the retina, the major isoform of the cell surface antigen CD44 is the standard variant of approximately 90 kDa and is expressed by mature rodent as well as human Müller glial cells, especially in the apical microvilli of Müller cells [79, 87, 88]. These microvilli project into the IPM, which prominent component is HA. HA may has an organizing and supportive function, as it can interact with its receptor CD44 [89].

In addition, it has been shown that the protein is also expressed in the developing retina in cells that later differentiate into Müller cells. Knockout and overexpression experiments additionally showed that the fate of retinal progenitor cells to become Müller cells was not regulated by CD44 expression. These findings suggest, that CD44 is a marker to specifically label Müller glia precursors, but its expression has no influence on maturation [90].

Several studies observed that CD44 expression is highly upregulated in Müller cells in RP retinas after disease onset [78, 79, 91] and that CD44 could mediate the attachment of the retina to components of the interphotoreceptor matrix [88].

But the question remains unanswered of why CD44 expression is upregulated in the degenerating retina and whether this has any consequences for the other retinal cell types. This is especially important considering how significant Müller cells are for retinal integrity and stability, and that under gliotic conditions they can both slow and promote disease progression.

Therefore, this study investigated the effects of CD44 knockout in Müller cells on retinal disease progression.

1.5 Mouse models

A Pde6b-deficient (*Pde6b*^{STOP}) RP mouse model was used in this study. Here, the PDE6B expression was inhibited by the insertion of a floxed STOP cassette into intron 1 of the *Pde6b* gene on both alleles, leading to homozygous *Pde6b*$^{STOP/STOP}$ (also referred to as ST/ST) mice. As wildtype control, mice with a heterozygous insertion of a floxed STOP cassette were used (*Pde6b*$^{STOP/WT}$, also referred to as ST/WT) (**Fig. 9**) [92].

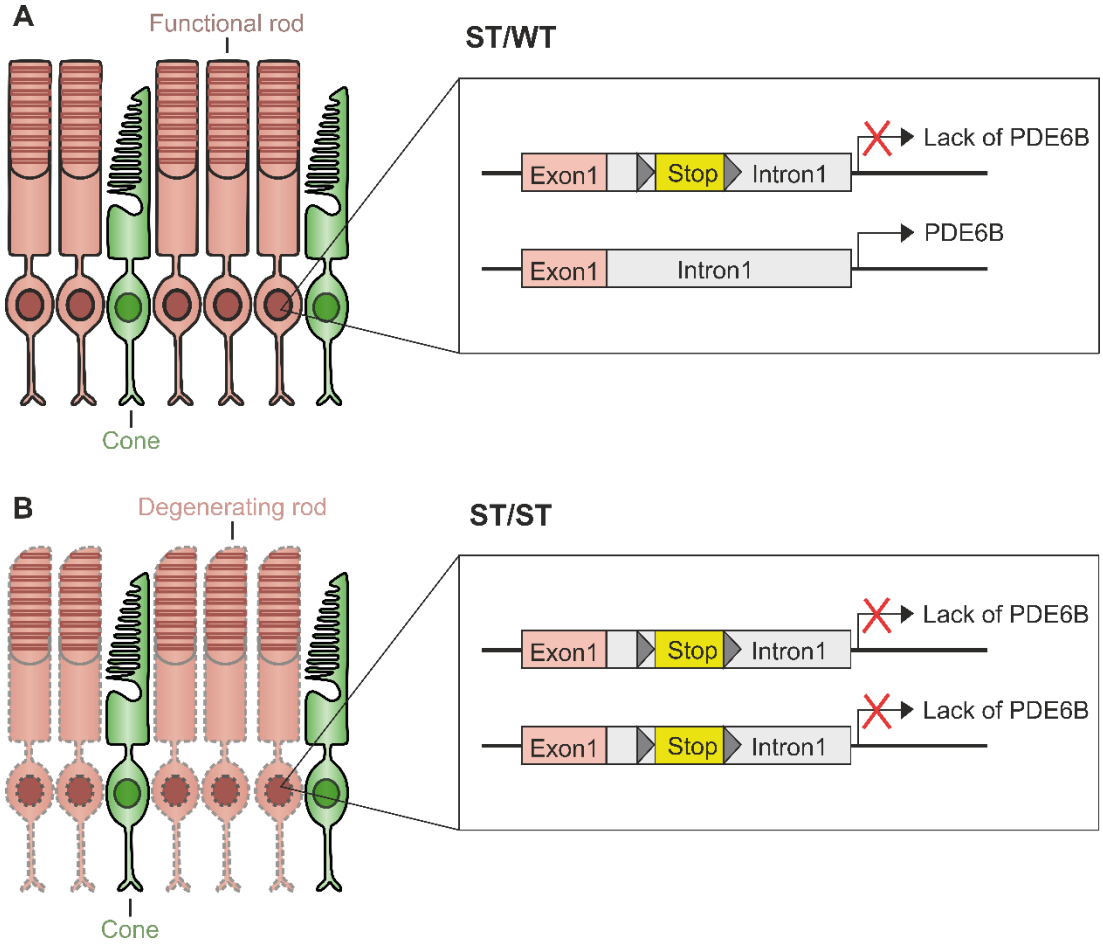

Fig. 9: *Pde6b*^{STOP} mouse model.
Insertion of a floxed STOP cassette in intron 1 of the Pde6b gene. **(A)** ST/WT mice are heterozygous for the STOP cassette, and one allele still expresses PDE6B; therefore, ST/WT mice serve as wildtype control. **(B)** ST/ST mice contain the STOP cassette on both alleles of the *Pde6b* gene, which prevents *Pde6b* transcription and consequently leads to rod photoreceptor degeneration.

To investigate the role of CD44 on RP disease progression, ST/ST mice were crossed with CD44 knockout (CD44$^{-/-}$) mice. In these mice the expression of all CD44 isoforms was abolished by targeted insertion of a lacZ/neo cassette into exon 1 and a part of intron 1. CD44$^{-/-}$ mice are viable, fertile, and showed no behavioural abnormalities. Only the lymphocytes exhibit a reduced ability to migrate to peripheral lymph nodes and thymus, although lymphocyte development appears to be unremarkable in CD44$^{-/-}$mice [93].

2 Aim of the thesis

In the healthy retina, Müller glia, the main support cell in the retina, fulfil multiple functions essential for photoreceptor health. In human and rodent RP retinas, Müller cells are activated by photoreceptor degeneration – a process, known as Müller cell gliosis, marked by metabolic changes and upregulation of CD44. CD44 is a cell surface transmembrane glycoprotein and the primary receptor for extracellular hyaluronic acid. Given the key roles played by Müller glia in healthy retina, and the changes they undergo in RP, it is important to understand their role in RP pathogenesis.

The thesis aimed to determine the function of CD44 in the healthy and diseased RP retina using *Cd44*$^{-/-}$ and *Pde6b*^{STOP} *Cd44*$^{-/-}$ mice, respectively. To investigate the impact of CD44 on photoreceptor survival and function, comprehensive morphological characterization (ONL thickness, cone inner and outer segments, inner retinal remodeling) and ERG recordings will be performed, respectively. Proinflammatory responses will also be assessed. To unravel downstream effects of CD44 in healthy and diseased retinas, Müller cells will be isolated using a multistep magnetic-activated cell sorting (MACS) approach and subjected to proteomics. The proteomics data will undergo bioinformatic analysis to identify dysregulated proteins. Interesting candidates will be validated by qRT-PCR, immunoblot, and immunohistochemistry.

This study will advance our understanding of RP disease progression and how photoreceptors and Müller cells are structurally and functionally coupled.

3 Material and methods

3.1 Material

3.1.1 Mouse line

All animal experiments were performed in accordance with the ARVO statement on the use of animals in ophthalmic and vision research and were approved by the local authorities (Regierung von Oberbayern). Mice were kept under standard conditions on a 12 h light/ dark cycle and had *ad libitum* access to water and food.

Pde6b^{STOP} mice were generated in the Barbara & Donald Jonas Stem Cells Laboratory, Columbia University, USA [92]. A STOP cassette was inserted in intron 1 of the *Pde6b* gene. Mice were rederived via *in vitro* fertilization at the Biomedical Center Munich, Germany. In this study mutant (*Pde6b*$^{STOP/STOP}$, also referred to as ST/ST) and control mice (*Pde6b*$^{STOP/WT}$; also referred to as ST/WT) of both sexes were used.

B6.129(Cg)-*Cd44*^{tm1Hbg}/J mice (referred to as CD44$^{-/-}$) were obtained from the Jackson Laboratory. Those mice carry a neomycin resistance/lacZ cassette that disrupts exon 1 and part of intron 1, resulting in complete loss of CD44 transcription [93]. To generate the *Pde6b*^{STOP} *Cd44*$^{-/-}$ mouse line *Pde6b*^{STOP} mice were crossed with *Cd44*$^{-/-}$mice to generate *Pde6b*$^{STOP/STOP}$ *Cd44*$^{-/-}$(also referred to as CD44$^{-/-}$ ST/ST) and *Pde6b*$^{STOP/+}$ *Cd44*$^{-/-}$ (also referred to as CD44$^{-/-}$ ST/WT) mice.

Table 1: Primers used for genotyping

Primer name	Forward Primer	Reverse primer	Internal primer	Annealing temperature [°C]
Pde6b^{STOP}	TGCTCTGTGGT GTTGCTCTGC	TGGCGATGCAG AGTGTCCTGA	GTCCTGCACGA CGCGAGCTG	65
CD44$^{-/-}$	ATCCCAGCTTTG CTTTGCTA	GTTTTCCCAGTC ACGACGTT	GCGACTAGATCC CTCCGTTT	57

3.1.2 Chemicals

Table 2: Utilized chemicals and reagents

Name	Supplier	Catalog Number
2-Mercaptothanol	Sigma-Aldrich/Merck	M7522
100 bp DNA Ladder	Thermo Fisher Scientific	15628050
10X Blue Juice	Thermo Fisher Scientific	10816015
Acetic Acid	Carl Roth	3738.4
Anti-Biotin MicroBeads	Miltenyi Biotec	130-090-485
Aqua-Poly/Mount	Polysciences	18606-5
Blotto, non-fat dry milk	Santa Cruz	sc-2324
Bromphenol blue	Carl Roth	A512.1
ChemiBLOCKER	Merck Millipore	2170
$CaCl_2$	Carl Roth	CN93.1
CD11b MicroBeads UltraPure, mouse	Miltenyi Biotec	130-126-725
CD29 Antibody, anti-mouse, Biotin	Miltenyi Biotec	130-101-943
CD31 MicroBeads, mouse	Miltenyi Biotec	130-097-418
cOmplete™, EDTA-free Protease Inhibitor Cocktail	Sigma-Aldrich/Merck	4693132001
D(+)-Glucose	Carl Roth	HN06.2
D(+)-Sucrose	Carl Roth	4621.1
Dithiothreitol (DTT)	Thermo Fisher Scientific	R0861
dNTP Set (100 mM)	Thermo Fisher Scientific	10297018
DreamTaq Green DNA-Polymerase (5 U/µl)	Thermo Fisher Scientific	EP0712
Dynabeads™ Protein A for Immunoprecipitation	Thermo Fisher Scientific	10001D

Name	Supplier	Catalog Number
Epredia™ Neg-50™ Frozen Section Medium	Fisher Scientific	11912365
Ethanol	Carl Roth	5054.1
Glycerine	Carl Roth	3783.3
Glycine	VWR Chemicals	24403.298
HEPES	Carl Roth	HN77.3
Hoechst 33342, Trihydrochloride, Trihydrate	Thermo Fisher Scientific	H1399
Immobilon Forte Western HRP substrate	Merck Millipore	WBLUF0100
Isotonische Natriumchlorid-Lösung ad us. Vet.	BRAUN	1409.99.99
Isopropanol	Carl Roth	6752.2
KCl	Carl Roth	6781.3
Ketamin 10%	Serumwerk Bernburg AG	13690.00.00
KH_2PO_4	Carl Roth	3904.2
Methanol	Carl Roth	0082.3
$MgCl_2$	Carl Roth	KK36.2
M-PER™ Mammalian Protein Extraction Reagent	Thermo Fisher Scientific	78503
$Na_2EDTAx2H_20$	Sigma-Aldrich	E1644-250G
Na_2HPO_4	Carl Roth	T876.1
NaCl	VWR Chemicals	27810.295
$(NH_4)_2S_2O_8$	Carl Roth	9178.3
Normal Rabbit Immunoglobulin	Peprotech	500-P00
PageRuler™ Plus Prestained Protein Ladder	Thermo Fisher Scientific	26619

Name	Supplier	Catalog Number
PageRuler™ Plus Prestained Protein Ladder	Thermo Fisher Scientific	26619
Papain	Sigma-Aldrich/Merck	10108014001
Paraformaldehyde	Carl Roth	0335.2
Phosphatase Inhibitor Cocktail (100X)	Cell Signaling	5870
Pierce™ Bovine Serum Albumin Standard Ampules	Thermo Fisher Scientific	23209
Pierce™ Coomassie (Bradford) Protein Assay Kit	Thermo Fisher Scientific	23200
PowerUp™ SYBR™ Green Master Mix	Thermo Fisher Scientific	A25777
ROTIPHORESE®NF-Acrylamide solution 30 (29:1)	Carl Roth	A124.1
SDS ultra pure	Carl Roth	2326.1
SYBR™ Safe DNA Gel Stain	Thermo Fisher Scientific	S33102
TEMED	Carl Roth	2367.3
Tris HCl	Carl Roth	9090.3
Tris	Carl Roth	0188.1
Triton X® 100	Carl Roth	3051.3
Trypsin/Lys-C Protease Mix, MS Grade	Thermo Fisher Scientific	A41007
Tween® 20	Carl Roth	9127.1
Super PAP Pen Liquid Blocker	Science Services	N71312-N
rDNase Set	Macherey-Nagel	740963
Restore™ PLUS Western Blot Stripping Buffer	Thermo Fisher Scientific	46428
UltraPure™ DNase/RNase-Free Distilled Water	Thermo Fisher Scientific	10977035

Name	Supplier
Xylazin 20 mg/ml	WDT

3.1.3 Buffers and solutions

Table 3: Composition of utilized buffers and solutions

Name	Composition
5X Laemmli	2,5 g SDS 12,5 ml Glycerine 6,25 ml 2-Mercaptothanol 0,013 g Bromphenol blue ad 50 ml Tris-HCl buffer (1,25 M) adjust pH = 6.8
10X Phosphate-buffered saline (PBS)	11.75 g Na2HPO4 2 g KH2PO4 80 g NaCl 2 g KCl ad 1000 ml ddH_20
1X PBS	100 mL 10X PBS ad 900 ml ddH_20 adjust pH = 7.4
50X TAE	242 g tris base 57.1 mL acetic acid 37.2 g $Na_2EDTAx2H_20$ ad 1000 ml ddH_20
1X TAE	10 mL 50X TAE ad 500 ml ddH20
10X Running Buffer	144 g Glycine 30,3 g Tris ad 1000 ml ddH_2O

Name	Composition
1X Running Buffer	100 ml Running Buffer 10X 1 g SDS ad 1000 ml ddH_2O
10X TBS	60,57 g Tris 87,66 g NaCl ad 1000 ml ddH_2O
5X ECS	39,74 g NaCl 1,12 g KCl 1,0 g $MgCl_2$ 11.91 g HEPES 1,47 $CaCl_2$ 10,9 Glucose ad 1000 ml ddH_2O
1X ECS	10 ml 5X ECL ad 50 ml ddH_2O adjust pH = 7.4
1000X DTT	0,78 g DTT 10 ml ddH_2O
2 % agarose solution	2 g Agarose ad 100 ml 1X TAE
10 % APS solution	10 g $(NH_4)_2S_2O_8$ ad 100 ml ddH_2O
4 % paraformaldehyde (PFA)	6 g PFA ad 150 ml 1X PBS
30 % sucrose solution	150 g D(+)-Saccharose ad 500 ml ddH_20
10% Triton X-100	1 ml Triton X-100 9 ml PBS
1,25 M Tris-HCl	19,7 g Tris HCl ad 100 ml ddH_2O
1M Tris pH 8.0	24.23 g tris ad 200 ml ddH_20 adjust pH = 8.0

Name	Composition
1M Tris pH 7.4	24.23 g tris ad 200 ml ddH_20 adjust pH = 7.4
0,1M Tris	6.057 g tris base ad 500 ml ddH_20 pH = 7.8
50mM NaOH	2 g NaOH ad 1 l ddH_20
100 bp DNA ladder	100 µl 10X Blue Juice 100 µl 100 bp DNA ladder Invitrogen 400 µl ddH_20
Hoechst 50 mg/ml	100 mg Hoechst 33342 ad 2000 µl ddH20
Hoechst solution	5 µL 50 mg/mL Hoechst ad 50 ml 1X PBS
PBS/Glucose solution	2,18 g Glucose ad 1000 ml PBS 1X
Protease Inhibitor Cocktail 25X	1 tablet cOmplete™ ad 2 ml ddH_2O
TBS-T	1 g Tween® 20 100 ml TBS 10X Ad 1000 ml ddH_2O
Transfer Buffer	100 ml Running Buffer 10X 200 ml Methanol ad 1000 ml ddH_2O

3.1.4 Antibodies

Table 4: Primary and secondary antibodies

Antibody	Host species	Dilution (IHC)	Dilution (WB)	Supplier	Catalog Number
B-Actin-Peroxidase	Mouse	-	1:6000	Sigma-Aldrich	A3854-200UL
Calbindin D-28k	Mouse	1:8000	-	Swant	300
CD44 (mouse)	Rat	1:400	-	BD Pharmingen	550538
CD44	Rabbit	-	1:2000	Abcam	ab28364
CD68	Rat	1:500	-	Bio-Rad	MCA1957T
Cone Arrestin (Arr3)	Rabbit	1:1000	-	Merck	AB15282
GARP clone 4B1	Mouse	1:800	-	Sigma-Aldrich	MABN2429
GFAP	Mouse	1:1000	1:800	Sigma-Aldrich	G3893
GLUL	Rabbit	1:2000	1:2000	Abcam	ab228590
Iba1	Rabbit	1:1000	-	VWR / Fujifilm Wako	WAKO019-19741
IL-1β	Rabbit	-	1:300	Abcam	ab9722
Pde6b	Mouse	-	1:400	Santa Cruz	sc77486
PKCα	Mouse	1:1000	-	Santa Cruz	Sc-8393
PKM2	Rabbit	1:800	1:2000	Cell Signaling	#4053
Recoverin	Rabbit	1:1000	-	Sigma-Aldrich	AB5585

Antibody	Host species	Dilution (IHC)	Dilution (WB)	Supplier	Catalog Number
Secretagogin	Rabbit	1:5000	-	Prof. Dr. Wagner (University of Vienna, Austria)	
Slc1a2	Rabbit	1:50	1:1000	Cell Signaling	20848
488-Goat anti-Rat	Goat	1:1000	-	Thermo Fisher	A-11006
488-Goat anti-Rabbit	Goat	1:1000	-	Thermo Fisher	A-11070
555-Goat anti-Mouse	Goat	1:1000	-	Thermo Fisher	A-21425
555-Goat anti-Rat	Goat	1:1000	-	Jackson	112-165-143
647-Goat anti-Rabbit	Goat	1:1000	-	Thermo Fisher	A-21245
anti-Rabbit HRP	Mouse	-	1:2000	Santa Cruz	sc-2357
anti-Mouse HRP	Mouse	-	1:2000	Santa Cruz	sc-516102

3.1.5 Primers used for qRT-PCR

Table 5: qRT-PCR Primers

Primer name	Forward primer	Reverse primer	Product length [bp]
CD44	ACGAGGAGGAGGTGTGATGT	GTGGCTTTTTGAGGGGTTC	121
GAPDH	CATCACTGCCACCCAGAAGACTG	ATGCCAGTGAGCTTCCCGTTCAG	153
GFAP	CACCTACAGGAAATTGCTGGAGG	CCACGATGTTCCTCTTGAGGTG	137
IL-6	TACCACTTCACAAGTCGGAGGC	CTGCAAGTGCATCATCGTTGTTC	116

Primer name	Forward primer	Reverse primer	Product length [bp]
NF-κB	GCTGCCAAAGAAGGACACGACA	GGCAGGCTATTGCTCATCACAG	131
TNF-α	TCTTCTCATTCCTGCTTGTGG	GGTCTGGGCCATAGAACTGA	128

3.1.6 Kits

Table 6: Commercially available Kits

Name	Supplier	Catalog number
Lactate Assay Kit	Sigma-Aldrich	MAK064
NucleoSpin® RNA, Mini kit for RNA purification	Macherey-Nagel	740955.50
PicoProbe™ Glutamate Assay Kit (Fluorometric)	Abcam	ab252893
Quantikine™ Hyaluronan ELISA Kit	R&D Systems	DHYAL0
RevertAid First Strand cDNA Synthesis Kit	Thermo Fisher Scientific	K1622

3.1.7 Consumables

Table 7: Consumables

Name	Supplier	Catalog number
24-Well plates	Greiner	662160
96-Well plates	Greiner	655101
ACQUITY UPLC M-Class HSS T3 Column, 100Å, 1.8 µm, 75 µm X 250 mm, 1/pk	Waters	186007474

Name	Supplier	Catalog number
Amersham™ Hybond® P Western blotting membranes, PVDF	Sigma-Aldrich/Merck	GE10600021
Braun Sterican® Cannula G 30 0,30 x 12 mm	Neolab	TZ-1438
Coverslips Thickness: 1, 24 x 60 mm	Carl Roth	H878.2
Epredia™ SuperFrost Plus™ Adhesion slides	Fisher Scientific	10149870
Large cell columns	Miltenyi	130-042-202
MicroAmp™ Fast Optical 96-Well Reaction Plate, 0.1 mL	Thermo Fisher Scientific	4346907
MicroAmp™ Optical Adhesive Film	Thermo Fisher Scientific	4311971
Multiply®-µStrip Pro 8-strip	Sarstedt	72.991.002
SafeSeal reaction tube, 1,5 ml	Sarstedt	72.706
SafeSeal reaction tube, 2,0 ml	Sarstedt	72695500
SafeSeal reaction tube, 5 ml	Sarstedt	72.701
Scalpel	Hartenstein	SK11
Screw cap tube, 15 ml	Sarstedt	62554502
Screw cap tube, 50 ml	Sarstedt	62559001
Whatman® paper	Carl Roth	7602.1

3.1.8 Instruments

Table 8: Instruments

Name	Supplier
16-Tube SureBeads™ Magnetic Rack	Bio-Rad
Agarose gel chamber	Danaphore
Castroviejo Spring Scissors - Sharply Curved Up	FST
Centrifuge 5425 R	Eppendorf
ChemiDoc™ MP	Bio-Rad
Corning® LSE™ 6770 Mini Mikrozentrifuge	Omnilab
Cryostat CM3050 S	Leica
Dumont #55 Forceps	FST
Espion ERG Diagnosys equipment	Diagnosys LLC
Gel Doc 2000	Bio-Rad
Heating mat	Trixie
Keyence BZ-X800	Keyence
Kleinfeld Vortex Genie® 2 Mixer	Omnilab
Leica TCS SP8 Inverted	Leica
Mastercycler® nexus GX2	Eppendorf
Microscope DM750	Leica
Mini-PROTEAN® Tetra System	Bio-Rad
Mixer Mill MM 400	Retsch
NanoDrop™ 2000c Spectrophotometer	Thermo Fisher Scientific
OctoMACS™ Separator	Miltenyi

Name	Supplier
PCR Plate Spinner	VWR
pH meter Lab 850	Schott Instruments
Pipette controller, Stripettor™ Ultra	Omnilab
PowerPac™ Basic	Bio-Rad
Q Exactive HF-X mass spectrometer	Thermo Fisher Scientific
QuantStudio™ 5 Real-Time PCR System	Thermo Fisher Scientific
Rotamax 120	Heidolph
Sonifier® W-450 D	Branson
SpectraMax® iD3	Molecular Devices
Student Dumont #7 Forceps	FST
Thermomixer compact	Eppendorf
Tube Rotator	VWR
UltiMate™ 3000 RSLCnano System	Thermo Fisher Scientific
Vannas-Tübingen Spring Scissors	FST
Zoom Stereomicroscope SZ51	Olympus

3.1.9 Software

Table 9: Software

Name
ApE - A Plasmid Editor
CorelDRAW 2018
Espion V6

Name
GraphPad Prism 9.3.1
ImageJ
ImageLab 6.1
Microsoft Office 2016 (Excel, Power Point, Word)
Perseus v2.0.7.0
Primer3Plus
Proteome Discoverer 2.4 SP1 software (v2.4.1.15)
QuantStudio™ Design & Analysis Software v1.5.2

3.2 Methods

3.2.1 Genotyping

To isolate the DNA, the ear punches were boiled at 95 °C in 600 µl 50mM NaOH for 10 min. Then, 50 µl of 1 M tris HCL was added and roughly vortexed to lyse the punch completely. After 6 min of centrifugation at room temperature, the supernatant was transferred into a fresh tube and stored on ice. Now components of the master mix (**Table 10-11**) were mixed with the exception of the DNA template and transferred to 0,2 ml PCR tubes. The tubes were labeled, and the corresponding DNA template was added to each tube. The used primers and their annealing temperatures used for genotyping are listed in **Table 1** and the thermocycling conditions are given in **Tables 12-13.**

Table 10: Master Mix components for Pde6b^{STOP} genotyping

Component	µl
10xDreamtaq mix	1,50
dNTPs	0,50
10µM Forward Primer	1,25
10µM Reverse Primer	1,25
10µM Intermediate Primer	1,25
DNA template	1,00

Component	µl
DNA template	1,00
PCR grade water	8,13
Dream Taq polymerase	0,13
Total volume	15,00

Table 11: Master Mix components for CD44$^{-/-}$ genotyping

Component	µl
10xDreamtaq mix	1,50
dNTPs	0,50
10µM CD44 Common Primer	0,75
10µM CD44 Wildtype Reverse Primer	0,75
10µM CD44 Mutant Reverse Primer	0,75
DNA template	1,00
PCR grade water	9,63
Dream Taq polymerase	0,13
Total volume	15,00

Table 12: Thermocycling conditions for Pde6b^{STOP} primers

Step	Temperature [°C]	Duration	Cycles
Initial denaturation	95	3 min	1
Denaturation	95	30 sec	
Annealing	65	30 sec	30
Extension	72	1 min	
Final extension	72	10 min	1
	4	hold	

Table 13: Thermocycling conditions for CD44$^{-/-}$ primers

Step	Temperature [°C]	Duration	Cycles
Initial denaturation	95	3 min	1
Denaturation	95	30 sec	
Annealing	57	30 sec	30
Extension	72	1 min	
Final extension	72	10 min	1
	10	hold	

To separate the amplified DNA PCR products by size, a 2 % agarose gel was prepared. This was achieved by dissolving agarose in 1X TAE buffer and subsequently heating the mixture in a microwave. After the agarose solution was cooled down to approximately 50 °C, 5 µl Sybr Safe was added to 100 ml of 2 % agarose solution, mixed and poured into a gel chamber with comb. After the gel has set, the comb was removed, and the chamber was filled with 1X TAE. A 100 bp DNA ladder and the PCR samples were then loaded into the pockets of the gel. The gel was subjected to electrophoresis at 70 V for about 15 minutes. The amplified DNA fragments were visualized using Gel Doc 2000 system. The expected product lengths are listed in **Table 14.**

Table 14: Product length of PCR products

	Pde6b^{STOP}	**CD44$^{-/-}$**
Wildtype lane [bp]	284	218
Mutant lane [bp]	415	115

3.2.2 Tissue preparation

3.2.2.1 Retina isolation

After euthanization, the eye was gently pulled out of the orbit with bent forceps and held in place. The cornea was now carefully incised from nasal to temporal with a scalpel. Subsequently, the forceps were pulled gently, which causes the retina to detach, allowing it to be isolated. The isolated retina was washed briefly in phosphate-buffered saline (PBS), transferred to a tube and frozen in liquid nitrogen.

3.2.2.2 Retinal cryosections

After the mouse was euthanized, the temporal side of the eye was marked with a hot cannula (**Fig. 10** step 1). After the eye was marked, it was removed from the orbit with slightly curved scissors by cutting the optic nerve. Now the eye was placed in a 35 mm dish under the stereo microscope Olympus SZ51 and a hole was made slightly above the *ora serrata* with a thin cannula, exactly at the point where the *ora serrata* and the mark intersect (**Fig. 10** step 3). To pre-fix the tissue, the eye was now placed in 4 % paraformaldehyde (PFA) for 5 minutes. Following the incubation period, the hole was used to cautiously insert small scissors, allowing for a careful cut along the *ora serrata* (**Fig. 10** step 4). It is essential to always cut above the *ora serrata* to avoid detachment of the retina. When reaching the initial starting point where the burn mark is located, a small vertical incision was made just below the *ora serrata* to mark the original eye orientation and thus preserve important information for subsequent processing. At this stage, the cornea can be lifted off, and both the lens and vitreous can be removed (**Fig. 9** step 5).

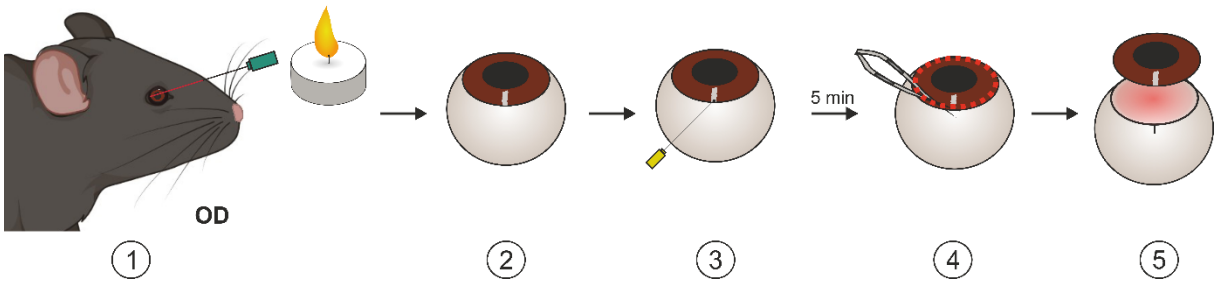

Fig. 10: Schematic drawing of the eye preparation for retinal cryosections.
After the mouse was sacrificed, the temporal orientation of the right eye (OD) was marked with a hot cannula (step 1). Subsequently the eye was removed from the eye socket with the help of curved scissors (step 2) and then a small hole was made with a cannula above the *ora serrata* where the burn mark is located (step 3). The eye was now incubated for 5 min in 4 % PFA. Subsequently, fine scissors were used to cut in a circle along the *ora serrata* and slightly into the temporal mark (step 4). Preparation of eyecups was completed by removal of cornea and lens (step 5). Eyecups were used for frozen sections.

The eyecup was subsequently fixed in 4 % PFA for 45 min. Following fixation, the eyecup was washed three times for 5 min each with PBS and then immersed in 30 % sucrose solution for a minimum of 2 hours or overnight. Once the eyecup had sunk to the bottom of the well, it was ready to be embedded in Cryo Medium for further processing. To do so, any excess sucrose solution was carefully removed using tissue. Then, the eyecup was positioned with the back of the eye facing downward into a handmade aluminum foil cup filled with Epredia™ Neg-50™ Frozen Section Medium. The aluminum cup was provided with an external mark that allowed alignment of the eyecup. The eyecup with its temporal incision was aligned parallel to the mark to retain the orientation of the eye, and then slightly

submerged under the medium and frozen on dry ice. Subsequently, the frozen eyecup was stored at -80 °C until the eyes were sectioned.

Prior to sectioning the eyes with a cryostat, the mark on the aluminum cup was transferred to the top surface of the frozen block. Subsequently, the aluminum foil was removed, and the frozen eye was clamped in the cryostat with the mark facing downward to obtain sections with dorso-ventral orientation. The eye was cut into 10 µm thick sections using the Leica Cryostat CM3050 S. Six of the retinal sections were collected on each Epredia™ SuperFrost Plus™ slide. To reduce the number of slides, one slide with sections was collected before the optic nerve, the entire optic nerve, and another slide after the optic nerve. The slides were stored at -20 °C until they were used.

3.2.3 Immunohistochemistry of retinal sections

The retinal sections were thawed and subsequently encircled with a liquid blocker. Once the blocker has dried, a drop of PBS was added to each section in order to wash away the mounting medium. The primary antibody (**Table 4**) was diluted in PBS containing 5 % Chemiblocker and 0,3 % Triton X® 100. The antibody solution was applied to the sections and then incubated overnight at 4 °C. The next day, the retinal sections were initially washed three times with PBS and then they were incubated with the appropriate secondary antibodies (**Table 4**) in PBS containing 3 % Chemiblocker for a duration of 1,5 hours at room temperature. After the incubation period, the sections were washed three times with PBS. To stain the DNA and thereby make the cell nuclei visible, the sections were incubated with Hoechst solution for 5 min and then washed three times with PBS. Afterwards, the slides were gently tapped on a tissue to remove as much PBS as possible, a drop of Aqua-Poly/Mount mounting medium was added to each section and the slide was carefully covered with a coverslip. To allow the medium to cure, the slides were dried overnight in the dark at room temperature. Subsequently, the slides were stored in the refrigerator at 4 °C.

3.2.4 Imaging of fluorescence staining

Fluorescence staining of retinal cryosections was imaged at the Leica SP8 Inverted scanning confocal microscope with a 40x oil objective. For quantitative analyses, the images were acquired with the compact fluorescence microscope KEYENCE BZ-X800.

3.2.5 Quantitative analysis of ONL thickness

To determine the thickness of the ONL, retinal sections were stained with Hoechst. By staining the nuclei, the thickness of the ONL can be measured. For this purpose, two sections per eye were taken from the central area of the retina with a 20x objective. Using the program ImageJ, the thickness of the ONL was measured at a distance of 300 µm from the optical nerve on the ventral side of the eye. Two sections were measured per biological replicate (N number) and the mean value of these was calculated. To check whether there was a significant difference in ONL thickness between genotypes, an ordinary one-way ANOVA analysis was performed. Results were considered to be significantly different if the calculated p-value between two groups was less than 0.05. The N numbers for the respective genotypes and the different time points are listed in **Table 15**.

Table 15: N numbers for ONL thickness and cone IS+OS length quantification

Genotype	Age [pw]	N numbers	
		ONL	Cones
ST/WT	3	5	5
$CD44^{-/-}$ ST/WT	3	5	5
ST/ST	3	5	5
$CD44^{-/-}$ ST/ST	3	5	5
ST/WT	4	6	5
$CD44^{-/-}$ ST/WT	4	6	6
ST/ST	4	6	6
$CD44^{-/-}$ ST/ST	4	6	6
ST/WT	8	6	5
$CD44^{-/-}$ ST/WT	8	7	7
ST/ST	8	7	5
$CD44^{-/-}$ ST/ST	8	6	6
ST/WT	12	8	8
$CD44^{-/-}$ ST/WT	12	6	6
ST/ST	12	5	5
$CD44^{-/-}$ ST/ST	12	6	6
$CD44^{+/+}$	60	3	3
$CD44^{+/-}$	60	4	4
$CD44^{-/-}$	60	5	5

3.2.6 Quantitative analysis of cone inner and outer segment length

The quantification of cone inner and outer segment length was performed on retinal sections. For this purpose, the sections were stained with the antibody against cone arrestin (Arr3) to label the cones and co-stained with Hoechst. Images were taken with a 20x objective, and the quantification was performed in ImageJ. To do so, the length of three cone inner and outer segments was measured at a distance of around 300 µm from the optic nerve on the ventral side of the retina. Three cones were measured per N number and the mean value of these was calculated. To check whether there is a significant difference in cone length between genotypes, an ordinary one-way ANOVA analysis was performed. Results were considered to be significantly different if the calculated p-value between two groups was less than 0.05. The N numbers for the respective genotypes and the different time points are listed in **Table 15.**

3.2.7 Quantitative analysis of rod and cone bipolar cell dendrites and horizontal cell processes

The quantification of rod and cone bipolar cell dendrites as well as the quantitative analysis of horizontal cell dendrites were performed on retinal cryosections. In order to do so, retinal sections were immunostained with antibodies against protein kinase C-alpha (PKC-α) to label the rod bipolar cells or secretagogin (SCGN) to label the cone bipolar cells or with calbindin to label the horizontal cells. The sections were co-stained with Hoechst. Images were taken with a 63x objective of the Leica SP8 Inverted scanning confocal microscope close to the optic nerve on the ventral side of the retina. The quantification of the dendrite area was performed in ImageJ. For this purpose, a 100 µm line was first drawn along the inner nuclear layer (INL). Then, the outer cell bodies were outlined along this line. In this way, the stained dendrite area could be binarized using the default threshold settings on all images and the number of pixels above the threshold was analyzed. For each animal, two optic nerve sections were analyzed and the pixel number averaged. The N numbers for the respective genotypes and the different time points are listed in **Table 16.**

Table 16: N numbers for rod and cone bipolar and horizontal cell dendrite quantification

Genotype	Age [pw]	N numbers
ST/WT	8	4
$CD44^{-/-}$ ST/WT	8	5
ST/ST	8	5
$CD44^{-/-}$ ST/ST	8	5

Genotype	Age [pw]	N numbers
ST/WT	12	8
CD44$^{-/-}$ ST/WT	12	6
ST/ST	12	5
CD44$^{-/-}$ ST/ST	12	6

3.2.8 Quantitative analysis of activated microglia

The quantification of activated and resting microglia was performed on retinal sections. For this, retinal sections were immunostained with an antibody against Iba1 to label microglia and with an antibody against cluster of differentiation 68 (CD68) to label activated microglia and co-stained with Hoechst. Images were taken with a 10x objective, and quantification was performed in ImageJ. First, the image was rotated so that the ONL was oriented horizontally. Then a rectangle with a length of 380 µm and width of 453 µm was inserted and positioned over the retina. Within this square, cells that were positive for Hoechst, Iba1, and CD68 were counted, corresponding to the number of activated microglia. For each animal, two retinal sections were analyzed, and the numbers were averaged. The N numbers for the respective genotypes and the different time points are listed in **Table 17.**

Table 17: N numbers for microglia quantification

Genotype	Age [pw]	N numbers
ST/WT	4	5
CD44$^{-/-}$ ST/WT	4	6
ST/ST	4	6
CD44$^{-/-}$ ST/ST	4	6
ST/WT	8	4
CD44$^{-/-}$ ST/WT	8	5
ST/ST	8	5
CD44$^{-/-}$ ST/ST	8	5
ST/WT	12	8
CD44$^{-/-}$ ST/WT	12	6

Genotype	Age [pw]	N numbers
CD44$^{-/-}$ ST/WT	12	6
ST/ST	12	5
CD44$^{-/-}$ ST/ST	12	6

3.2.9 Quantitative real-time PCR (qRT-PCR)

3.2.9.1 RNA extraction from the retina

After isolation of the retina (chapter 3.2.2.1), it was collected in a 2,0 ml tube and 350 µl RA1 buffer from NucleoSpin® RNA kit (Macherey-Nagel) and 3,5 µl 2-mercaptoethanol were added. The tissue was then homogenized in the MixerMill at 20 Hz for 2 min. According to the manufacturer's protocol, the lysate was transferred to the supplied filter tubes and briefly centrifuged. Subsequently, 350 µl 70 % ethanol was added, mixed, and the lysate was transferred to NucleoSpin® RNA Column and centrifuged. 350 µl MDB buffer was added, and the column was briefly centrifuged to dry the membrane. Then, 95 µl DNase reaction mixture was applied onto the membrane of the column and incubated for 15 min at room temperature. Then the membrane was washed three times, the first time with RAW2 buffer and twice with RA3 buffer. After the washing steps, the RNA was eluted in 30 µl RNase-free water during 2 min of centrifugation and stored on ice.
The quantity and quality of the extracted RNA were estimated by measurements with the Nanodrop spectrometer. The quality and purity of the RNA was evaluated using the 260/280 absorbance ratio. A ratio of approximately 2.0 was accepted as pure RNA.

3.2.9.2 cDNA synthesis

500 - 1000 ng of total RNA was used for cDNA synthesis using the RevertAid First Strand cDNA Synthesis Kit (Thermo Fisher Scientific) following the manufacturer's instructions. The RNA was incubated together with the random hexamer primer from the kit at 65 °C for 5 min. Subsequently, the kit components were added in the indicated order and the PCR was started. The obtained cDNA was diluted 1:5 with distilled water and used for quantitative real-time PCR.

3.2.9.3 qRT-PCR

Exon-spanning primer pairs were designed to hybridize exclusively to the desired transcript and to avoid genomic contamination. To do so the UCSC genome browser and the software Primer3Plus was used. The specificity of the primer pairs was then verified by checking the length of the PCR product using gel electrophoresis. The used reaction setup is listed in **Table 18** and the thermocycling conditions are listed in **Table 19.**

Table 18: Reaction setup

Component	**Volume**	**Final concentration**
10 µM Forward Primer	1 µl	0,5 µM
10 µM Reverse Primer	1 µl	0,5 µM
cDNA template	2 µl	< 20 ng
PowerUp™ SYBR™ Green Master Mix	10 µl	1X
UltraPure™ DNase/RNase-Free Distilled Water	6 µl	

Table 19: Thermocycling conditions for qRT-PCR

Step	**Temperature [°C]**	**Duration**	**Cycles**
Pre-treatment	50	2 min	1
Initial denaturation	95	2 min	1
Denaturation	95	3 sec	
Annealing	58	5 sec	40
Extension	60	25 sec	
Step	**Temperature [°C]**	**Duration**	**Cycles**
	95	15 sec	
Melting	60	1 min	1
	95	15 sec	

The relative quantification method was used to compare the residual gene expression of one sample to that of a reference gene. Glyceraldehyde 3-phosphate dehydrogenase (Gapdh) was used as the

reference gene for data normalization. The “double delta Ct” method (ΔΔCt) was used to calculate the relative expression of the target gene. The mean of two technical replicates was used to calculate the residual expression using the following equation:

$$\text{Residual expression (Target)} = 2^{(-\Delta \text{ Cq (Target-Reference)})}$$

3.2.10 Immunoblot

3.2.10.1 Protein extraction from retina

After isolation of the retina (chapter 3.2.2.1), it was collected in a 1,5 ml tube and 95 µl of M-PER™ Mammalian Protein Extraction Reagent, 4 µl of cOmplete™, EDTA-free protease inhibitor cocktail 25X and 1 µl of phosphatase inhibitor cocktail (100X) were added.

The tissue was then lysed on ice four times by ultrasonic pulses with an amplitude of 40 %. Ultrasound pulses lasted 10 sec each with a resting time of 10 sec between bursts. After sonication, samples were kept on ice for 10 min followed by centrifugation at 13 000 g for 10 min. The supernatant was transferred to a new tube and the protein content of the sample was determined immediately afterwards.

3.2.10.2 Protein quantification

The Bradford protein assay was used to measure total protein content. The assay consists of using a series of bovine serum albumin standards (Pierce™ Bovine Serum Albumin Standard Ampules) of 0, 125, 250, 500, 750, 100, and 2000 µg/ml to establish a calibration curve. The calibration curve can then be used to calculate the protein content of unknown samples. For that, 5 µl of the freshly prepared protein lysates were diluted 1:4 with water, vortexed, and kept on ice. 5 µl of each standard, sample, and blank (H_2O) was pipetted in triplicates into a 96-Well plate. After 250 µl Pierce™ Coomassie Reagent was added to each well, the plate was incubated for 10 min on a plate shaker at room temperature. The absorbance was measured at 595 nm with a plate reader (SpectraMax® iD3). The mean of all triplicates was calculated and that of the blank was subtracted from all others. Using the standard trend line formula, the amount of protein in the samples could be calculated, whereby x was replaced by the sample values. Immediately following the Bradford assay, 19 µl of 5X Laemmli was added to the remaining 95 µl of protein lysate and boiled at 95 °C for 5 min. The samples were stored at - 80 °C.

3.2.10.3 Immunoblot analysis

To separate the proteins by size, a sodium dodecyl sulfate-polyacrylamide gel electrophoresis (SDS-PAGE) had to be made first. For this purpose, a 1.0 mm thick 12,5 % acrylamide gel was prepared (**Table 20**).

Table 20: Components of 12,5 % Acrylamide gel for SDS-PAGE

Component	**Volume for 2 gels**
Resolving Gel	
ddH_20	3,8 ml
ROTIPHORESE®NF-Acrylamide solution 30	5,0 ml
4X Resolving Gel Buffer	3,0 ml
10X APS solution	120 µl
TEMED	12 µl
Stacking Gel	
ddH_20	3,1 ml
ROTIPHORESE®NF-Acrylamide solution 30	650 µl
4X Resolving Gel Buffer	1,25 ml
10X APS solution	50 µl
TEMED	10 µl

After thawing, the samples (chapter 3.2.10.2) were boiled at 95 °C for 5 min and then 20 µg protein per sample was loaded into the gel pockets. To check the size of the separated proteins, 7 µl PageRuler™ Plus Prestained Protein Ladder were also loaded. The gel was run for 20 min at 80 V and then continued for approximately another 1.5 h at 120 V until the bromophenol blue reached the end of the gel.

After SDS-PAGE, a blotting sandwich was prepared in 1X Transfer Buffer using a PVDF membrane previously activated in methanol for 1 min. The sandwich was placed in the blotting chamber, which was cooled both inside and out and filled with 1X Transfer Buffer. The transfer was run for 90 min at constant 90 V.

The membrane was then blocked in 5 % milk in TBS-T for one hour. Then the indicated primary antibody diluted in 5 % milk in TBS-T was added and incubated overnight at 4 °C. The next day, the membrane was washed three times with TBS-T and then the corresponding peroxidase-conjugated

secondary antibody was added for 1 h at room temperature. After three washes the blot was detected with chemiluminescent Western HRP substrate (Merck Millipore) on ChemiDoc™ MP (Bio-Rad). Blots were scanned with ImageLab and quantified by densitometry analysis with ImageJ. The analysis was semi-quantitative, as the relative expression of the target protein compared to a loading control was always calculated. The loading control was always from the same sample and was also detected on the same Western blot membrane.

3.2.11 Hyaluronan ELISA

The Quantikine™ Hyaluronan ELISA Kit (R&D Systems) was used to measure ≥ 35 kDa Hyaluronan (HA) in mouse retina. The assay was conducted according to the manufacturer's protocol.

After isolation of the retina (3.2.2.1), it was collected in a 1,5 ml tube and 95 µl of M-PER™ Mammalian Protein Extraction Reagent, 4 µl of cOmplete™, EDTA-free protease inhibitor cocktail 25X and 1 µl of phosphatase inhibitor cocktail (100X) were added.

The tissue was then lysed on ice three times by ultrasonic pulses with an amplitude of 40 %. Ultrasound pulses lasted 10 sec each with a resting time of 10 sec between bursts. After sonication, samples were kept on ice for 10 min followed by centrifugation at 13 000 g for 10 min. The supernatant was transferred to a new tube. ST/WT lysates were diluted 1:1 with ddH_2O and ST/WT $CD44^{-/-}$, ST/ST, and ST/ST $CD44^{-/-}$ lysates were diluted 1:4 with ddH_2O to ensure that the measured abundances were in the middle of the standard curve. After lysates were prepared, 50 µl of Assay Diluent RD1-14 was pipetted into each well of the plate included in the kit. Then, 50 µl of the standards and samples were added. The wells were covered and incubated for 2 hours at room temperature on a plate shaker. The wells were washed five times with the provided washing buffer and then 100 µl of Hyaluronan Conjugate was pipetted into the wells. The covered wells were incubated again for 2 hours at room temperature on a plate shaker. The wells were washed five times and 100 µl of Substrate Solution was added to each well and incubated for 30 min at room temperature protected from light. 100 µl Stop Solution was added to each well and the optical density of each well was measured at 450 nm and at 540 nm. For wavelength correction the readings at 540 nm were subtracted from the readings at 450 nm. A standard curve was created by plotting the mean absorbance for each standard on the y-axis against the concentration on the x-axis. Since the samples have been diluted in advance, the read from the standard curve must be multiplied by the dilution factor.

3.2.12 Lactate Assay

The Lactate Assay Kit (Sigma-Aldrich) was used to measure L(+)-Lactate in mouse retina. Lactate was measured according to the manufacturer's protocol.

A completely intact retina, which was collected in a 1,5 ml tube (3.2.2.1), was thawed and 110 µl of Lactate Assay Buffer were added. The tissue was then lysed on ice four times by ultrasonic pulses with an amplitude of 40 %. Ultrasound pulses lasted 10 sec each with a resting time of 10 sec between bursts. The samples were then centrifuged at 13 000 g for 10 min at room temperature. Standards and samples were pipetted in the wells of a 96-well plate according to the manufacturer's protocol. For the samples 15 µl of the obtained lysates were diluted with 35 µl Lactate Assay Buffer, to gain a final volume of 50 µl per well. Subsequently, 50 µl of the master reaction mix was added to each of the wells and mixed by using a horizontal shaker. The reaction was incubated for 30 min at room temperature and meanwhile protected from light. The absorbance was measured at 570 nm. To reduce the background, the value obtained for the blank lactate standard was subtracted from all readings. The values obtained from the lactate standards were used to plot a standard curve. The amount of lactate in the retinae was determined from the standard curve. Due to the dilution of the samples, the lactate concentration was multiplied by 3,33, which reflected the total amount of lactate in one retina.

3.2.13 Proteome analysis of Müller glia cells and Neurons of murine retina

3.2.13.1 Cell purification of murine retina using magnetic-activated cell sorting (MACS)

Neurons and Müller glia cells were isolated from whole murine retina using magnetic-activated cell sorting (MACS). First, two freshly isolated retinae were combined in one tube containing 672 µl PBS/Glucose solution. 28 µl of Papain was added and the mixture was incubated for 30 min at 37 °C. The tissue was then washed three times with PBS/Glucose and treated with DNaseI (200 U/ml in PBS/Glucose) for 4 min at room temperature. PBS/Glucose was removed and substituted with extracellular solution (1X ECS) before dissociating the retinae using a firepolished glass Pasteur pipette. Microglia and vascular cells were subsequently removed from the cell suspension by incubation with anti-mouse CD11b and CD31 microbeads (Miltenyi Biotec) for 15 min at 4 °C and passing through large cell columns (Mitenyi Biotec) using the magnetic OctoMACS™ Separator (Miltenyi Biotec). The resulting cell suspension was incubated with anti-CD29 biotinylated antibodies (Miltenyi Biotec) for 15 min at 4 °C, spun down, and the pellet was resuspended in ECS. Anti-biotin microbeads (Mitenyi Biotec) were added and incubated for 15 min at 4 °C. The suspension was passed through a large cell column, resulting in a neuron-rich flowthrough (negative for CD29). The bound CD29 positive Müller

cells were subsequently eluted from the column. To check the purity of the separated fractions, drop samples were taken for immunostaining. To do this, 100 µl of CD29 positive and CD29 negative samples were fixed in 4 % PFA for 15 min at room temperature, spun down, resuspended in 50 µl PBS, and dropped onto a slide.

3.2.13.2 Liquid chromatography-mass spectrometry (LC-MSMS)

Proteins were proteolyzed with LysC and trypsin with filter-aided sample preparation procedure (FASP) as described previously [94, 95]. Acidified eluted peptides were analyzed on a Q Exactive HF-X mass spectrometer (Thermo Fisher Scientific) online coupled to an UltiMate™ 3000 RSLCnano HPLC System (Dionex). Samples were automatically injected and loaded onto the C18 trap cartridge and after 5 min eluted and separated on the C18 analytical column (Waters) by a 90 min non-linear acetonitrile gradient at a flow rate of 250 nl/min. MS spectra were recorded at a resolution of 60 000 with an AGC target of 3 x 1e6 and a maximum injection time of 30 ms from 300 to 1500 m/z. From the MS scan, the 15 most abundant peptide ions were selected for fragmentation via HCD (higher energy collisional dissociation) with a normalized collision energy of 28, an isolation window of 1.6 m/z, and a dynamic exclusion of 30 s. MS/MS spectra were recorded at a resolution of 15 000 with a AGC target of 1e5 and a maximum injection time of 50 ms. Unassigned charges, and charges of +1 and >8 were excluded from precursor selection.

Acquired raw data was analyzed in the Proteome Discoverer 2.4 SP1 software for peptide and protein identification via a database search (Sequest HT search engine) against the SwissProt Human database (Release 2020_02, 20432 sequences), considering full tryptic specificity, allowing for up to one missed tryptic cleavage site, precursor mass tolerance 10 ppm, fragment mass tolerance 0.02 Da. Carbamidomethylation of cysteine was set as a static modification. Dynamic modifications included deamidation of asparagine and glutamine, oxidation of methionine, and a combination of methionine loss with acetylation on protein N-terminus. The Percolator algorithm [96] was used for validating peptide spectrum matches and peptides. Only top-scoring identifications for each spectrum were accepted, additionally satisfying a false discovery rate < 1 % (high confidence). The final list of proteins satisfying the strict parsimony principle included only protein groups passing an additional protein confidence false discovery rate < 5 % (target/decoy concatenated search validation).

Quantification of proteins, after precursor recalibration, was based on intensity values (at RT apex) for the top three unique peptides per protein. Peptide abundance values were normalized on total peptide amount. The protein abundances were calculated averaging the abundance values for admissible peptides. The final protein ratio was calculated using median abundance values of three to five

biological replicates in a non-nested design. For the lysate samples, statistical significance of the ratio change was ascertained employing the approach described in [97] which is based on the presumption that we look for expression changes for proteins that are just a few in comparison to the number of total proteins being quantified. The quantification variability of the non-changing "background" proteins can be used to infer which proteins change their expression in a statistically significant manner. The dataset was further analyzed with the Software Perseus and GraphPad Prism.

3.2.14 Glutamate Assay

The PicoProbe™ Glutamate Assay Kit (Fluorometric) (BioVision) was used to measure Glutamate in mouse retina. Glutamate was measured according to the manufacturer's protocol.

After protein extraction from retina (3.2.10.1), and protein quantification (3.2.10.2) 2 µl of the obtained lysate were diluted with 18 µl ddH_2O. Subsequently, 1,5 µl of the diluted samples were added into wells of a 96-well plate. The volume of the samples was adjusted to 50 µl/well with Glutamate Assay Buffer. For the standard curve 0, 2, 4, 6, 8, and 10 µl of a 10 µM Glutamate standard were added into a series of wells to generate 0, 20, 40, 60, 80, and 100 pmol of Glutamate/well respectively. The volume was adjusted to 50 µl/well with Glutamate Assay Buffer. Then the reaction mix was prepared. For each well, a total amount of 50 µl reaction mix was prepared containing:

Reaction Mix (50 µl/well)	
Glutamate Assay Buffer	45 µl
Glutamate Enzyme Mix	2 µl
Glutamate Substrate Mix	2 µl
Pico Probe™	1 µl

Reaction mix was added to each well containing the Glutamate standards and diluted samples. The total final reaction volume for each well was 100 µl. The fluorescence intensity (Ex/Em = 535/587 nm) was measured in kinetic mode at 37 °C for 60 min using SpectraMax® iD.

Two timepoints (t_1 and t_2) were chosen in the linear range of the plot to obtain the corresponding relative fluorescence unit (RFU) for all samples (R_{S1} and R_{S2}) and standards. The RFU of the 0 µM standard was subtracted from all standards and samples. The linear portion of every time curve for each standard and sample was extrapolated to the y-axis to obtain the Y-Intercept (**Fig. 11**).

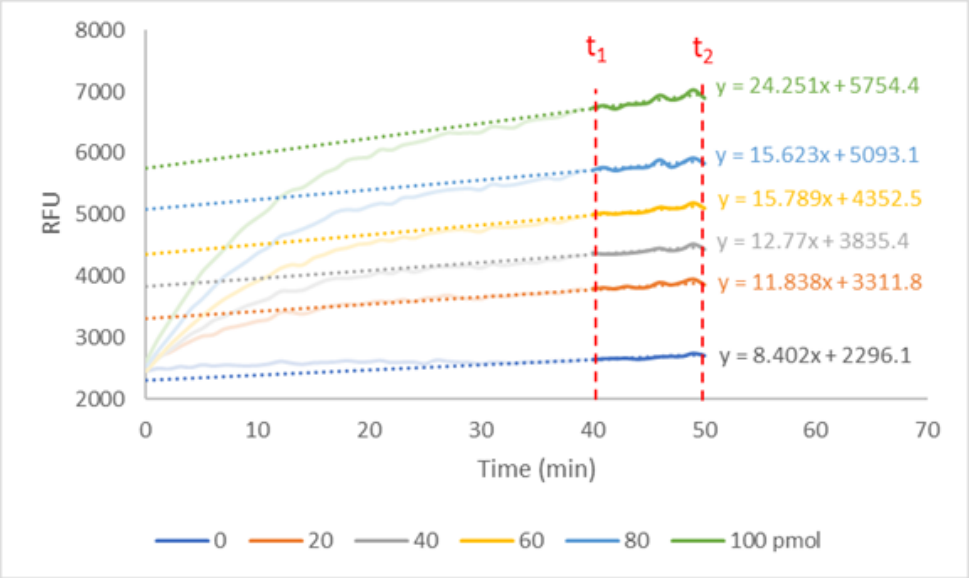

Fig. 11: Obtaining corresponding RFU values for glutamate standard curve.
Two fixed time points in the linear range must be selected for each measured standard. The straight line between the two time points is then extrapolated. The respective intersection with the y-axis results in the associated RFU value, which then reflects the value for the respective concentration. The standard curve can be plotted with the RFU values obtained in this way.

Subsequently the standard curve was plotted using the obtained and corrected intercept values. The Y-Intercept of the samples from the standard curve get B pmol of Glutamate formed during the reaction time ($\Delta t = t_2 - t_1$).

$$\text{Sample Glutamate Amount} = \frac{\boldsymbol{B}}{(\boldsymbol{V} * \boldsymbol{P})} * \boldsymbol{D} = \frac{pmol}{mg}$$

B is Glutamate amount from standard curve

V is sample volume added into the reaction well (0,0015 ml)

P is initial sample concentration in mg-protein/ml (mgP/ml)

D is sample dilution factor (10)

3.2.15 Electroretinogram recordings

The electroretinogram (ERG) is an electrophysiological test that measures the electrical potentials generated by the retina in response to a flash of light. The ERG results from currents flowing within the eye as a consequence of light-induced activity of neuronal and glial cells and can be analyzed as so-called a-, and b-waves emanating from specific cells or groups of cells [20]. One day before the measurements, the animals were dark adapted. On the day of the measurements, all handling was

performed under dim red light (used red filter: Rosco Supergel 27, Medium Red, #10273). Mice were anesthetized by an intraperitoneal injection of 0.1 ml/10 g body weight of anesthetic solution (1 ml of 100 mg/ml ketamine, 0.1 ml of 20 mg/ml xylazine, and 8.9 ml of 0,9 % NaCl). The pupils were dilated using a drop of 0,5 % tropicamide (Mydriaticum Stulln 0,5 %). Hypromellose (Methocel® 2 %) was applied to ensure the corneal hydration during the measurement. The mouse was placed on the heating pad of the device to maintain the body temperature at 37 °C and the golden loop electrodes were placed on the lower part of each cornea. The electrical potentials were recorded simultaneously from both eyes using an Espion E3 console which was connected to the Color Dome. Scotopic electroretinograms were recorded at white light flash intensities of -3, -2, -1.5, -1.0, 0.5 and 1.0 log (cd·s/m²). For photopic measurements, mice were adapted for 5 min to a background of white light at an intensity of 30 cd/m² to suppress the rods, and then recordings were continued at white light intensities of -0.5, 0, 0.5, 1, and 1.5 log (cd·s/m²). A-wave amplitudes were measured from the baseline to the peak of the negative a-wave (baseline to trough), b-wave amplitudes were measured from the trough of the a-wave to the peak of the positive b-wave (**Fig. 12**). For each animal, the mean response of both eyes was averaged. Data were analyzed using a two-way analysis of variance (ANOVA).

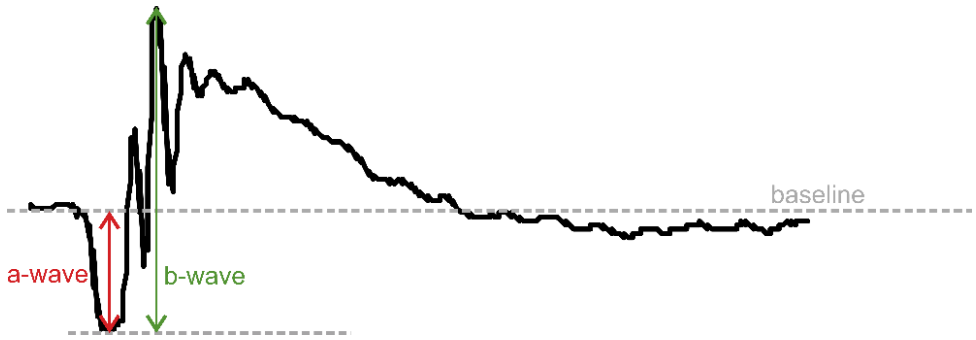

Fig. 12: Representative ERG response.
The a-wave amplitude reflects the distance between the baseline and the trough of the a-wave. The b-wave was measured from the trough of the a-wave to the peak of the b-wave.

4 Results

4.1. Upregulation of CD44 expression in Müller cells in RP retinas

In this study, the *Pde6b*^{STOP} mouse line was used as a retinitis pigmentosa (RP) model, where a floxed STOP cassette was inserted into intron 1 of the *Pde6b* gene [92]. Heterozygous *Pde6b*$^{STOP/WT}$ mice (also referred to as ST/WT), express PDE6B and therefore also have functioning rod photoreceptors. In homozygous *Pde6b*$^{STOP/STOP}$ mice (also referred to as ST/ST), the STOP cassettes cause loss of PDE6B and subsequent rod and cone degeneration.

In response to photoreceptor degeneration, other retinal cells react. In particular, Müller cells are one of the first cells to respond to stress, possibly leading to remodeling and cell death of other retinal cell types [44, 45]. For this reason, it is important to understand Müller cell remodeling in depth and to study early changes. One of these early responses in Müller cells to stress is that they upregulate the protein CD44, which is localized to the apical microvilli of Müller cells [79].

For this reason, we investigated the Müller cell response with respect to CD44 in the *Pde6b*$^{STOP/STOP}$ mice. To do so, retinas from *Pde6b*$^{STOP/WT}$ (ST/WT) and *Pde6b*$^{STOP/STOP}$ (ST/ST) mice were analyzed at 4 and 8 weeks of age. qRT-PCR analysis revealed that *Cd44* RNA expression was upregulated in 4- and 8-week-old ST/ST mice compared to age-matched ST/WT controls and that the amount of *Cd44* RNA increased with disease progression. In the 8-week-old ST/ST mice, CD44 expression was significantly higher than in ST/WT mice of the same age (**Fig. 13A**). Müller cells were visualized by immunofluorescence of glutamine synthetase (GLUL). The co-staining of GLUL and CD44 revealed, that CD44 is exclusively expressed by Müller cells and to a high extent in the apical microvilli of Müller cells. In addition, the counterstaining with Hoechst visualized the progressive thinning of the ONL over time in ST/ST compared to ST/WT retinas, demonstrating the progressive degeneration of photoreceptors in RP. Moreover, staining also showed that CD44 is upregulated in 4-week-old ST/ST mice compared to 4-week-old ST/WT mice, i.e., at an early stage of the disease with little photoreceptor degeneration (ONL thinning). This reflects the early response of Müller cells to stress conditions (**Fig. 13B**). Immunoblot analysis of CD44 confirmed CD44 upregulation in 4- and 8-week-old ST/ST mice compared to ST/WT controls on protein level (**Fig. 13C**). CD44 expression in 8-week-old ST/ST mice was even higher than in 4-week-old ST/ST mice, indicating that as photoreceptor degeneration progresses, CD44 expression also increases. Quantitative analysis of immunoblots validated significant upregulation of CD44 in 8-week-old ST/ST mice compared with 8-week-old ST/WT mice (**Fig. 13D**). Immunoblot analysis of PDE6B was used to confirm PDE6B deficiency in ST/ST mice (**Fig. 13C**).

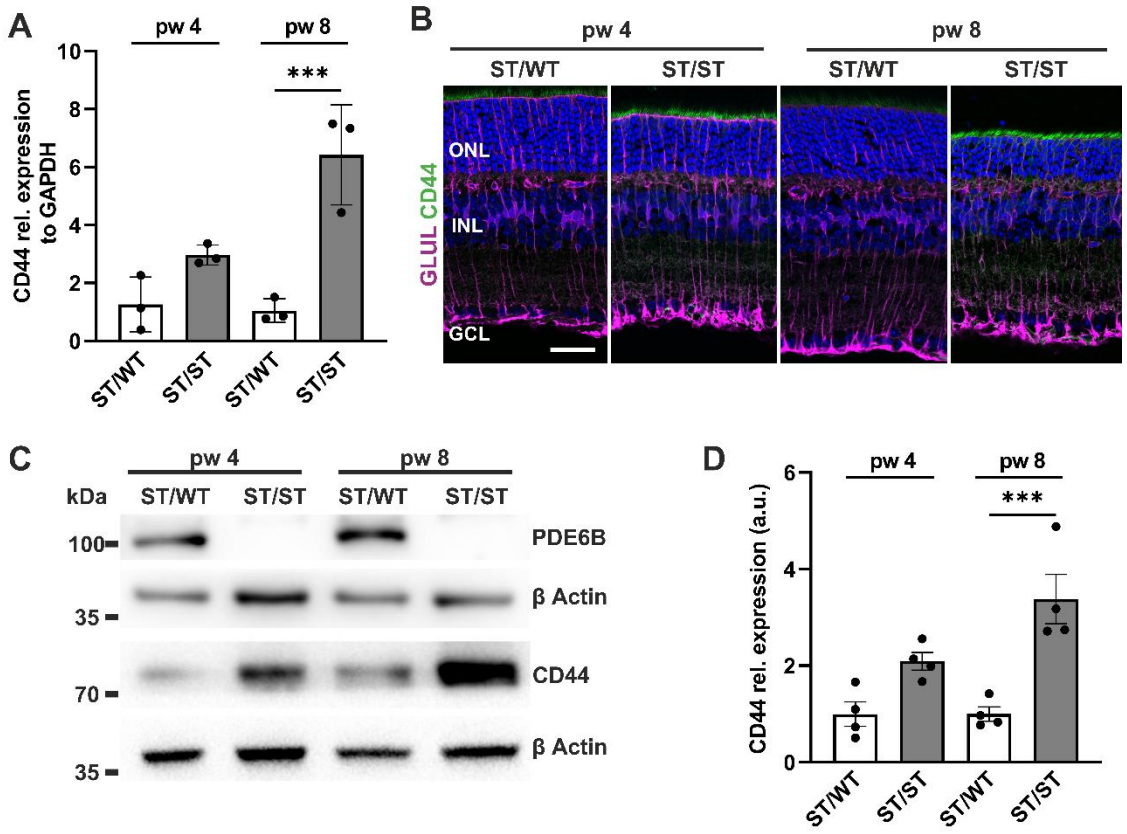

Fig. 13: Loss of PDE6B results in progressive photoreceptor degeneration and upregulation of CD44 expression in Müller glia cells.

(A-D) Retinas from *Pde6b*$^{STOP/WT}$ (ST/WT) and *Pde6b*$^{STOP/STOP}$ (ST/ST) mice were analyzed at 4 and 8 weeks of age. **(A)** Quantitative analysis of *Cd44* mRNA. Increased *Cd44* mRNA expression in 4- and 8-week-old ST/ST mice compared to age-matched ST/WT control. The highest level of *Cd44* mRNA was detected in 8-week-old ST/ST retinas (i.e., in the retina with the most extensive degeneration). Data, presented as mean ± SD. ANOVA, *** P < .001. **(B)** Representative images of retinal sections immunostained for glutamine synthetase (GLUL) to visualize Müller cells and for CD44. CD44 is upregulated in ST/ST mice and mainly expressed in the apical microvilli of Müller cells. Scale bar, 30 µm. **(C)** Representative PDE6B and CD44 immunoblots of retinal lysates. PDE6B is absent and CD44 is upregulated in ST/ST mice. b-Actin was used as a loading control. **(D)** Quantitative analysis of CD44 immunoblots. Increased CD44 expression in 4- and 8-week-old ST/ST mice compared to age-matched ST/WT control. The highest level of CD44 was detected in 8-week-old ST/ST retinas. Data, presented as mean ± SEM. ANOVA, *** P < .001.

Next, we analyzed the CD44 expression in retinas from three other retinal degeneration mouse models (**Fig. 14**). First, I investigated the *Pde6b*^{H620Q} mouse, an RP model, harboring a missense mutation in the catalytic domain of the *Pde6b* gene, that dramatically reduces expression of PDE6B [98]. Immunostaining of retinal sections showed a degeneration of the ONL in 4-week-old *Pde6b*^{H620Q} mice and an upregulation of CD44 compared to an age-matched wildtype control. A representative CD44 immunoblot validated the upregulation of CD44 expression compared to wildtype (**Fig. 14A**). Second, *Rho*$^{P23H/+}$ mice, another RP model, were studied. The autosomal dominant P23H mutation of the rhodopsin (*Rho*) gene leads to progressive retinal degeneration [99]. Immunostaining and

immunoblotting of *Rho*$^{P23H/+}$ retinas showed an increased CD44 expression compared to the wildtype animal (**Fig. 14B**). Third, the Cnga3-Rho-Opn4 triple-knockout (TKO) mouse was analyzed. These mice are completely blind from birth, because they lack functional photoreceptors or photosensitive retinal ganglion cells [100, 101]. In this mouse model, upregulation of CD44 was shown by staining and immunoblotting (**Fig. 14C**). In summary, photoreceptor degeneration leads to upregulation of CD44 expression in Müller cells, regardless of the underlying mutation.

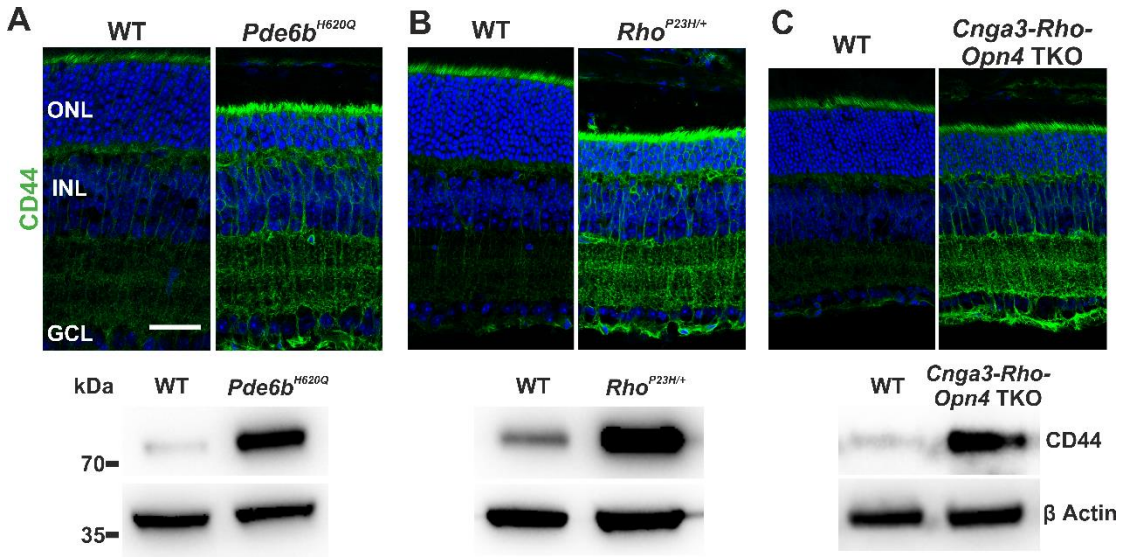

Fig. 14: Upregulation of CD44 expression in different retinal degeneration mouse models.
(A-C) Retinas from 3 retinal degeneration mouse models were analyzed: *Pde6b*^{H620Q} at 4 weeks of age, *Rho*$^{P23H/+}$ at 9 weeks of age, and *Cnga3*$^{-/-}$, *Rho*$^{-/-}$, *Opn4*$^{-/-}$ triple-knockout mice at 5 weeks of age. (**Upper panel**) Representative images of retinal sections immunostained for CD44 and counterstained with Hoechst 33342. Scale bar, 30 µm. (**Lower panel**) Representative CD44 immunoblots of retinal lysates. CD44 was upregulated in all 3 retinal degeneration mouse models. β-Actin was used as a loading control.

4.2 Effect of CD44 ablation on healthy and diseased retina

4.2.1 Morphological characterization of *Cd44*$^{-/-}$ *mice*

To investigate the role of CD44 in the retina, we used *Cd44*$^{-/-}$ mice, where a neomycin resistance/lacZ cassette disrupts exon 1 and part of intron 1, resulting in complete loss of CD44 transcription [93]. To confirm the loss of CD44 on the one hand and to check the antibody specificity on the other hand, an immunoblot was performed with retinas from 60-week-old *Cd44*$^{-/-}$, *Cd44*$^{+/-}$, and *Cd44*$^{+/+}$ mice (**Fig. 15A**). Homozygous *Cd44*$^{-/-}$ mice had no CD44 expression, whereas heterozygous *Cd44*$^{+/-}$ mice showed decreased CD44 expression compared to *Cd44*$^{+/+}$ wildtype mice. Since CD44 is a Müller cell-specific protein, and Müller cells often undergo reactive gliosis in response to stress [102], glial fibrillary acidic protein (GFAP) expression was also examined. Immunoblot analysis of GFAP showed comparatively

similar levels of the protein in all three mouse groups, indicating that ablation of CD44 did not lead to reactive gliosis in Müller cells. Furthermore, glutamine synthetase (GLUL) a common marker for Müller cells and a key enzyme in neurotransmitter recycling [103] also showed no differences between the three mouse groups (**Fig. 15A**). Immunolabeling with CD44 also revealed weaker CD44 expression in the heterozygous *Cd44*$^{+/-}$ mouse and total ablation of the protein in the homozygous *Cd44*$^{-/-}$ mouse. In line with the immunoblot, GLUL expression remained unchanged between groups in retinal sections (**Fig. 15B**).

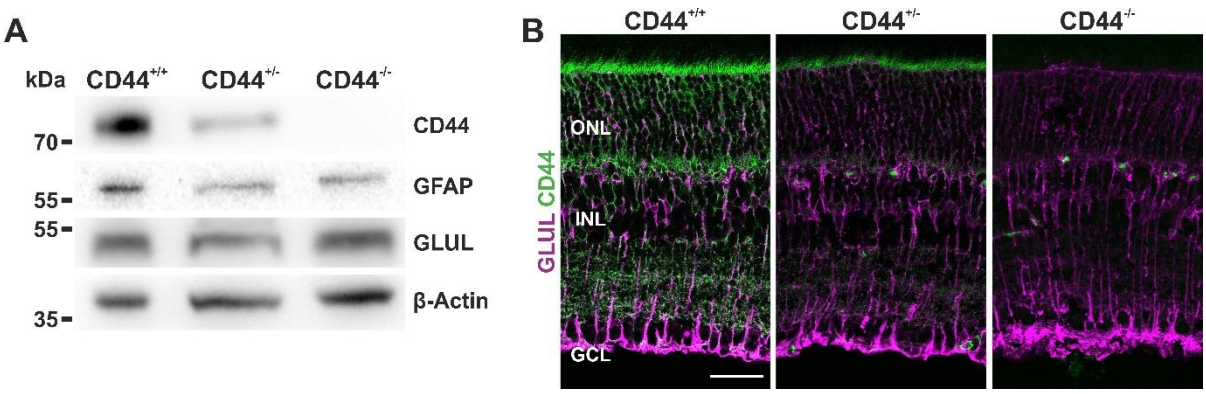

Fig. 15: Validation of CD44 knockout in CD44$^{-/-}$ mice.
Retinas from *CD44*$^{-/-}$, *CD44*$^{+/-}$, and *CD44*$^{+/+}$ mice were analyzed at 60 weeks of age. **(A)** Representative CD44, GFAP, and GLUL immunoblots of retinal lysates. CD44 was downregulated in *CD44*$^{+/-}$ mice compared to *CD44*$^{+/+}$ mice and absent in *CD44*$^{-/-}$ mice. GFAP and GLUL had similar expression levels in *CD44*$^{+/+}$, *CD44*$^{+/-}$, and *CD44*$^{-/-}$ mice. β-Actin was used as a loading control. **(B)** Representative images of retinal sections immunostained for GLUL and CD44. CD44 was downregulated in *CD44*$^{+/-}$ mice and absent in *CD44*$^{-/-}$ mice. Scale bar, 35 µm.

4.2.2 Morphological characterization of *Cd44*$^{-/-}$ *Pde6b*$^{STOP/STOP}$ mice

To elucidate the role of CD44 in the context of RP, the *CD44*$^{-/-}$ mice were crossed with the *Pde6b*^{STOP} line. Thus, ST/WT and ST/ST mice with ablated CD44 expression were obtained (CD44$^{-/-}$ ST/WT, CD44$^{-/-}$ ST/ST).

To confirm the absence of CD44 in the new mouse line, the mRNA and protein levels of 8-week-old mice were investigated (**Fig. 16**). qRT-PCR analysis validated the loss of *Cd44* RNA in both CD44$^{-/-}$ ST/WT, and CD44$^{-/-}$ ST/ST mice (**Fig. 16A**). Immunoblot analysis of CD44 confirmed CD44 loss in 8-week-old CD44$^{-/-}$ ST/WT, and CD44$^{-/-}$ ST/ST mice on protein level (**Fig. 16B**). Immunofluorescence labeling of CD44 revealed that CD44 was absent in CD44$^{-/-}$ ST/WT, and CD44$^{-/-}$ ST/ST mice (**Fig. 16C**). In line with previous experiments (**Fig. 13**), CD44 was upregulated in Müller cells of ST/ST mice compared to ST/WT on both RNA and protein level (**Fig. 16A,B**).

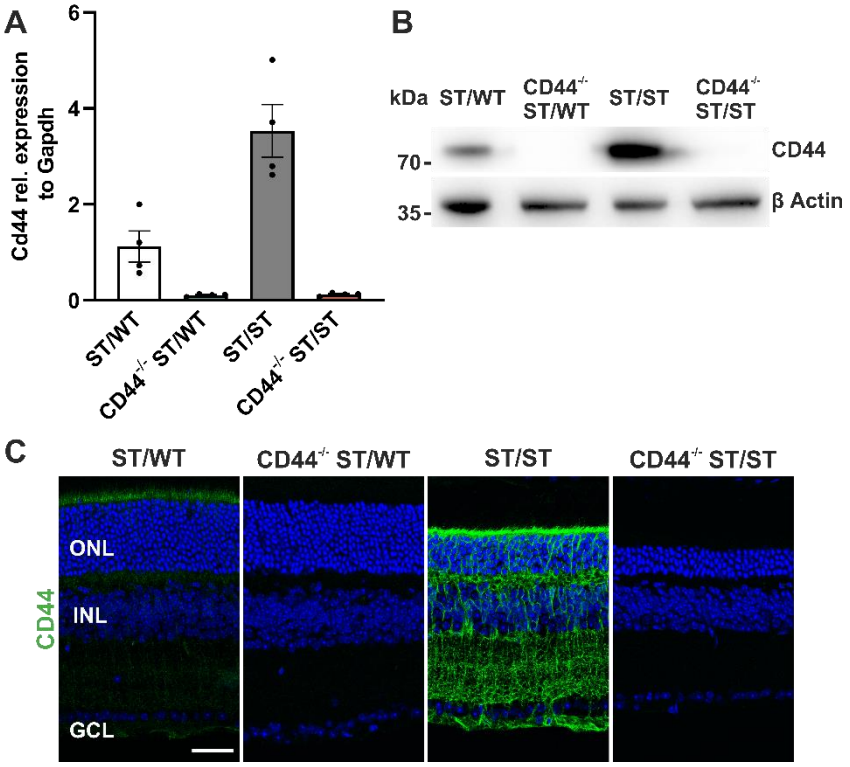

***Fig. 16:* CD44$^{-/-}$ ST/WT and CD44$^{-/-}$ ST/ST mice show no CD44 expression.**
(A-C) Retinas from *Pde6b*$^{STOP/WT}$ (ST/WT), *Cd44*$^{-/-}$ *Pde6b*$^{STOP/WT}$ (CD44$^{-/-}$ ST/WT), ST/ST, and CD44$^{-/-}$ ST/ST mice were analyzed at 8 weeks of age. Absence of CD44 mRNA and protein expression in CD44$^{-/-}$ ST/WT and CD44$^{-/-}$ ST/ST mice. **(A)** Quantitative analysis of *Cd44* by qPCR. Data presented as mean ± SEM. ANOVA, *** P < .001. **(B)** Representative CD44 immunoblot of retinal lysates. β-Actin was used as a loading control. **(C)** Representative images of retinal sections immunostained for CD44 to visualize the loss of CD44 in CD44$^{-/-}$ ST/WT and CD44$^{-/-}$ ST/ST mice. Scale bar, 25 µm.

Müller cells undergo gliosis under stress conditions [65]. To understand the role of CD44 in gliosis, we examined the new mouse models *Cd44*$^{-/-}$ *and Cd44*$^{-/-}$ *Pde6b*$^{STOP/STOP}$ for the gliosis marker GFAP at 8 weeks of age (**Fig. 17**). For this purpose, qRT-PCR (**Fig. 17A**), immunoblotting (**Fig. 17B**), and immunostaining (**Fig. 17C**) were performed. The mRNA levels of *Gfap* were not altered between ST/WT and CD44$^{-/-}$ ST/WT and between ST/ST and CD44$^{-/-}$ ST/ST mice, respectively. In line with Figure 13, *Cd44* RNA levels were significantly higher in ST/ST and CD44$^{-/-}$ ST/ST mice compared to ST/WT and CD44$^{-/-}$ ST/WT mice, respectively (**Fig. 17A**). Immunoblot analysis showed no detectable GFAP expression in ST/WT and CD44$^{-/-}$ ST/WT mice and comparable GFAP levels between ST/ST and CD44$^{-/-}$ ST/ST mice (**Fig. 17B**). Immunostaining for GFAP also confirmed similar expression levels in ST/WT and CD44$^{-/-}$ ST/WT mice and a similar upregulation of GFAP in ST/ST and CD44$^{-/-}$ ST/ST mice (**Fig. 17C**). Taken together, these data showed that knockout of CD44 did not affect gliosis.

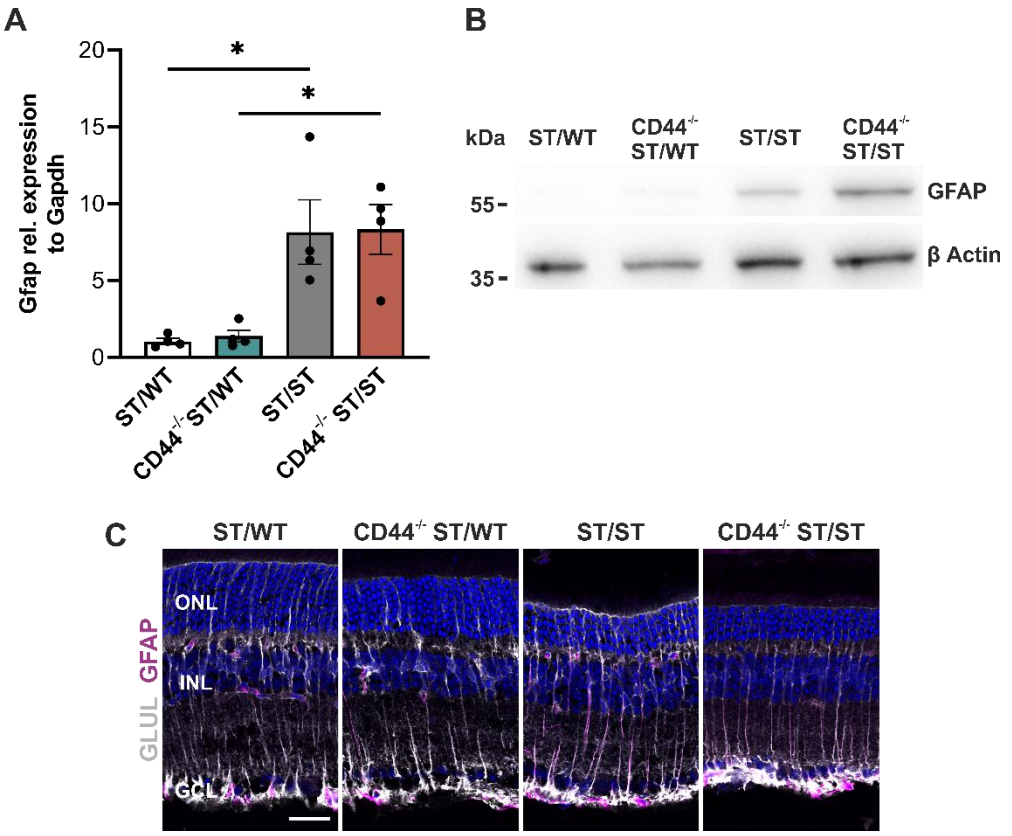

Fig. 17: Retinas from CD44$^{-/-}$ ST/ST mice have a similar GFAP level as ST/ST mice.
(A-C) Retinas from ST/WT, CD44$^{-/-}$ ST/WT, ST/ST, and CD44$^{-/-}$ ST/ST mice were analyzed for GFAP expression at 8 weeks of age. Increased GFAP mRNA and protein expression in ST/ST and CD44$^{-/-}$ ST/ST mice compared to age-matched ST/WT and CD44$^{-/-}$ ST/WT control. CD44 does not affect GFAP expression. No differences in *Gfap* mRNA and GFAP protein expression between ST/WT and CD44$^{-/-}$ ST/WT and no difference between ST/ST and CD44$^{-/-}$ ST/ST mice. **(A)** Quantitative analysis of GFAP mRNA by qRT-PCR. Data, presented as mean ± SEM. ANOVA, *** P < .001. **(B)** Representative GFAP immunoblot of retinal lysates. β-Actin was used as a loading control. **(C)** Representative images of retinal sections immunostained for GLUL and GFAP. Scale bar, 25 µm.

To determine whether ablation of CD44 affects the retinal morphology and disease progression of RP, we quantified the ONL thickness and cone inner and outer segment (IS/OS) length in ST/WT, CD44$^{-/-}$ ST/WT, ST/ST, and CD44$^{-/-}$ ST/ST mice at 300 µm distance from the optic nerve at the ventral side of the retina (**Fig. 18**). Mice were studied at 3, 4, 8, and 12 weeks of age. Immunofluorescence of sections was conducted for cone arrestin (Arr3) and Hoechst 33342 to visualize cone photoreceptors and the photoreceptor nuclei (ONL), respectively (**Fig. 18A**). At 3 weeks of age, after the retina is fully developed [104], the ONL thickness of ST/WT and CD44$^{-/-}$ ST/WT mice were 65 µm ± 4.0 µm and 67 µm ± 2.1 µm respectively, while in ST/ST and CD44$^{-/-}$ ST/ST mice the ONL thickness was 51 µm ± 1.8 µm and 60 µm ± 2.1 µm, respectively. These findings demonstrate that CD44 does not influence photoreceptor development. In ST/WT mice, ONL thickness decreased due to programmed cell death between three and four weeks of age to 59 µm ± 2.8 µm and remained constant thereafter until 12 weeks of age. In CD44$^{-/-}$ ST/WT mice, the decrease in ONL thickness between three and four weeks

of age to 50 µm ± 1.9 µm was greater compared to ST/WT mice. These data suggest an additional CD44-related cell death. Between 4 to 12 weeks of age, the ONL thickness of CD44$^{-/-}$ ST/WT mice remained constant. The difference between ST/WT (59 µm ± 2.8 µm) and CD44$^{-/-}$ ST/WT (50 µm ± 1,9 µm) at 4 weeks of age was significant with $P < 0.02$. In 8-week-old animals the ONL of CD44$^{-/-}$ ST/WT mice (52 µm ± 1.9 µm) was thinner compared to ST/WT (58 µm ± 2.2 µm), but the difference was not significant. At 12 weeks of age the ONL thickness of ST/WT and CD44$^{-/-}$ ST/WT mice were 57 µm ± 1.8 µm and 53 µm ± 2.1 µm, respectively.

In ST/ST and CD44$^{-/-}$ ST/ST mice, the ONL degenerates over time with a ONL thickness of 17 µm ± 0.8 µm and 11 µm ± 0.8 µm at 12 weeks of age, respectively ($p < 0.03$) (**Fig. 18B**, left panel).

The quantification of cone IS and OS revealed that ablation of CD44 had no effect on the development of cones. At 3 weeks of age, after the retina is fully developed, the cone IS and OS length of ST/WT and CD44$^{-/-}$ ST/WT mice were 21 µm ± 0.3 µm (SEM) and 22 µm ± 0.7 µm (SEM), respectively, while in ST/ST and CD44$^{-/-}$ ST/ST mice the cone IS and OS length was 19 µm ± 0.7 µm (SEM) and 22 µm ± 0.2 µm (SEM). After 4, 8 and 12 weeks the cone IS and OSs length decreased in CD44$^{-/-}$ ST/WT mice compared to ST/WT, which lead to a significant difference at all three timepoints. The IS and OS of cones in CD44$^{-/-}$ ST/ST mice compared to the ST/ST group were also shorter after 4, 8 and 12 weeks, with a significant difference only at 4 weeks with $P < 0.002$ (**Fig. 18B**, right panel).

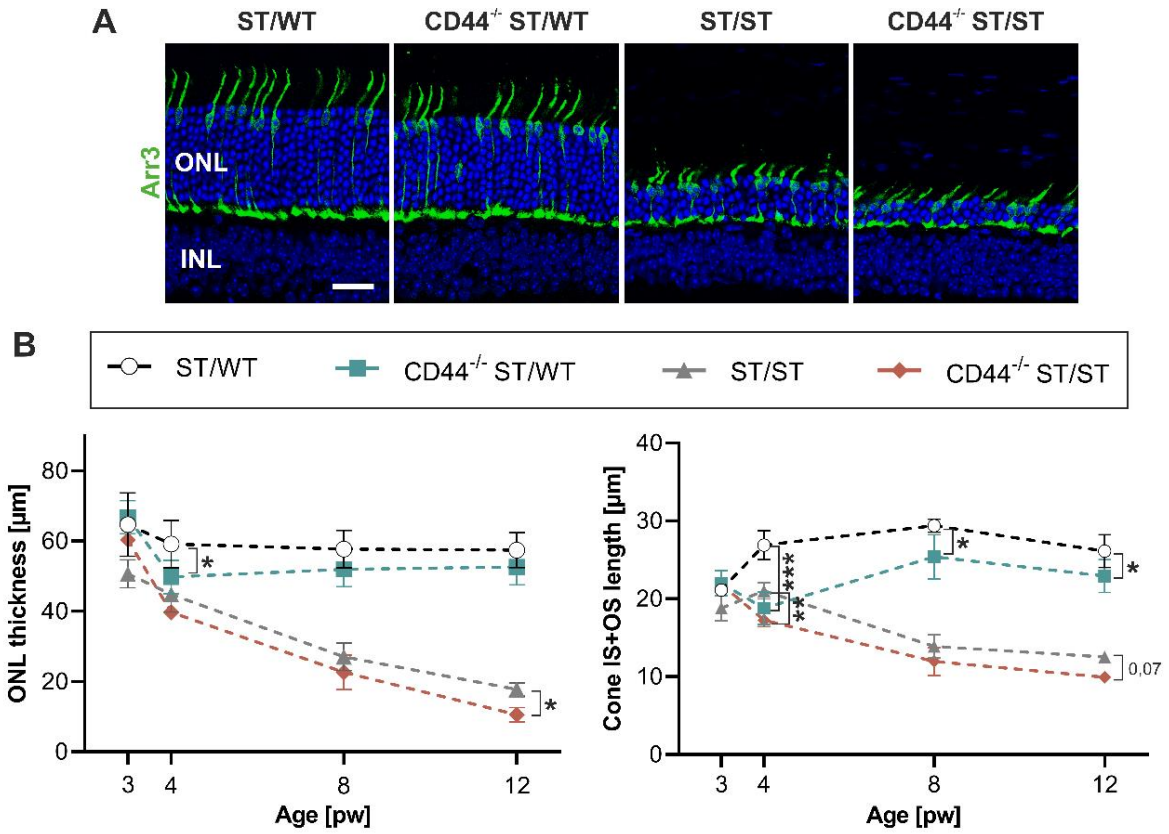

Fig. 18: CD44$^{-/-}$ ST/ST mice show enhanced disease progression in comparison with ST/ST mice.
(A) Representative images of retinal sections from 12-week-old mice immunostained for Arr3 to visualize the cones and counterstained with Hoechst. Staining of photoreceptor nuclei showed more rapid ONL thinning in CD44$^{-/-}$ ST/ST mice compared to ST/ST mice. Scale bar, 25 µm. **(B)** Retinas from ST/WT, CD44$^{-/-}$ ST/WT, ST/ST, and CD44$^{-/-}$ ST/ST mice were analyzed at 3, 4, 8, and 12 weeks of age. Quantification of ONL thickness and cone inner and outer segment length at 300 µm distance from the optic nerve. ONL was significantly thinner in 12-week-old CD44$^{-/-}$ ST/ST mice compared to ST/ST mice. Cone inner and outer segments were significantly shorter in CD44$^{-/-}$ ST/WT compared to ST/WT mice at 4, 8, and 12 weeks of age. pw3, n = 5 per group. pw4, n = 6 per group. pw8, n = 5 for ST/WT, and ST/ST, n = 7 for CD44$^{-/-}$ ST/WT, n = 6 for CD44$^{-/-}$ ST/ST. pw12, n = 8 for ST/WT, n = 6 for CD44$^{-/-}$ ST/WT, and CD44$^{-/-}$ ST/ST, n = 5 for ST/ST. Data, presented as mean ± SEM. ANOVA, *** P < .001.

In addition to the loss of photoreceptors in RP, there is also remodeling of the inner retina [44]. Next, we analyzed remodeling in our CD44$^{-/-}$ ST/WT and CD44$^{-/-}$ ST/ST compared to ST/WT and ST/ST mice, respectively.

To evaluate the effect of CD44 loss on rod bipolar cells, rod bipolar cells were stained with an antibody against the protein kinase (PKC)-α (**Fig. 19**). PKC-α is abundant in retinal bipolar cells [105] and the antibody labels the cell bodies, axons, and dendrites of rod bipolar cells. Rod bipolar cells of 12-week-old ST/WT retinas showed long, dense, and bushy dendritic arborization in the outer plexiform layer (OPL) with numerous dendrites irradiating from the cell. In contrast, CD44$^{-/-}$ ST/WT mice showed shorter dendrites, which at the same time appeared less bushy (**Fig. 19A**; arrowheads). In 12-week-old ST/ST retinas, the rod bipolar cell dendrites appeared shorter and spatially disordered compared to

the ST/WT retina. This effect was even more pronounced in the rod bipolar cell dendrites of the CD44$^{-/-}$ ST/ST mice compared to the ST/ST mice (**Fig. 19A**; arrowheads). To quantify this observation, the area of the rod bipolar cell dendrites was analyzed in retinal sections (**Fig. 19B**). In ST/ST mice, the dendritic area was significantly reduced compared to age-matched ST/WT mice. In CD44$^{-/-}$ ST/WT mice, the dendrite area also was significantly reduced compared to ST/WT mice, whereas there was no significant difference between CD44$^{-/-}$ ST/ST and ST/ST mice.

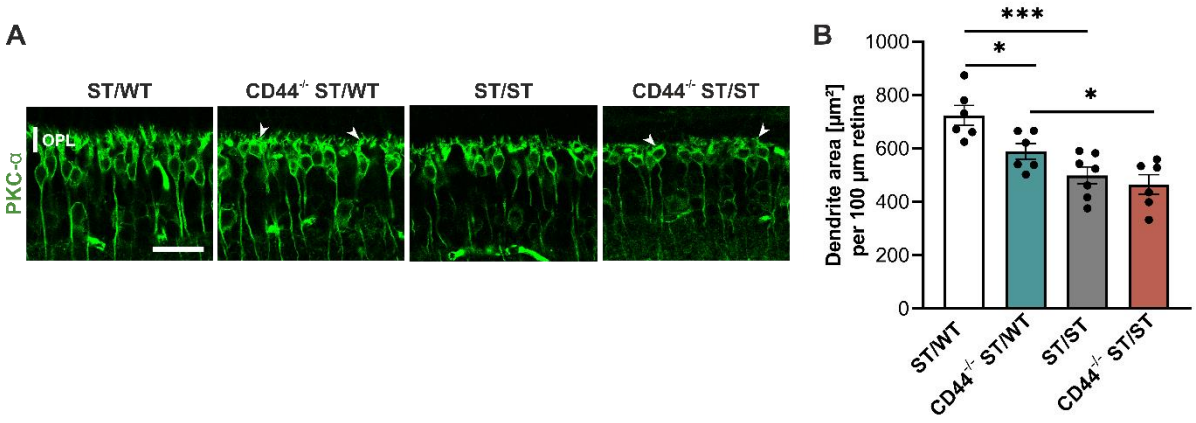

Fig. 19: Loss of CD44 leads to rod bipolar cell remodeling.
(A-B) Retinas from ST/WT, CD44$^{-/-}$ ST/WT, ST/ST, and CD44$^{-/-}$ ST/ST mice were analyzed for rod bipolar cell remodeling at 12 weeks of age. **(A)** Retinal sections were labeled with anti-PKC–α antibodies to visualize rod bipolar cells, particularly their processes in the OPL. Arrowheads indicate the shorter and less-branched dendrites of CD44$^{-/-}$ ST/WT and CD44$^{-/-}$ ST/ST mice compared to ST/WT and ST/ST mice, respectively. The rod bipolar cell dendrites of ST/ST and CD44$^{-/-}$ ST/ST mice were shorter in comparison with the corresponding wildtype control. Scale bar, 25 µm. **(B)** Quantification of rod bipolar cell dendritic area was based on immunostaining of retinal sections with PKC-α. The dendrite area corresponds to the area of 100 µm retinal slices and was calculated using ImageJ. In both ST/ST and CD44$^{-/-}$ ST/WT mice, the dendrite area of rod bipolar cells was significantly smaller compared to ST/WT mice. Additionally, a notable decrease in dendrite area was observed between CD44$^{-/-}$ ST/WT and CD44$^{-/-}$ ST/ST mice, while no significant decrease was found among the RP mouse groups. Data represent individual values, presented as mean ± SEM. T-test, * P ≤ 0.05; ** P ≤ 0.01; *** P ≤ 0.001.

Next, retinal sections from 12-week-old mice were stained with antibodies against secretagogin (SCGN) to analyze ON and OFF cone bipolar cells. SCGN is expressed in the dendrites, soma, and axon terminals of cone bipolar cells [106] (**Fig. 20**). The cone bipolar cells from ST/WT mice have a large dendritic process that emerges from the cell body and then branches further into smaller dendrites in the OPL (**Fig. 20A**). In contrast, in 12-week-old CD44$^{-/-}$ ST/WT mice, the dendrites appeared thinner and less branched. The same applies to the comparison between ST/ST and CD44$^{-/-}$ ST/ST mice: the dendrites in the OPL appeared to be thinner and less branched in CD44$^{-/-}$ ST/ST compared to ST/ST mice. The changes described are reflected in the quantification but are not significant (**Fig. 20B**).

Significant reductions in dendritic area were observed exclusively between ST/WT and ST/ST retinas, as well as between CD44$^{-/-}$ ST/WT and CD44$^{-/-}$ ST/ST retinas (**Fig. 20B**).

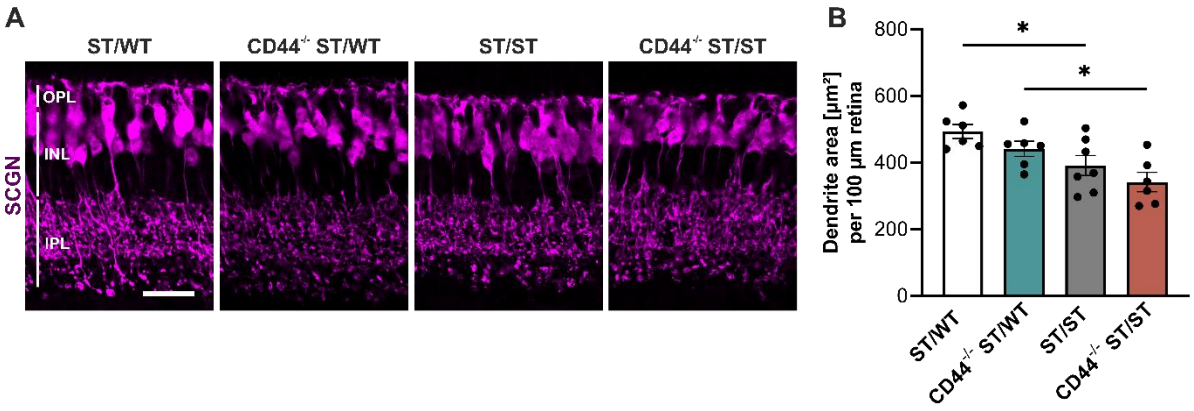

Fig. 20: Effect of CD44 ablation on cone bipolar cell dendrites.
(A-B) Retinas from ST/WT, CD44$^{-/-}$ ST/WT, ST/ST, and CD44$^{-/-}$ ST/ST mice were analyzed for cone bipolar cell remodeling at 12 weeks of age. **(A)** Retinal sections were labeled with SCGN antibody to visualize cone bipolar cells, particularly their dendrites in the OPL. CD44$^{-/-}$ ST/WT and CD44$^{-/-}$ ST/ST mice had shorter cone bipolar cell dendrites compared to ST/WT and ST/ST mice, respectively. Scale bar, 25 µm. **(B)** Quantification of the cone bipolar cell dendritic area was based on immunostaining of retinal sections with SCGN. The dendrite area corresponds to the area of 100 µm retinal slices and was calculated using ImageJ. The dendritic area from ST/ST and CD44$^{-/-}$ ST/ST mice was significantly smaller compared to ST/WT and CD44$^{-/-}$ ST/WT mice, respectively. The dendritic area decreased in CD44$^{-/-}$ ST/WT and CD44$^{-/-}$ ST/ST mice compared to ST/WT and ST/ST mice, respectively, but not significant. Data represent individual values, presented as mean ± SEM. T-test, * $P \leq 0.05$; ** $P \leq 0.01$; *** $P \leq 0.001$.

To examine changes in the horizontal cells, horizontal cells were visualized using the calbindin-D28kD antibody (**Fig. 21**). Calbindin is present in cell bodies and dendrites of the horizontal cells [107]. Horizontal cells of 12-week-old ST/WT mice have a dense dendritic pattern with “rosette”-like clusters of dendritic terminals in the OPL (**Fig. 21A**). This rosette-like arrangement of dendrite terminals decreased in CD44$^{-/-}$ ST/WT mice and was absent in ST/ST and CD44$^{-/-}$ ST/ST (**Fig. 21A**). The quantitative analysis of the horizontal cell dendritic area revealed a significant decrease between ST/ST and ST/WT mice and between CD44$^{-/-}$ ST/WT and CD44$^{-/-}$ ST/ST mice. The total length of dendrites and the degree of branching also decreased between ST/ST and CD44$^{-/-}$ ST/ST retinas, although the difference was not significant (**Fig. 21B**).

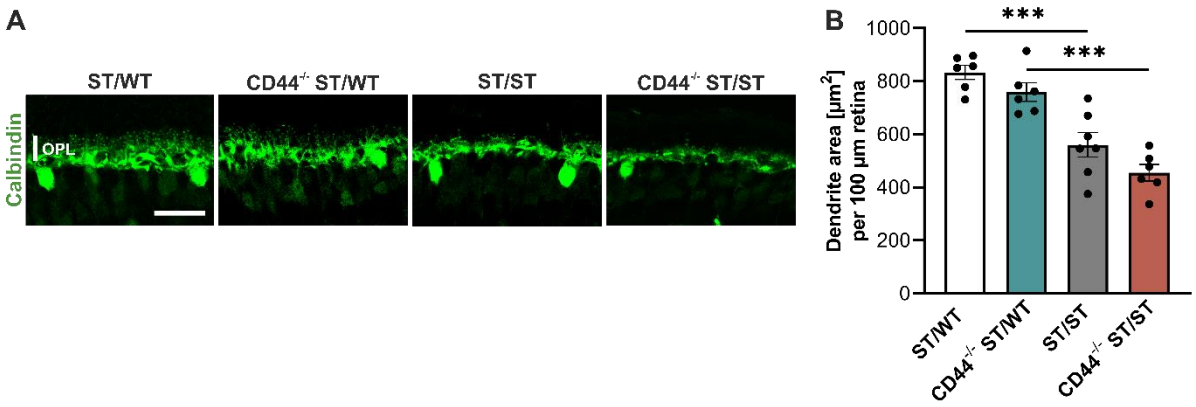

Fig. 21: Effect of CD44 loss on horizontal cell dendrites.
(A-B) Retinas from ST/WT, CD44$^{-/-}$ ST/WT, ST/ST, and CD44$^{-/-}$ ST/ST mice were analyzed for horizontal cell remodeling at 12 weeks of age. **(A)** Retinal sections were labeled with calbindin antibody to visualize horizontal cells, particularly their dendrites in the OPL. CD44$^{-/-}$ ST/WT and CD44$^{-/-}$ ST/ST mice showed a less dense and less branched dendritic pattern than ST/WT and ST/ST mice, respectively. Scale bar, 25 µm. **(B)** Quantification of horizontal cell dendritic area from retinal sections immunostained with calbindin. The dendrite area corresponds to the area of 100 µm retinal slices and was calculated using ImageJ. The dendritic area from ST/ST and CD44$^{-/-}$ ST/ST mice was significantly smaller compared to ST/WT and CD44$^{-/-}$ ST/WT mice, respectively. The dendritic area decreased in CD44$^{-/-}$ ST/WT and CD44$^{-/-}$ ST/ST mice compared to ST/WT and ST/ST mice, respectively, but not significant. Data represent individual values and mean ± SEM. T-test, * P ≤ 0.05; ** P ≤ 0.01; *** P ≤ 0.001.

4.2.3 Investigation of a pro-inflammatory response in *Cd44$^{-/-}$ Pde6b$^{STOP/STOP}$* mice

Inflammation is a common feature of RP, and neuroinflammation has been shown to accompany photoreceptor degeneration [108]. Microglia, the resident immune cells of the retina, are involved in maintaining tissue integrity and homeostasis. Under physiological conditions, microglia exhibit a resting, ramified state characterized by numerous, extending processes emerging from a round and small soma. In response to stress, retinal microglia become reactive, lose their long cellular processes, and may kill photoreceptors by phagocytosis and accelerate disease progression [108–112]. Due to their different functions in healthy and diseased retina, we quantified the total number of activated microglia in retinal sections of 4-, 8-, and 12-week-old-mice (**Fig. 22**). To do so, sections were stained with antibodies against Iba1 and CD68 and used for quantitative analysis. Iba1 is a marker for microglia cells [113] and CD68 is expressed by phagocytosing macrophages [114]. At 12-weeks-of-age, the microglia had a resting, ramified morphology and were located between the IPL and the OPL of ST/WT, CD44$^{-/-}$ ST/WT, and ST/ST mice. In contrast, in retinas from 12-week-old CD44$^{-/-}$ ST/ST mice, microglia were activated with extending processes and were located in the ONL (**Fig. 22A**). For quantification, microglia positive for Hoechst 33342, Iba1, and CD68 were counted. CD44$^{-/-}$ ST/WT mice had a slightly higher number of activated microglia compared to ST/WT at 4 and 8 weeks of age. In 12-week-old CD44$^{-/-}$ ST/WT retinas, the number of activated microglia returned to the level observed in ST/WT

retinas. CD44$^{-/-}$ ST/ST retinas showed higher numbers of activated microglia compared with ST/ST retinas at all ages. In CD44$^{-/-}$ ST/ST mice the number of microglia increased in parallel with disease progression. At 12 weeks of age, microglia number was significantly higher in CD44$^{-/-}$ ST/ST compared to ST/ST mice (**Fig. 22B**).

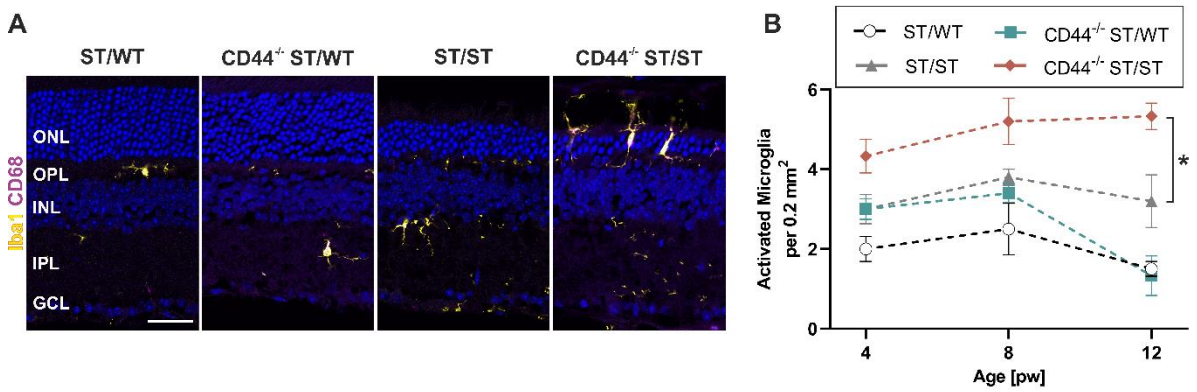

Fig. 22: Increased microglia activation in CD44$^{-/-}$ ST/ST mice in comparison with ST/ST mice.
(A) Representative images of retinal sections from 12-week-old mice immunostained for Iba1 and CD68 to visualize microglia and phagocytic microglia, respectively. Scale bar, 35 µm. **(B)** Quantification of activated microglia in 4, 8, and 12-week-old ST/WT, CD44$^{-/-}$ ST/WT, ST/ST, and CD44$^{-/-}$ ST/ST mice. CD44$^{-/-}$ ST/ST retinas had a significantly higher number of activated microglia compared to ST/ST retinas. pw4, n = 5 for ST/WT, n = 6 for CD44$^{-/-}$ ST/WT, ST/ST, and CD44$^{-/-}$ ST/ST. pw8, n = 4 for ST/WT, n = 5 for CD44$^{-/-}$ ST/WT, ST/ST, and CD44$^{-/-}$ ST/ST. pw12, n = 8 for ST/WT, n = 6 for CD44$^{-/-}$ ST/WT, and CD44$^{-/-}$ ST/ST, n = 5 for ST/ST. Data, presented as mean ± SEM. ANOVA, *** P < .001.

Activated phagocytic microglia express pro-inflammatory factors such as TNFα and IL-6, which have the ability to activate NF-κB signaling, leading to a cascade of downstream effects [110, 115]. To determine whether the increased number of activated microglia in the CD44$^{-/-}$ ST/ST retina also led to increased secretion of those pro-inflammatory factors, qRT-PCR analysis of 8-week-old ST/WT, CD44$^{-/-}$ ST/WT, ST/ST, and CD44$^{-/-}$ ST/ST mice was performed. The RNA levels of TNFα and NF-κB were significantly elevated in CD44$^{-/-}$ ST/ST retinas compared to ST/WT and CD44$^{-/-}$ ST/WT retinas, whereas they were not different between ST/WT and CD44$^{-/-}$ ST/WT retinas (**Fig. 23A-B**). TNFα also appeared to be increased in CD44$^{-/-}$ ST/ST retina compared with ST/ST, although this difference was not significant (**Fig. 23A**). IL-6 RNA expression was slightly increased in CD44$^{-/-}$ ST/ST retinas compared with ST/WT, CD44$^{-/-}$ ST/WT and ST/ST retinas, but this difference was not significant between any of the groups (**Fig. 23C**). These results are also consistent with the total number of activated microglia in 8-week-old mice: here, only the number of activated microglia was increased in the CD44$^{-/-}$ ST/ST mice compared with the CD44$^{-/-}$ ST/WT, ST/WT, and ST/ST group (**Fig. 22B**).

In conclusion, increased activation of microglia in CD44$^{-/-}$ ST/ST mice was associated with increased secretion of the proinflammatory factor TNFα along with increased activation of the NF-kb pathway.

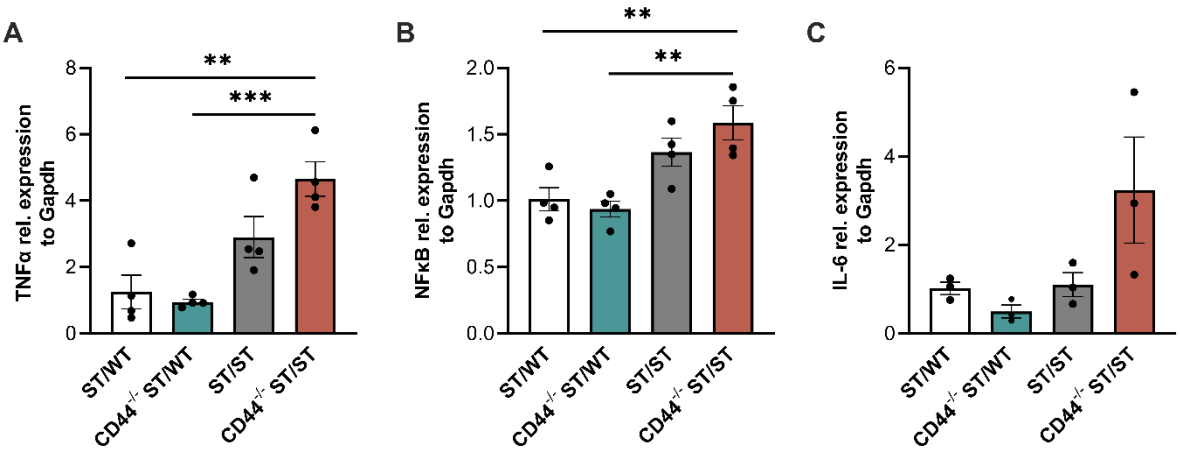

Fig. 23: Increased TNFα, NF-κB, and IL-6 RNA expression in CD44$^{-/-}$ ST/ST retinas.
(A-C) ST/WT, CD44$^{-/-}$ ST/WT, ST/ST, and CD44$^{-/-}$ ST/ST retinas were analyzed at 8 weeks of age. RNA of all samples was isolated and used for qRT-PCR of pro-inflammatory factors. Results were normalized to *Gapdh*. TNFα and NF-κB RNA was significantly elevated in CD44$^{-/-}$ ST/ST compared to CD44$^{-/-}$ ST/WT and ST/WT retinas. TNFα and NF-κB levels were higher in CD44$^{-/-}$ ST/ST retinas compared with ST/ST retinas, but not significant. IL-6 RNA expression wasn't significantly altered between the groups, but it seemed to be increased in CD44$^{-/-}$ ST/ST compared with ST/ST retinas. Data are presented as mean ± SEM. ANOVA, *** P < .001.

4.2.4 Effect of CD44 ablation on retinal function

The morphological characterization (chapter 4.2.2) from ST/WT, CD44$^{-/-}$ ST/WT, ST/ST, and CD44$^{-/-}$ ST/ST mice showed that CD44 ablation in ST/ST retinas resulted in an increased degeneration of photoreceptors and remodeling of the inner retina. Furthermore, the degeneration is accompanied by an increased inflammatory response. To test whether these morphologically abnormalities impact retinal function, full-field single-flash electroretinography (ERG) responses were recorded in 8-week-old mice. ERG is a useful tool to measure electrical responses of retinal cells to a light stimulus to assess retinal function [116]. The a-wave is the negative deflection and represents a direct measure of the photoreceptor response. The b-wave is the positive deflection and is generated by cells in the inner retina, mainly the bipolar cells [117]. In the scotopic range, up to the luminance of -2.0 log (cd*s/m^2), only rod photoreceptors are activated. In the mesopic range, with higher luminances than -2.0 log (cd*s/m^2) both rod and cone photoreceptors are activated [118]. At higher light levels, i.e., luminances of 3.0 log (cd*s/m^2) and higher, rods are completely saturated, and vision is mediated by signals from cone photoreceptors [119]. The bipolar cells represent an amplification of the rod signals in the dark-adapted retina, which explains the detection of the b-wave with less luminous stimuli [117].

In 8-week-old ST/WT mice, the scotopic a-wave amplitude increased with increasing light stimuli and a clear a-wave was detected at -1.0 log (cd*s/m^2) (**Fig. 24A**), which is also reflected by the

representative ERG curves (**Fig. 24C**). Conversely, in CD44$^{-/-}$ ST/WT mice, the a-wave was less pronounced and significantly smaller compared to ST/WT mice at luminances of 0.5 log (cd*s/m^2) and 1.0 log (cd*s/m^2). In CD44$^{-/-}$ ST/ST and ST/ST mice, the a-wave was almost completely absent (**Fig. 24A,C**). The a-wave of CD44$^{-/-}$ ST/ST mice was significantly smaller compared to ST/ST mice at 0.5 and 1.0 log (cd*s/m^2) (**Fig. 24A**). At 1.0 log (cd*s/m^2), the mean amplitude of CD44$^{-/-}$ ST/WT was 76 % of that of the ST/WT animals and the mean amplitude of CD44$^{-/-}$ ST/ST retinas was 33 % of that of ST/ST.

The b-wave was detected at -3.0 log (cd*s/m^2) in ST/WT, CD44$^{-/-}$ ST/WT and ST/ST, but not in CD44$^{-/-}$ ST/ST mice (**Fig. 24C**). The b-wave also increased with increasing light intensities. It is important to note that at the highest measured light intensity of 1.0 log (cd*s/m^2) the b-wave amplitude of CD44$^{-/-}$ ST/WT mice was with 81 % significantly lower than that of ST/WT mice. The b-wave amplitudes of CD44$^{-/-}$ ST/ST retinas were slightly but not significantly decreased at all light intensities compared to ST/ST retinas (**Fig. 24B**).

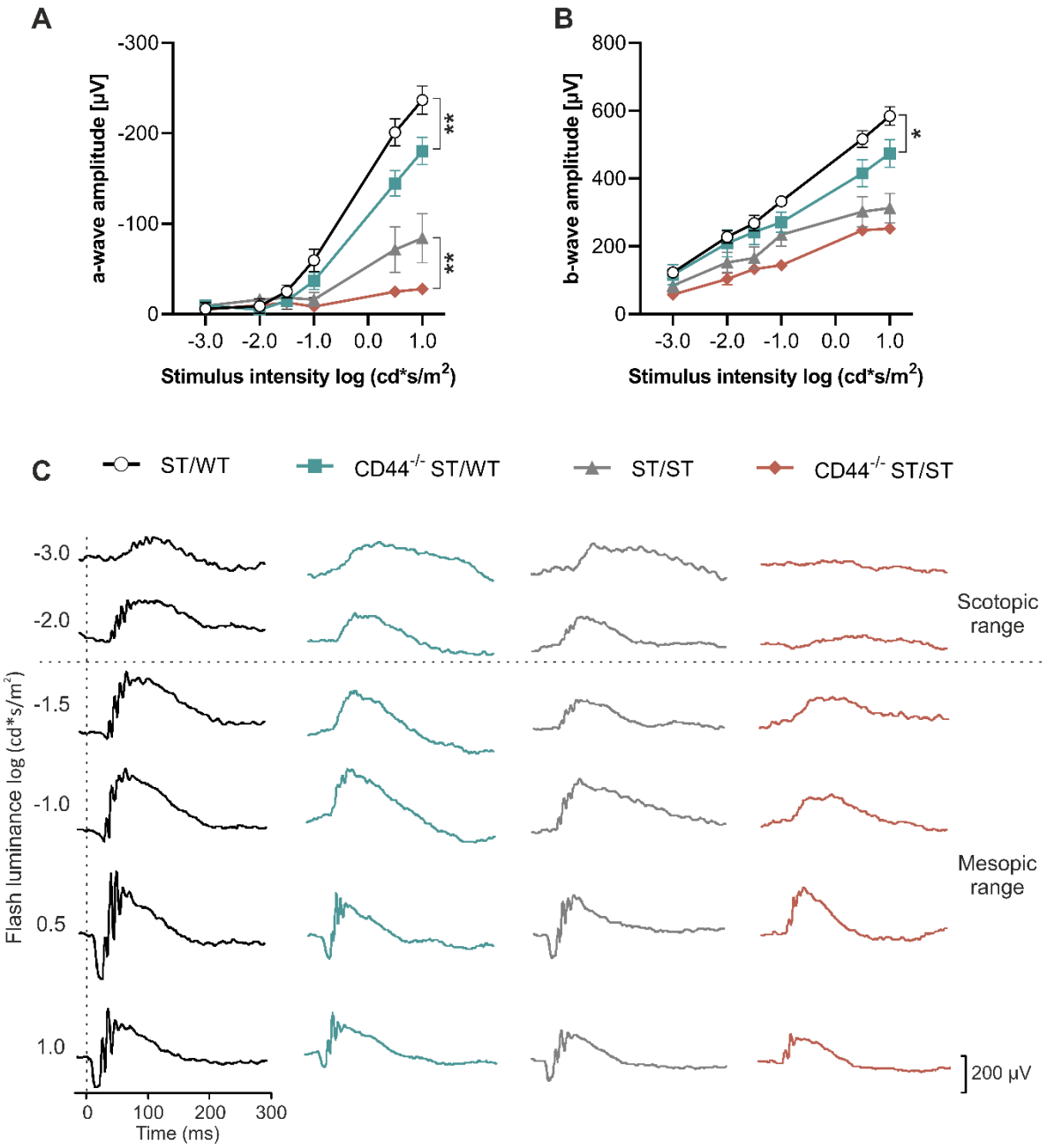

Fig. 24: Decreased scotopic and mesopic retinal function after CD44 ablation.

(A-C) ERGs were recorded of 8-week-old ST/WT, CD44$^{-/-}$ ST/WT, ST/ST, and CD44$^{-/-}$ ST/ST mice. **(A)** Scotopic and mesopic a-wave amplitudes. A-wave amplitudes of CD44$^{-/-}$ ST/WT and CD44$^{-/-}$ ST/ST at 0.5 and 1.0 log (cd*s/m^2) were significantly smaller than the a-wave amplitudes of ST/WT and ST/ST, respectively. Data, presented as mean ± SEM. N = 7 per group. ANOVA, *** P < .001. **(B)** Scotopic and mesopic b-wave amplitudes. At the highest measured light intensity 1.0 log (cd*s/m^2) the b-wave amplitude of CD44$^{-/-}$ ST/WT mice was significantly decreased compared to ST/WT mice. No statistically significant difference was observed between ST/ST, and CD44$^{-/-}$ ST/ST animals. Data presented as mean ± SEM. N = 7 per group. ANOVA, *** P < .001. **(C)** Representative ERG responses from a single retina per mouse group in the scotopic and mesopic range.

After the mice were light-adapted with a rod-desensitizing background, the cone photoreceptor response was measured. Under photopic conditions, the ERG recordings of 8-week-old ST/WT, CD44$^{-/-}$ ST/WT, ST/ST, and CD44$^{-/-}$ ST/ST mice showed an increase of the b-wave amplitude with each increased intensity (**Fig. 25A,B**). These data demonstrate that the cone-driven photopic ERG response was preserved in every mouse group of this age. Therefore, it can be concluded that ablation of CD44 in 8-week-old retinas had no effect on cone function, although the outer segments of cones were shorter than those of the respective comparison group (**4.2.2**).

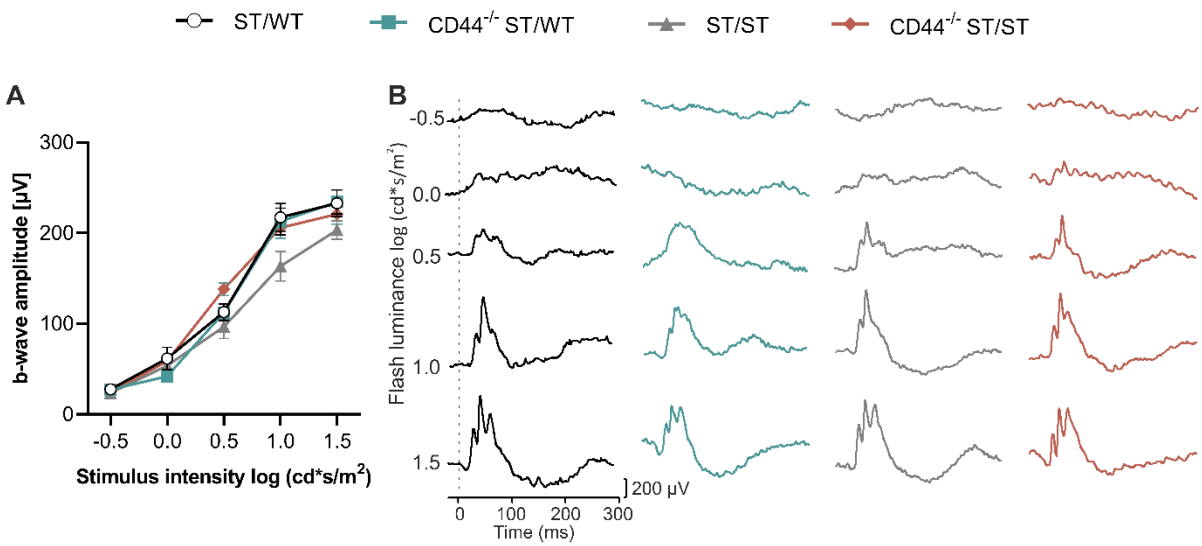

Fig. 25: Preserved photopic ERG response after CD44 ablation.
(A-B) ERGs were recorded of 8-week-old ST/WT, CD44$^{-/-}$ ST/WT, ST/ST, and CD44$^{-/-}$ ST/ST mice. **(A)** Photopic b-wave amplitudes. B-wave amplitudes were undistinguishable between all experimental groups. Data presented as mean ± SEM. N = 7 per group. **(B)** Representative ERG responses from a single retina per mouse group in the photopic range.

4.3 Investigation of CD44's ligand hyaluronic acid

Given that CD44 serves as the transmembrane receptor for hyaluronic acid (HA), we were interested in investigating whether the elevated CD44 levels observed in *Pde6b*$^{STOP/STOP}$ (ST/ST) mice were also associated with an increase in HA concentration. In addition, we aimed to determine if there were any alterations in HA expression following CD44 ablation. For this purpose, we used an HA ELISA assay to quantitatively measure total HA content per retina.

The HA analysis revealed that HA was upregulated in the ST/ST group at 4 and 8 weeks of age compared with ST/WT mice. At 4-weeks-of-age, HA concentration was 16 ng/ml and 89 ng/ml in ST/WT and ST/ST mice, respectively. In addition, HA levels were increased in CD44$^{-/-}$ ST/WT compared with ST/WT

retinas. At 8 weeks of age, HA concentration was 16 ng/ml in ST/WT and 95 ng/ml in CD44$^{-/-}$ ST/WT ($p < 0.025$, ANOVA). There were no differences between CD44$^{-/-}$ ST/ST and ST/ST animals (**Fig. 26**).

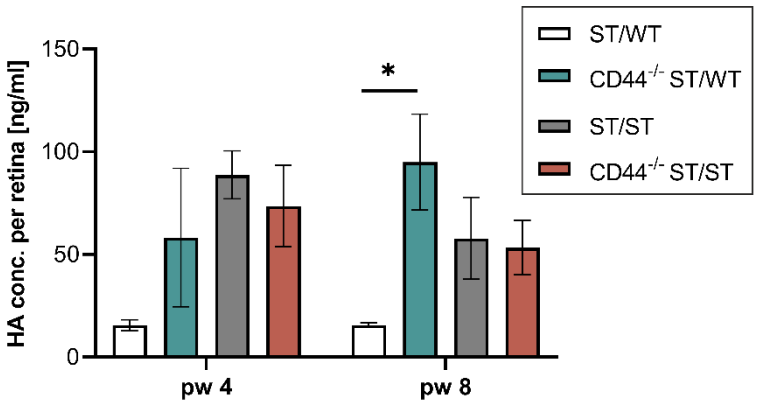

Fig. 26: Hyaluronic acid levels are elevated in ST/ST and CD44$^{-/-}$ ST/WT mice.
Quantitative ELISA assay of total retinal hyaluronic acid in 4 and 8-week-old mice. Significantly higher hyaluronic acid concentration in 8-week-old CD44$^{-/-}$ ST/WT mice compared to ST/WT mice. pw4, n = 3 for ST/WT, CD44$^{-/-}$ ST/WT, and ST/ST, n = 5 for CD44$^{-/-}$ ST/ST. pw8, n = 5 for ST/WT, CD44$^{-/-}$ ST/WT, and CD44$^{-/-}$ ST/ST, n = 6 for ST/ST. Data, presented as mean ± SEM. ANOVA, *** P < .001.

4.4 Isolation of retinal neurons and Müller cells to detect cell type specific changes

4.4.1 Isolation of neurons and Müller cells from *Pde6b$^{STOP/STOP}$* and *Cd44$^{-/-}$ Pde6b$^{STOP/STOP}$* retinas by magnetic-activated cell sorting

The characterization of the *Cd44$^{-/-}$ Pde6b$^{STOP/WT}$* and *Cd44$^{-/-}$ Pde6b$^{STOP/STOP}$* mouse lines has shown that a Müller cell-specific protein can have a significant effect on the morphology and function of both healthy and diseased retinas. Since Müller glia make up only a small fraction of cells in murine retina [107], proteomic studies of whole retina cannot provide Müller cell-specific information. Therefore, to identify proteins dysregulated in Müller cells, we performed proteomic analysis on Müller cells and neurons isolated from 8-week-old *Pde6b$^{STOP/WT}$* (ST/WT), *Pde6b$^{STOP/STOP}$* (ST/ST), CD44$^{-/-}$ ST/WT, and CD44$^{-/-}$ ST/ST retinas using a multistep magnetic-activated cell sorting (MACS).

MACS is based on sequential cell depletion and results in four different fractions: Microglia (CD11b positive population), endothelial cells (CD31+), Müller cells (CD29+), and neuron enriched flowthrough (negative for CD11b, CD31, CD29). This method enables the isolation of intact Müller cells from adult murine retina, which are also suited for subsequent proteomic analyses [95]. To ensure the purity of the Müller cell fraction compared to the neuronal fraction, samples of the freshly isolated Müller cell and neuron fractions were immunostained for Müller cell and photoreceptor specific antibodies, respectively. The CD29 positive fractions were stained with GLUL, a Müller cell marker (**Fig. 27A**), and the CD29 negative neuron samples were stained with Recoverin, a photoreceptor marker (**Fig. 27B**).

The immunohistochemistry analysis of all the MACS samples demonstrated the high purity of the individual fractions and the good performance of the method itself, because almost all of the cells were double positive for Hoechst and the cell type specific antibody GLUL or Recoverin. Importantly, isolated Müller cells retained their characteristic polar morphology (**Fig. 27A**).

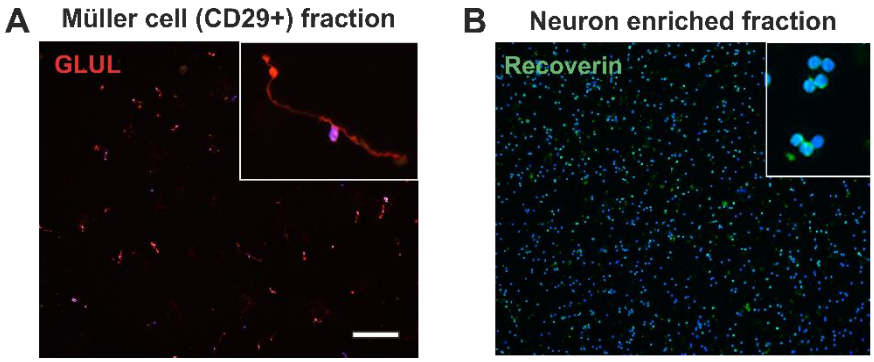

Fig. 27: Purity of magnetic-activated cell sorted (MACS) Müller cell and neuron fractions.
(A-B) Sequential MACS enrichment of *Pde6b*$^{STOP/WT}$ (ST/WT), *Pde6b*$^{STOP/STOP}$ (ST/ST), CD44$^{-/-}$ ST/WT, and CD44$^{-/-}$ ST/ST retinas yielded Müller cell (CD29+) and neuron enriched cell fractions. Representative image from an 8-week-old ST/WT animal. **(A)** CD29+ drop sample was stained with an antibody against glutamine synthetase (GLUL) and counterstained with Hoechst 33342. It consisted almost exclusively of GLUL positive cells with distinct Müller cell morphology. Scale bar, 50 µm. **(B)** Neuron enriched flowthrough was stained with Recoverin and counterstained with Hoechst 33342. Almost every cell from the drop sample is double-positive for Recoverin and Hoechst 33342 and thus consists mainly of photoreceptor neurons.

4.4.2 Proteomic profiling of Müller cells and neurons isolated from *Pde6b*$^{STOP/STOP}$ and *Cd44*$^{-/-}$ *Pde6b*$^{STOP/STOP}$ retinas

After confirming the purity of the fractions, the proteome of Müller cells and neurons of 8-week-old *Pde6b*$^{STOP/WT}$ (ST/WT), *Pde6b*$^{STOP/STOP}$ (ST/ST), CD44$^{-/-}$ ST/WT, and CD44$^{-/-}$ ST/ST retinas were analyzed by tandem mass spectrometry. This method generated a proteomic data set with approximately 5200 identified proteins per Müller cell and neuron dataset. First, the expression patterns for known marker genes were analyzed to verify the quality of the proteomic data as well as the cell fractions (**Fig. 28**). The Müller cell marker GLUL was highly expressed in the Müller cells of ST/WT, ST/ST, CD44$^{-/-}$ ST/WT, and CD44$^{-/-}$ ST/ST mice, whereas GLUL was scarcely expressed in all neuronal fractions (**Fig. 28A**). The expression pattern of rhodopsion (RHO), a rod photoreceptor marker, confirmed the purity of the neuronal fraction (**Fig. 28B**). Rho was hardly expressed in any Müller cell sample, whereas it was strongly expressed in the neuron fractions of ST/WT and CD44$^{-/-}$ ST/WT mice. The Rho expression level in the neuron fraction from ST/ST and CD44$^{-/-}$ ST/ST groups was slightly decreased compared to ST/WT and CD44$^{-/-}$ ST/WT due to the degeneration of photoreceptors in these two RP retinas (**Fig. 18**).

After the quality of the Müller cell and neuron fractions was ensured, I next examined the expression of PDE6B and CD44 (**Fig. 28C,D**). PDE6B, a rod photoreceptor marker, was hardly found in any Müller cell sample and was also absent in the neuron fractions of ST/ST and CD44$^{-/-}$ ST/ST mice. The absence of PDE6B in the Müller cell fraction provided confirmation that the separation between Müller cells and neurons was successful (**Fig. 28C**). CD44 was not found in any of the four neuronal fractions, nor in the Müller cell fractions of the CD44$^{-/-}$ mouse lines. It was expressed solely in the Müller cells of the ST/WT and ST/ST animals (**Fig. 28D**). This expression pattern confirmed the genotypes of the used mice, since CD44 expression was increased in the ST/ST compared to the ST/WT retinas (**Fig. 13**).

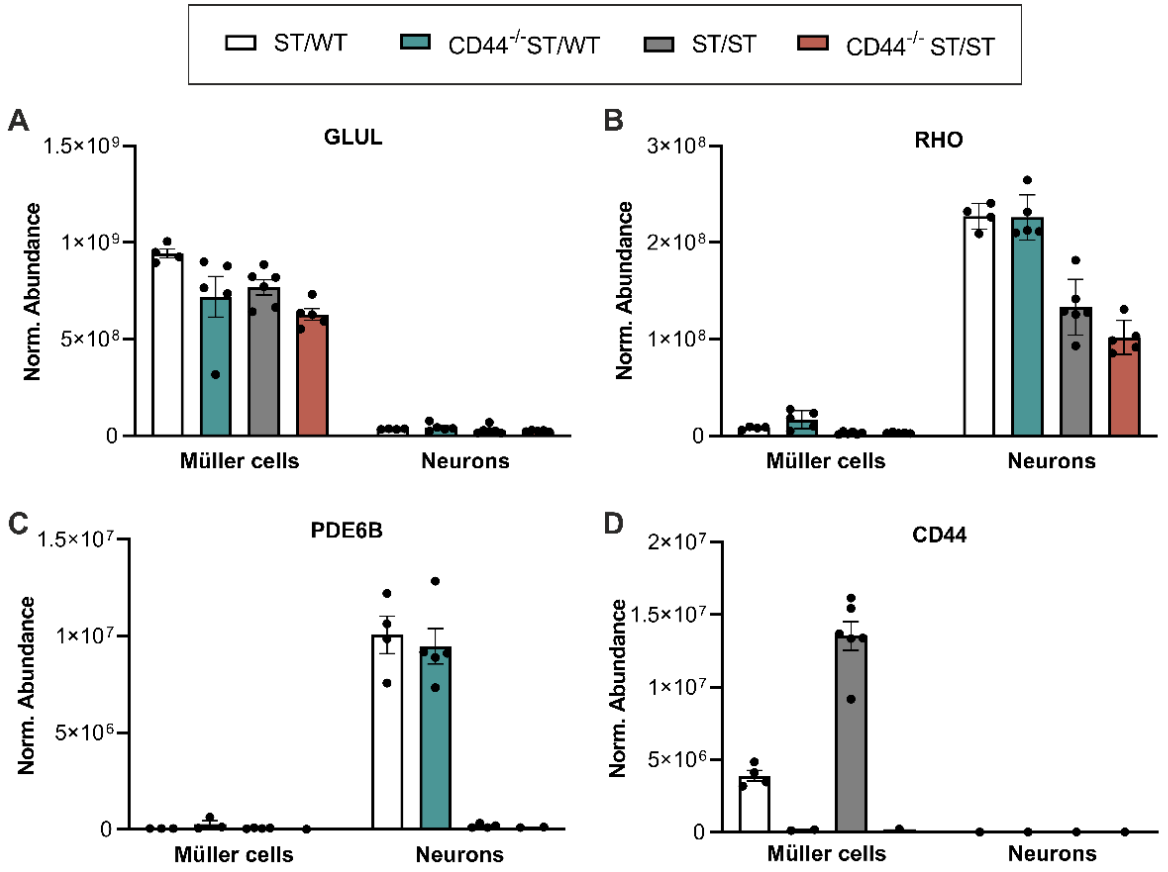

Fig. 28: Label-free mass spectrometry of Müller cell and photoreceptor specific proteins confirmed cellular subpopulations.
(A-D) Label-free mass spectrometric analysis of 8-week-old *Pde6b*$^{STOP/WT}$ (ST/WT), *Pde6b*$^{STOP/STOP}$ (ST/ST), CD44$^{-/-}$ ST/WT, and CD44$^{-/-}$ ST/ST retinas. Proteomics showed that the Müller cell marker glutamine synthetase (GLUL) was highly expressed in the CD29+ retinal Müller cells **(A)**, while rhodopsin (RHO), which is exclusively expressed in rod photoreceptors, was enriched in the triple-negative flowthrough, indicating that neurons were the most abundant cell type in this fraction **(B)**. The lower expression of RHO in ST/ST and CD44$^{-/-}$ ST/ST compared to ST/WT and CD44$^{-/-}$ ST/WT indicates the ongoing degeneration of rod photoreceptors in the RP groups. **(C)** PDE6B was exclusively found in the neuron fractions of ST/WT and CD44$^{-/-}$ ST/WT retinas. **(D)** CD44 was absent in all the CD44$^{-/-}$ groups and it wasn't detected in any of the neuronal samples as well. Furthermore, CD44 expression was increased in the ST/ST compared to the ST/WT retinas. **(A-D)** ST/WT n = 4, CD44$^{-/-}$ ST/WT, CD44$^{-/-}$ ST/ST n = 5, ST/ST n = 6.

We then used the proteomic dataset to find proteins that were differentially regulated in both CD44$^{-/-}$ ST/WT and CD44$^{-/-}$ ST/ST mice compared to ST/WT and ST/ST groups, respectively. As a first step, volcano plots of the neuron and Müller cell datasets were performed (**Fig. 29A,B**) to show proteins that are significantly differentially expressed (adj. p-value < 0.5) between ST/ST and CD44$^{-/-}$ ST/ST retinas. We also visualized Müller cell-specific proteins involved in metabolic processes in the form of a heat map (**Fig. 29C**). Solute carrier family 1 member 2 (SLC1A2) was significantly downregulated in Müller cells of CD44$^{-/-}$ ST/WT and CD44$^{-/-}$ ST/ST retinas compared to ST/WT and ST/ST retinas, respectively. These differences are visualized by both volcano plots (**Fig. 29B**) and heat map (**Fig. 29C**).

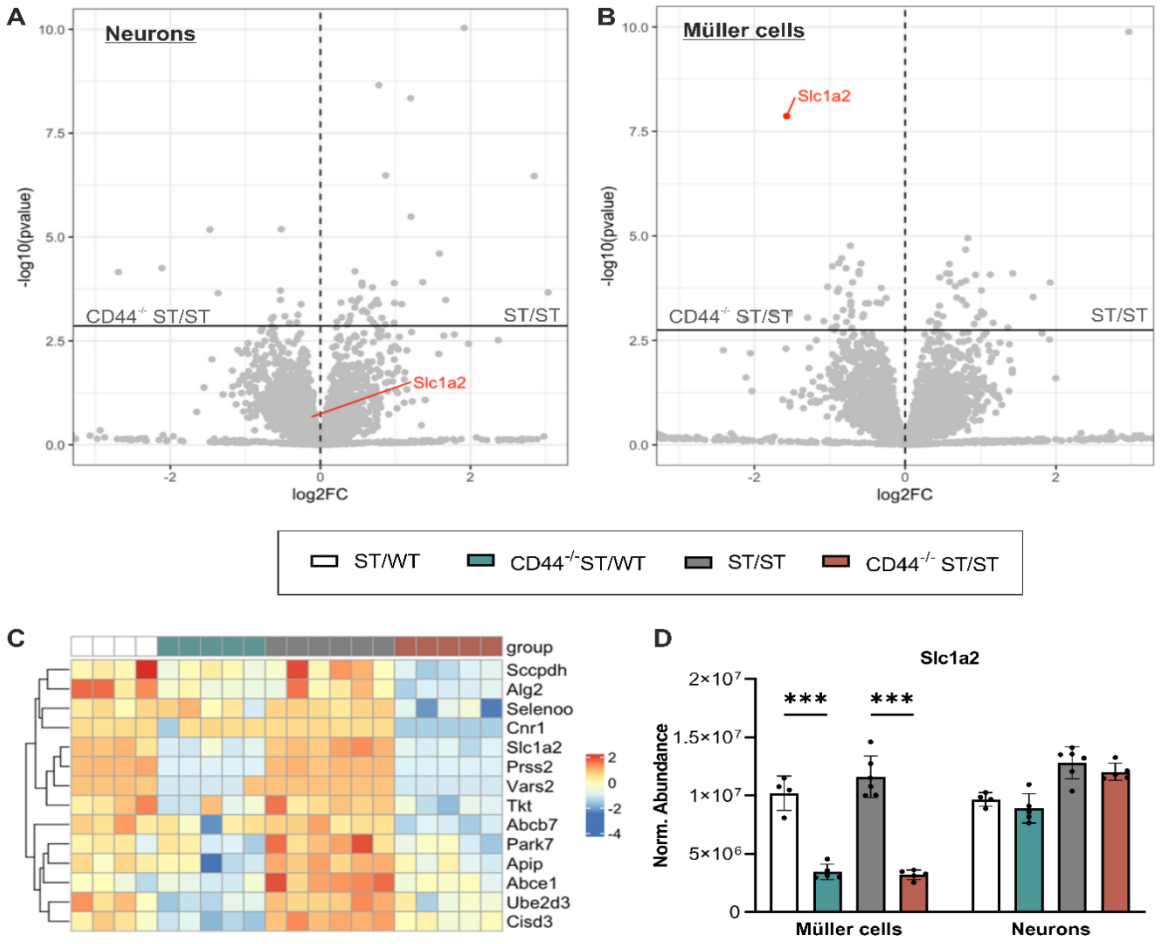

Fig. 29: Proteomic profiling of murine neurons and Müller cells of ST/WT, ST/ST, CD44$^{-/-}$ ST/WT, and CD44$^{-/-}$ ST/ST retinas.
(A) Volcano plot of differentially expressed neuronal proteins of ST/ST and CD44$^{-/-}$ ST/ST mice. SLC1A2 expression was not altered between ST/ST and CD44$^{-/-}$ ST/ST retinas. **(B)** Volcano plot of differentially expressed Müller cell proteins of ST/ST and CD44$^{-/-}$ ST/ST. Solute carrier family 1 member 2 (SLC1A2) was more than two-fold higher expressed in ST/ST compared to CD44$^{-/-}$ ST/ST retinas. **(C)** Heat map representation of Müller cell specific proteins involved in metabolic processes. Most of the proteins were strongly downregulated in the CD44$^{-/-}$ ST/ST group compared to the ST/ST group. Among them is the protein SLC1A2, also known as glutamate transporter GLT-1, an interesting candidate gene. **(D)** SLC1A2 was significantly downregulated in Müller cells of CD44$^{-/-}$ ST/WT and CD44$^{-/-}$ ST/ST compared to ST/WT and ST/ST, respectively. This downregulation didn't occur in neurons. Data presented as mean ± SEM. ANOVA, *** P < .001. **(A-D)** ST/WT n = 4, CD44$^{-/-}$ ST/WT, CD44$^{-/-}$ ST/ST n = 5, ST/ST n = 6.

The heatmap illustrates the downregulation of SLC1A2 in Müller cells of the CD44$^{-/-}$ ST/WT and CD44$^{-/-}$ ST/ST retinas compared to ST/WT and ST/ST retinas, respectively. Additionally, proteins related to metabolic processes, as identified by the gene ontology (GO) term, displayed similar expression patterns within the CD44$^{-/-}$ mouse groups and within *Pde6b*^{STOP} retinas. All proteins shown were downregulated in the CD44$^{-/-}$ mice compared with ST/WT and ST/ST mice (**Fig. 29C**). SLC1A2, also known as glutamate transporter GLT-1, is an interesting candidate protein, because it was significantly downregulated in the Müller cell fractions of CD44$^{-/-}$ ST/WT and CD44$^{-/-}$ ST/ST retinas compared to

ST/WT and ST/ST retinas, respectively ($p < 0,001$, ANOVA), whereas it was not altered in the neuron fraction between these groups (**Fig. 29D**).

4.5 Validation of decreased SLC1A2 expression in *Cd44*$^{-/-}$ *Pde6b*$^{STOP/WT}$ *and Cd44*$^{-/-}$ *Pde6b*$^{STOP/STOP}$ retinas

Our proteomics data revealed low expression of SLC1A2 protein in Müller cells of CD44$^{-/-}$ ST/WT and CD44$^{-/-}$ ST/ST retinas (**Fig. 29**). SLC1A2 encodes EAAT2, also known as the glial glutamate transporter GLT1 in the mouse [120]. Müller cells, as the principal glial cells of the retina, express this glutamate transporter and are able to take up extracellular glutamate and by that support the synaptic activity [60]. To verify the results of the proteome analysis, immunohistochemistry and immunoblots were performed (**Fig. 30**). Staining of SLC1A2 in retinal sections of 8-week-old mice revealed that the glutamate transporter is expressed by Müller cells and cone photoreceptors (**Fig. 30A**). In addition, immunohistochemistry also showed that the expression of SLC1A2 was reduced in CD44$^{-/-}$ ST/WT and CD44$^{-/-}$ ST/ST retinas compared to ST/WT and ST/ST, respectively. To further validate this observation, immunoblots for SLC1A2 were performed. The representative immunoblot confirmed the downregulated glutamate transporter in 8-week-old CD44$^{-/-}$ ST/WT and CD44$^{-/-}$ ST/ST retinas compared with ST/WT and ST/ST, respectively (**Fig. 30B**). Quantitative evaluation of immunoblots confirmed the decreased expression of the glutamate transporter SLC1A2, which was reduced by an average of 60 % in the CD44$^{-/-}$ ST/ST mice compared to the ST/ST group. In the CD44$^{-/-}$ ST/WT retinas, SLC1A2 expression decreased by an average of 50 % compared to ST/WT mice (**Fig. 30C**).

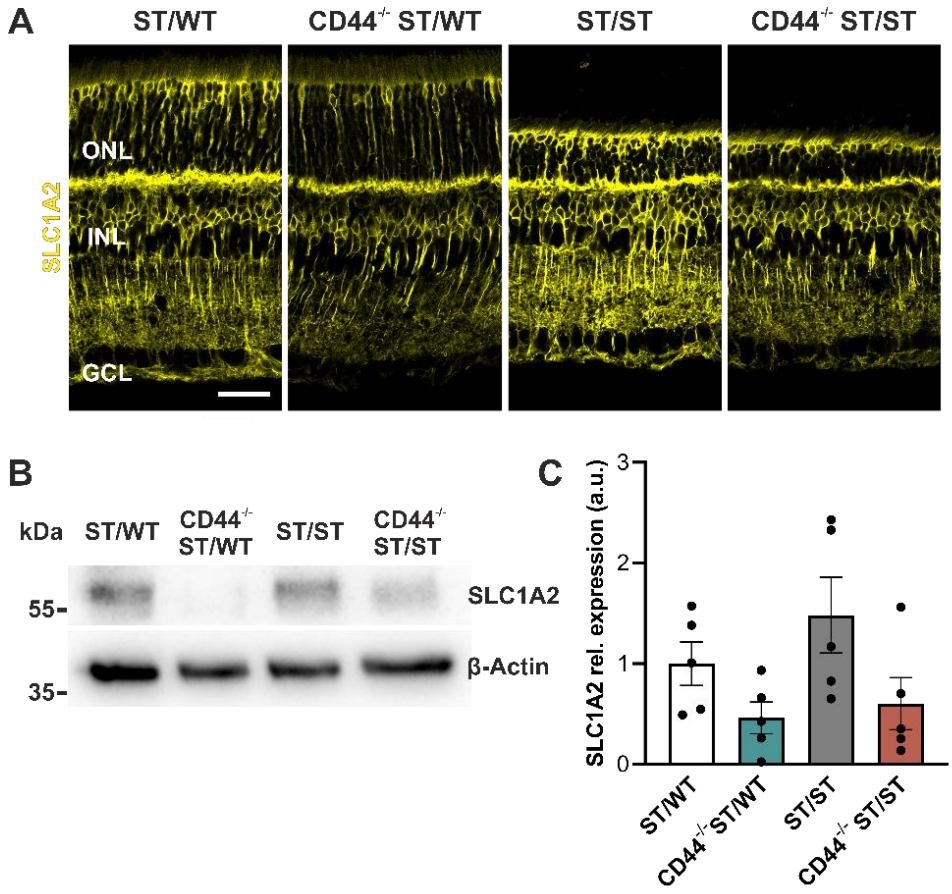

Fig. 30: Validation of decreased SLC1A2 expression in CD44$^{-/-}$ ST/WT and CD44$^{-/-}$ ST/ST retinas.
(A-C) Retinas from ST/WT, CD44$^{-/-}$ ST/WT, ST/ST, and CD44$^{-/-}$ ST/ST were analyzed at 8 weeks of age. **(A)** Representative images of retinal sections immunostained for the glutamate transporter SLC1A2 to visualize its expression pattern. SLC1A2 is expressed by Müller cells and cone photoreceptors and was downregulated in CD44$^{-/-}$ ST/WT and CD44$^{-/-}$ ST/ST mice. Scale bar, 35 µm. **(B)** Representative SLC1A2 immunoblot of whole retinal lysates. SLC1A2 was downregulated in CD44$^{-/-}$ ST/WT and CD44$^{-/-}$ ST/ST retinas. β-Actin was used as a loading control. **(C)** Quantitative analysis of SLC1A2 immunoblots. Decreased SLC1A2 expression in 8-week-old CD44$^{-/-}$ ST/WT and CD44$^{-/-}$ ST/ST compared to ST/WT and ST/ST mice, respectively. Data presented as mean ± SEM. ANOVA, *** P < .001. N = 5 per group.

4.6 Impact of SLC1A2 downregulation in *Cd44$^{-/-}$ Pde6b$^{STOP/WT}$* and *Cd44$^{-/-}$ Pde6b$^{STOP/STOP}$* retinas on glutamate levels in the retina

To determine whether the observed downregulation of the glutamate transporter impacts retinal glutamate levels, a fluorometric glutamate assay was established (chapter 3.2.14). With this method, we were able to calculate the amount of glutamate per retina (in nmol/mg protein). We hypothesize that the downregulation of the glutamate transporter SLC1A2 in Müller cells results in a higher glutamate concentration in the retina, as Glutamate is not sufficiently removed from the extracellular space. In fact, the assay revealed significantly increased glutamate levels of 260 nmol/mg in CD44$^{-/-}$

ST/WT retinas compared to 169 nmol/mg in ST/WT retinas ($P < 0.05$, ANOVA). Glutamate concentration in CD44$^{-/-}$ ST/ST retinas was also increased to 217 nmol/mg compared to 148 nmol/mg in ST/ST retinas, but this difference was not significant (**Fig. 31**).

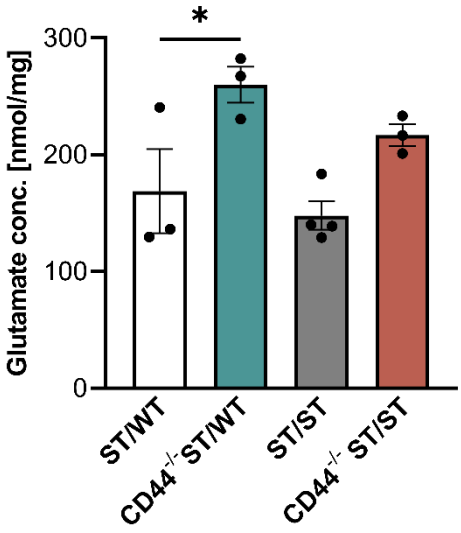

Fig. 31: Increased glutamate levels in *Cd44*$^{-/-}$ retinas.
Fluorometric glutamate assay of 8-week-old *Pde6b*$^{STOP/WT}$ (ST/WT), *Pde6b*$^{STOP/STOP}$ (ST/ST), CD44$^{-/-}$ ST/WT, and CD44$^{-/-}$ ST/ST retinas. Significant higher glutamate concentration in CD44$^{-/-}$ ST/WT retinas compared to ST/WT. CD44$^{-/-}$ ST/ST retinas had increased glutamate levels compared to ST/ST. Data, presented as mean ± SEM. ANOVA, *** $P < .001$. ST/WT, CD44$^{-/-}$ ST/WT, CD44$^{-/-}$ ST/ST n = 3, ST/ST n = 4.

4.7 Loss of CD44 leads to impaired metabolism in photoreceptors

To investigate whether the loss of CD44 in Müller cells affects aerobic glycolysis in photoreceptors, which serves as the primary source of energy in these cells, the expression of the enzyme pyruvate kinase M2 (PKM2) was investigated. PKM2 is a crucial regulator of aerobic glycolysis and catalyzes the final rate-limiting step of glycolysis, namely the conversion of phosphoenolpyruvate (PEP) to pyruvate [12, 121]. The immunohistochemistry of PKM2 (**Fig. 32A**) showed that the enzyme is mainly expressed in the inner segments of photoreceptors. Furthermore, the staining revealed, that PKM2 was upregulated in CD44$^{-/-}$ ST/WT and CD44$^{-/-}$ ST/ST mice compared to ST/WT and ST/ST mice, respectively. Immunoblots were performed to quantify this observation (**Fig. 32B,C**). The representative immunoblot in Fig. **32B** shows the elevated PKM2 expression in CD44$^{-/-}$ ST/WT and CD44$^{-/-}$ ST/ST compared to ST/WT and ST/ST, respectively. Quantification of immunoblots revealed that the expression of PKM2 increased in CD44$^{-/-}$ ST/WT and CD44$^{-/-}$ ST/ST retinas compared to ST/WT and ST/ST retinas, respectively. However, the increase was not statistically significant (ANOVA) (**Fig. 32C**).

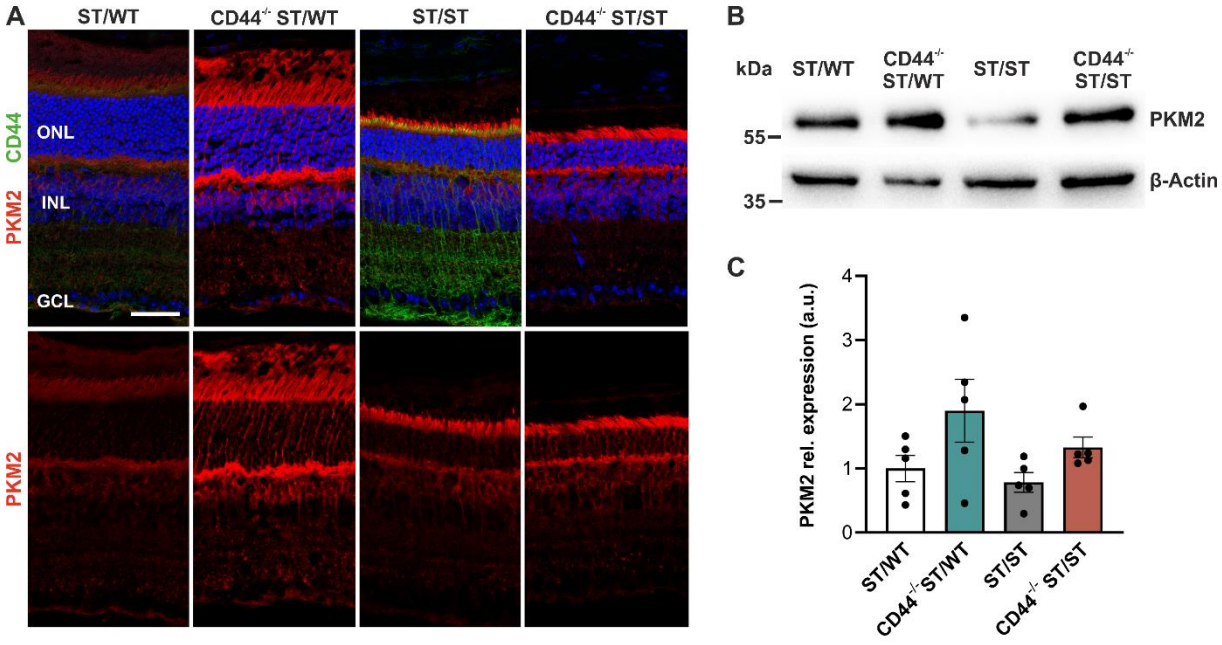

Fig. 32: Upregulated PKM2 expression in CD44$^{-/-}$ ST/WT and CD44$^{-/-}$ ST/ST retinas.
(A-C) Retinas from ST/WT, CD44$^{-/-}$ ST/WT, ST/ST, and CD44$^{-/-}$ ST/ST were analyzed at 8 weeks of age. **(A)** Representative images of retinal sections immunostained for the enzyme PKM2 and counterstained for CD44 to visualize their expression pattern. PKM2 is expressed in the inner segments of photoreceptors and to a lesser extent also in cells in the outer plexiform layer. PKM2 was upregulated in CD44$^{-/-}$ ST/WT and CD44$^{-/-}$ ST/ST mice. Scale bar, 25 µm. **(B)** Representative PKM2 immunoblot of whole retinal lysates. PKM2 was upregulated in CD44$^{-/-}$ ST/WT and CD44$^{-/-}$ ST/ST retinas. β-Actin was used as a loading control. **(C)** Quantitative analysis of PKM2 immunoblots. Increased PKM2 expression in 8-week-old CD44$^{-/-}$ ST/WT and CD44$^{-/-}$ ST/ST compared to ST/WT and ST/ST mice, respectively. Data presented as mean ± SEM. ANOVA, *** P < .001. N = 5 per group.

After pyruvate is synthesized by PKM2, it can subsequently be reduced to lactate in aerobic glycolysis or enter the tricarboxylic acid (TCA) cycle for energy production [60, 121, 122, 10]. To assess whether the increase of PKM2 in CD44$^{-/-}$ ST/WT and CD44$^{-/-}$ ST/ST mice correlate with an enhancement of aerobic glycolysis in photoreceptors, we measured the content of lactate per retina.

The lactate assay was performed in 8-week-old ST/WT, ST/ST, CD44$^{-/-}$ ST/WT, and CD44$^{-/-}$ ST/ST retinas (**Fig. 33**). The lactate concentrations of ST/ST and CD44$^{-/-}$ ST/ST retinas were significantly lower compared to ST/WT and CD44$^{-/-}$ ST/WT retinas, respectively. This indicates that in both RP mouse models, there was a significant reduction in lactate concentration compared to their respective ST/WT and CD44$^{-/-}$ ST/WT controls. Interestingly, despite the elevated PKM2 levels in CD44$^{-/-}$ ST/WT and CD44$^{-/-}$ ST/ST retinas, there was no increase in lactate concentration compared to ST/WT and ST/ST retinas, respectively. These findings provide evidence that the increased glycolytic rate resulting from elevated PKM2 levels in CD44$^{-/-}$ ST/WT and CD44$^{-/-}$ ST/ST retinas is primarily utilized for energy production through the TCA cycle, rather than for an increased production of lactate.

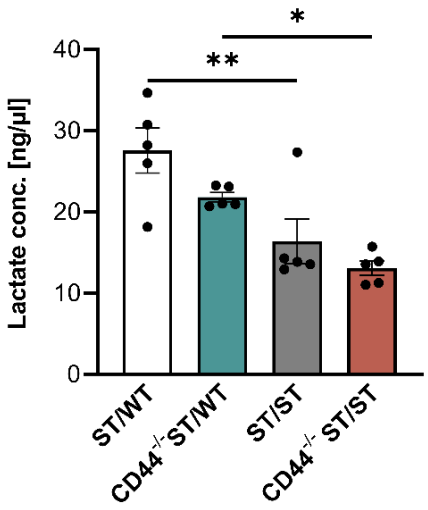

Fig. 33: Decreased lactate concentration in *Cd44*$^{-/-}$ retinas.
Lactate assay of 8-week-old *Pde6b*$^{STOP/WT}$ (ST/WT), *Pde6b*$^{STOP/STOP}$ (ST/ST), CD44$^{-/-}$ ST/WT, and CD44$^{-/-}$ ST/ST retinas. Significant lower lactate concentration in ST/ST, and CD44$^{-/-}$ ST/ST retinas compared to ST/WT or CD44$^{-/-}$ ST/WT, respectively. Data, presented as mean ± SEM. ANOVA, *** P < .001. n = 5 per group.

5 Discussion

Many different mutations in a variety of genes but also yet unknown gene mutations can lead to retinitis pigmentosa (RP). Given the large heterogeneity of genetic lesions and the fact that a causative mutation cannot always be identified [123], it is important to study gene-independent mechanisms that accompany disease progression and photoreceptor degeneration. In this context, special attention should be given to Müller cells, as they are among the first cells to respond to retinal stress, a process termed gliosis. Little is known about the downstream effects of Müller cell gliosis, to the point that the field continues to debate whether the effects on retinal neurons are detrimental, beneficial, or both [50]. A feature of Müller cells in murine RP retinas is the upregulation of the protein CD44 [78, 79]. However, the role of CD44 on disease progression has not yet been deciphered.

In this study, the *Pde6b*^{Stop} RP mouse model was used to investigate the effects of CD44 expression on photoreceptor disease progression.

5.1 Gene independent upregulation of CD44 expression in RP retinas

This study demonstrated the upregulation of the Müller cell specific protein CD44 in two PDE6B-deficient RP mouse lines, an RHO-deficient RP mouse line and the *Cnga3*$^{-/-}$, *Rho*$^{-/-}$, *Opn4*$^{-/-}$ triple-knockout mice (**Fig. 13,14**). These results suggest that Müller cells respond similarly to photoreceptor degeneration in RP, at least in terms of CD44 expression. The question now arose whether CD44 functions as a marker for Müller cell gliosis, similar to GFAP [67], or whether its expression has a positive or negative impact on disease progression. To address these questions, *Cd44*$^{-/-}$ mice were analyzed and in a next step crossed with our *Pde6b*$^{Stop/Stop}$ (ST/ST) RP mouse model to suppress CD44 overexpression in those mice.

5.2 Loss of CD44 signaling in healthy and diseased retinas leads to decreased retinal function

To investigate the role of CD44 in the retina, *Cd44*$^{-/-}$ mice were used. 60-week-old *Cd44*$^{-/-}$ and *Cd44*$^{+/+}$ mice had comparable GFAP levels (**Fig. 15**), demonstrating that loss of CD44 expression does not lead to Müller cell gliosis. Furthermore, immunohistochemistry analysis of GLUL revealed intact Müller cell morphology (**Fig. 15**).

To determine whether the ablation of CD44 already affects retinal morphology ST/WT, ST/ST, CD44$^{-/-}$ ST/WT, and CD44$^{-/-}$ ST/ST retinas were examined at 3, 4, 8, and 12 weeks of age. Studies have shown

that CD44 is expressed in Müller cell progenitors [90, 124, 125] and thus may have effects on retinal development. The analysis of our 3-week-old mice revealed that CD44$^{-/-}$ ST/WT and CD44$^{-/-}$ ST/ST retinas had the same ONL layer thickness and cone inner and outer segment length as ST/WT animals at 3 weeks of age (**Fig. 18**), demonstrating, that CD44 does not impact photoreceptor development.

Additionally, the morphological characterization of ST/WT, ST/ST, CD44$^{-/-}$ ST/WT, and CD44$^{-/-}$ ST/ST mice showed that CD44$^{-/-}$ ST/ST retinas have a more rapid degeneration of rod photoreceptors compared with ST/ST retinas which was significant in 12-week-old mice, and shorter cone inner and outer segments after the onset of disease at 4 weeks of age (**Fig. 18**). The ONL of CD44$^{-/-}$ ST/WT retinas was thinner compared to ST/WT retinas from as early as 4 weeks of age.

In parallel with the enhanced degeneration of rods and shorter cone outer segments, CD44$^{-/-}$ ST/WT and CD44$^{-/-}$ ST/ST retinas exhibited retinal remodeling of inner retinal neurons, including rod and cone bipolar cells and horizontal cells. In the case of rod bipolar cells, loss of CD44 even resulted in significant loss of dendritic area in ST/WT mice (**Fig. 19-21**). It is also worth noting that despite the more rapid degeneration of photoreceptors and inner retinal remodeling in CD44$^{-/-}$ ST/ST mice, Müller cell gliosis did not increase compared to ST/ST retinas, as shown by analysis of the gliosis marker GFAP (**Fig. 17**). However, this contrasts with the increased inflammatory response, as both the number of activated microglia and the expression of proinflammatory factors such as TNFα, NFκb, and IL-6 were increased in CD44$^{-/-}$ ST/ST compared with ST/ST retinas at 8 weeks of age (**Fig. 22-23**). Activated microglia infiltrate the ONL in 12-week-old CD44$^{-/-}$ ST/ST retinas. Infiltrated microglia phagocytose degenerating PRs and secrete proinflammatory cytokines, including TNFα. Activation of microglia, originally triggered by the mutation underlying RP, persists during the disease and exacerbates PR loss into the late stages [110].

To characterize the function, ERG measurements were performed in 8-week-old ST/WT, ST/ST, CD44$^{-/-}$ ST/WT, and CD44$^{-/-}$ ST/ST mice (**Fig. 24**). These data revealed that the rod-driven a-wave is significantly reduced in CD44$^{-/-}$ ST/WT, and CD44$^{-/-}$ ST/ST mice compared to ST/WT and ST/ST mice, respectively. The significant loss of rod function proved that the loss of CD44 had detrimental effects on ST/WT and ST/ST retinas. The measurements of the mesopic range, where rods, cones, as well as rod and cone bipolar cells are responsive, showed that the responses of the CD44$^{-/-}$ ST/WT and CD44$^{-/-}$ ST/ST mice were lower than those of ST/WT and ST/ST mice (**Fig. 24**). This result could be influenced by the remodeling of rod bipolar cells in CD44$^{-/-}$ ST/WT and CD44$^{-/-}$ ST/ST mice (**Fig. 19**). The photopic b-wave responses, were not significantly altered in CD44$^{-/-}$ ST/WT and CD44$^{-/-}$ ST/ST compared with ST/WT and ST/ST retinas, respectively (**Fig. 25**). This could be due to the fact that the reduction of the dendritic area in cone bipolar cells in 12-week-old mice was less than in rod bipolar cells (**Fig. 19,20**). This

reduction of dendritic area was probably even less pronounced at the time of ERG measurement at 8 weeks of age.

The first part of our study, focusing on the morphology and function of the retina, has demonstrated that the loss of CD44 has significant consequences on both healthy and diseased retinas. Although in the healthy retina the expression of CD44 in Müller cells is quite weak, it seems to have an impact on retinal integrity and health, as both morphologic changes and impaired rod function are observed in CD44$^{-/-}$ ST/WT compared with ST/WT mice. With respect to RP retinas, in which CD44 expression is elevated during disease progression, loss of this Müller cell-specific protein increases photoreceptor degeneration compared with ST/ST retinas, as there are also greater morphologic changes as well as greater loss of retinal function in CD44$^{-/-}$ ST/ST compared with ST/ST mice. These changes are also associated with an increased proinflammatory response in CD44$^{-/-}$ ST/ST mice.

5.3 Loss of the hyaluronic acid receptor CD44 and alterations in the composition of the extracellular matrix may impair retinal integrity and Müller cell function

Since CD44 is the receptor for hyaluronic acid (HA) [126], the HA concentrations in ST/WT, ST/ST, CD44$^{-/-}$ ST/WT, and CD44$^{-/-}$ ST/ST retinas were also investigated. The results showed that HA concentration was significantly higher in CD44$^{-/-}$ ST/WT retinas than in ST/WT mice, and HA concentration was also higher in ST/ST and CD44$^{-/-}$ ST/ST retinas than in ST/WT (**Fig. 26**). The extracellular matrix (ECM), which is largely composed of HA, has structural but also functional roles [126, 127]. The ECM's composition is subject to variation in order to suit the requirements of adjacent retinal cells, enabling cell mobility and responsiveness while preserving tissue integrity [128]. The increase in the HA concentration in ST/ST mice indicates that the ECM responds to photoreceptor death. This restructuring of the ECM composition during degeneration could subsequently lead to the upregulation of CD44, the transmembrane receptor for HA. This upregulation of HA expression presumably enhances connectivity between the ECM and the cytoskeleton of Müller cells. In CD44$^{-/-}$ ST/WT and CD44$^{-/-}$ ST/ST retinas, where the receptor for HA is absent, the connection between the ECM and Müller cells is probably compromised, because HA is a major component of the ECM. In an effort to counteract this, CD44$^{-/-}$ ST/WT mice may exhibit a significant increase in HA expression compared to ST/WT mice. However, this compensatory response was not observed in CD44$^{-/-}$ ST/ST mice, as those retinas exhibited the same HA levels as ST/ST retinas. It is possible that this compensatory mechanism is no longer effective in CD44$^{-/-}$ ST/ST mice due to the more advanced degeneration present in those retinas.

It has been discussed that alterations in the interphotoreceptor matrix (IPM), the ECM between the OLM and the RPE, affect retinal health, since this is the medium where metabolites are exchanged [14, 11]. This could explain the (enhanced) photoreceptor degeneration in CD44$^{-/-}$ ST/WT and CD44$^{-/-}$ ST/ST retinas, as the loss of the HA receptor CD44, could impair the three-dimensional HA network in the subretinal space [89], and thereby disrupting the metabolite transport from the choroid to the photoreceptors and Müller cells.

5.4 Loss of CD44 affects glutamate homeostasis within the retina

To investigate cell type-specific alterations and understand the impact of a Müller cell-specific protein on photoreceptor survival, we conducted proteomic analysis on isolated Müller cells and neurons derived from 8-week-old retinas of ST/WT, ST/ST, CD44$^{-/-}$ ST/WT, and CD44$^{-/-}$ ST/ST mice. Following the validation of our methodology (**Fig. 27,28**), we discovered a significant downregulation of the glutamate transporter SLC1A2 (also known as EAAT2) in Müller cells of CD44$^{-/-}$ ST/WT and CD44$^{-/-}$ ST/ST retinas compared to ST/WT and ST/ST retinas, respectively (**Fig. 29**). This finding could be validated by immunofluorescence and immunoblot analysis (**Fig. 30**). Since Müller cells are responsible for glutamate clearance from the synaptic cleft in the inner retina, thereby protecting neurons from excitotoxicity [60, 62], this downregulation of SLC1A2 in Müller cells could potentially affect overall retinal glutamate homeostasis. To verify this assumption, a glutamate assay was performed to measure the glutamate concentrations in the retina. Strikingly, glutamate levels were higher in 8-week-old CD44$^{-/-}$ ST/WT, and CD44$^{-/-}$ ST/ST compared with ST/WT and ST/ST retinas (**Fig 31**). Although this assay did not discriminate between intracellular and extracellular glutamate, it could still be suggested that the glutamate concentration in the synaptic cleft is possibly responsible for the overall higher glutamate concentrations in CD44$^{-/-}$ ST/WT, and CD44$^{-/-}$ ST/ST retinas, since it is generally assumed that Müller cells themselves contain little glutamate, because they convert it to glutamine and α-ketoglutarate immediately after uptake [62]. It is important to mention that glutamate is only excitotoxic if glial glutamate reuptake is impaired. This highlights the importance of the glutamate transporter of Müller cells in order to prevent neurotoxic effects [129–131]. Considering that our proteomic data revealed a downregulation of the SLC1A2 glutamate transporter in Müller cells of CD44$^{-/-}$ ST/WT, and CD44$^{-/-}$ ST/ST retinas, and that we observed higher glutamate levels in these retinas, it can be concluded that this might lead to excitotoxic effects in the retina.

Studies suggested that increased numbers of activated microglia which secrete proinflammatory cytokines such as TNFα may also increase synaptic glutamate levels [132, 133] while downregulating the expression and functionality of glutamate transporters such as EAAT2 [132]. The fact that we have

significantly more activated microglia in 12-week-old CD44$^{-/-}$ ST/ST retinas compared with ST/ST retinas (**Fig. 22**) could also impact the higher glutamate concentrations in those mice and thus explain the enhanced disease progression in CD44$^{-/-}$ ST/ST mice. But if the higher number of activated microglia would really lead to a downregulation of the SLC1A2 glutamate transporter, we would not see this downregulation in CD44$^{-/-}$ ST/WT, because the number of activated microglia in CD44$^{-/-}$ ST/WT retinas does not differ from that of ST/WT mice. To summarize, as the downregulated SLC1A2 expression was confirmed in both CD44$^{-/-}$ mouse lines, the number of microglia cannot be responsible for the altered SLC1A2 expression (**Fig. 30**), but microglia might further drive the excitotoxic damage in CD44$^{-/-}$ ST/ST mice by contributing to higher glutamate levels. In contrast to CD44$^{-/-}$ ST/ST mice, we observed resting, ramified microglia in CD44$^{-/-}$ ST/WT retinas. These are suspected to have neuroprotective functions by minimizing excitotoxic-induced neurodegeneration [134, 135]. Taking into account that CD44$^{-/-}$ ST/WT mice also showed retinal degeneration, remodeling and impaired retinal function, it indicates that the effects of elevated glutamate levels exceed the neuroprotective capacities of ramified microglia.

It was surprising that the SLC1A2 transporter had such a large effect on glutamate levels in the retina, because according to the literature the glutamate aspartate transporter 1 (GLAST1) appears to be the major and most abundant glutamate transporter in Müller cells [129, 136, 137]. In fact, the currently available literature suggests that SLC1A2 is not expressed in Müller cells, but in cones, bipolar cells, and amacrine cells [137–139]. However, our MAC-sorted proteomics and immunohistochemistry data clearly demonstrate that SLC1A2 is expressed in Müller cells (and cones). The increased glutamate levels indicate its significant role in glutamate homeostasis.

Reduced glutamate uptake may also lead to a compromised supply of nutrients to the photoreceptors, since Müller cells convert the uptaken glutamate directly into glutamine and α-ketoglutarate (KG), which are then transported to the photoreceptors to serve as a source of energy [60].

5.5 Alterations of the metabolic landscape after CD44 ablation

Photoreceptors are the cells in the body that consume the most oxygen and rely on aerobic glycolysis to meet their anabolic needs [12]. However, they also derive energy from the TCA cycle [60]. For this purpose, they use KG, which is produced and released by Müller cells, and serves as a key metabolite in the TCA cycle [140, 141]. To investigate whether downregulation of the glutamate transporter SLC1A2 in Müller cells of CD44$^{-/-}$ retinas leads to impaired energy supply for the photoreceptors, pyruvate kinase M2 (PKM2) expression was investigated. PKM2 is the key enzyme in glycolysis, as it catalyzes the final step of glycolysis, namely the conversion of phosphoenolpyruvate (PEP) to pyruvate, in the inner segments of photoreceptors [12, 142]. After pyruvate is synthesized by PKM2, it can

subsequently be reduced to lactate in aerobic glycolysis or enter the TCA cycle for energy production. The same cycle where KG is used [60, 121, 122, 10]. By examining the expression of PKM2, we get insights if there are alterations in metabolism following CD44 ablation.

Our results showed that PKM2 was upregulated in both CD44$^{-/-}$ ST/WT and CD44$^{-/-}$ ST/ST compared with ST/WT and ST/ST retinas, respectively (**Fig. 32**). PKM2 can occur in two different forms, the dimeric PKM2 provides enhanced formation of glycolytic intermediates for OS renewal via the pentose phosphate pathway and suppresses OXPHOS, thus preventing high ATP generation. The highly active, tetrameric PKM2, on the other hand, ensures increased ATP formation by introducing the formed pyruvate into the TCA cycle [12, 142]. Although we did not distinguish between the two forms of PKM2 in our experiments, the observed increase in PKM2 expression suggests that the photoreceptors of both CD44$^{-/-}$ ST/WT and CD44$^{-/-}$ ST/ST mouse groups metabolically reprogram themselves to meet their metabolic needs.

Next, we examined the lactate levels in the retinas. Lactate is the end product of aerobic glycolysis and serves as a source of energy within the retina. Lactate is transported to the RPE and Müller cells where it is used in the mitochondria for energy production, i.e. ATP synthesis. This prevents the RPE from consuming glucose, allowing it to deliver glucose to the photoreceptors [14, 60, 143]. Our results showed that there are significant lower lactate levels in ST/ST and CD44$^{-/-}$ ST/ST retinas compared with ST/WT and CD44$^{-/-}$ ST/WT retinas, respectively (**Fig. 33**). These data also indicate a decrease in lactate concentration from ST/WT to CD44$^{-/-}$ ST/WT retinas, and a slight decrease between ST/ST and CD44$^{-/-}$ ST/ST retinas, but neither difference was significant. This result revealed that the increase in PKM2 in CD44$^{-/-}$ ST/WT and CD44$^{-/-}$ ST/ST retinas did not lead to increased lactate levels and thus did not enhance aerobic glycolytic rate. The decreased lactate levels in ST/ST and CD44$^{-/-}$ ST/ST mice (compared to ST/WT and CD44$^{-/-}$ ST/WT, respectively) can be explained by the overall loss of lactate-producing cells, mainly photoreceptors, and the increased lactate consumption rate of dying photoreceptors [143].

In summary, we have shown that loss of CD44 leads to increased PKM2 expression, a critical catalyst for the final step of glycolysis [122]. However, this increase did not lead to an increase in aerobic glycolysis because lactate levels were not increased in CD44$^{-/-}$ ST/WT and CD44$^{-/-}$ ST/ST retinas. This suggests that the retinas either express more dimeric PKM2 to force the formation of glycolytic intermediates in the pentose phosphate pathway or that it is present in the tetrameric state, whereby the formed pyruvate is used for energy production in the TCA cycle and OXPHOS to compensate for losses due to the potential loss of α-ketoglutarate. To test this hypothesis, it would be necessary to perform metabolome analysis to determine the exact concentrations of lactate, pyruvate, and KG within the retinas of ST/WT, ST/ST, CD44$^{-/-}$ ST/WT and CD44$^{-/-}$ ST/ST mice.

It is striking that fusion transcripts of CD44 and SLC1A2 have been found in some types of cancer [144, 145]. The fusion occurred between exon 1 of the CD44 gene and exon 2 of the SLC1A2 gene, resulting in transcription of functional SLC1A2 under CD44 as the promoter [145]. Considering that retinal cells behave like cancer cells in many respects, especially in terms of metabolism [146], this could possibly be the reason why CD44 ablation in Müller cells leads to SLC1A2 downregulation since CD44 is missing as its promoter.

In summary, endogenous CD44 signaling in the retina appears to be necessary to prevent glutamate excitotoxicity, to provide adequate nutrient supply to photoreceptors, and, as a receptor for the major component of the IPM hyaluronic acid [89], to provide attachment sites for the IPM, potentially supporting retinal integrity and nutrient supply from the choroid.

6 References

1. Enoch J, McDonald L, Jones L et al. (2019) Evaluating Whether Sight Is the Most Valued Sense. JAMA Ophthalmol 137:1317–1320. https://doi.org/10.1001/jamaophthalmol.2019.3537
2. Poché RA, Reese BE (2009) Retinal horizontal cells: challenging paradigms of neural development and cancer biology. Development 136:2141–2151. https://doi.org/10.1242/dev.033175
3. Mahabadi N, Al Khalili Y (2023) StatPearls: Neuroanatomy, Retina, Treasure Island (FL)
4. Masland RH (2012) The neuronal organization of the retina. Neuron 76:266–280. https://doi.org/10.1016/j.neuron.2012.10.002
5. Schnapf JL, Baylor DA (1987) How photoreceptor cells respond to light. Sci Am 256:40–47. https://doi.org/10.1038/scientificamerican0487-40
6. Hoon M, Okawa H, Della Santina L et al. (2014) Functional architecture of the retina: development and disease. Prog Retin Eye Res 42:44–84. https://doi.org/10.1016/j.preteyeres.2014.06.003
7. Vecino E, Rodriguez FD, Ruzafa N et al. (2016) Glia-neuron interactions in the mammalian retina. Prog Retin Eye Res 51:1–40. https://doi.org/10.1016/j.preteyeres.2015.06.003
8. Silverman SM, Wong WT (2018) Microglia in the Retina: Roles in Development, Maturity, and Disease. Annu Rev Vis Sci 4:45–77. https://doi.org/10.1146/annurev-vision-091517-034425
9. Liu H, Prokosch V (2021) Energy Metabolism in the Inner Retina in Health and Glaucoma. Int J Mol Sci 22. https://doi.org/10.3390/ijms22073689
10. Viegas FO, Neuhauss SCF (2021) A Metabolic Landscape for Maintaining Retina Integrity and Function. Front Mol Neurosci 14:656000. https://doi.org/10.3389/fnmol.2021.656000
11. Ishikawa M, Sawada Y, Yoshitomi T (2015) Structure and function of the interphotoreceptor matrix surrounding retinal photoreceptor cells. Exp Eye Res 133:3–18. https://doi.org/10.1016/j.exer.2015.02.017
12. Rajala RVS (2020) Aerobic Glycolysis in the Retina: Functional Roles of Pyruvate Kinase Isoforms. Front Cell Dev Biol 8. https://doi.org/10.3389/fcell.2020.00266
13. Hurley JB (2021) Retina Metabolism and Metabolism in the Pigmented Epithelium: A Busy Intersection. Annu Rev Vis Sci 7:665–692. https://doi.org/10.1146/annurev-vision-100419-115156
14. Hurley JB, Lindsay KJ, Du J (2015) Glucose, lactate, and shuttling of metabolites in vertebrate retinas. J Neurosci Res 93:1079–1092. https://doi.org/10.1002/jnr.23583
15. Kanow MA, Giarmarco MM, Jankowski C, SR et al. (2017) Biochemical adaptations of the retina and retinal pigment epithelium support a metabolic ecosystem in the vertebrate eye. Elife 6. https://doi.org/10.7554/eLife.28899

16. Wang W, Kini A, Wang Y et al. (2019) Metabolic Deregulation of the Blood-Outer Retinal Barrier in Retinitis Pigmentosa. Cell Rep 28:1323-1334.e4. https://doi.org/10.1016/j.celrep.2019.06.093
17. Chen Y, Coorey NJ, Zhang M et al. (2022) Metabolism Dysregulation in Retinal Diseases and Related Therapies. Antioxidants (Basel) 11. https://doi.org/10.3390/antiox11050942
18. Shichida Y, Matsuyama T (2009) Evolution of opsins and phototransduction. Philos Trans R Soc Lond B Biol Sci 364:2881–2895. https://doi.org/10.1098/rstb.2009.0051
19. Burns ME, Arshavsky VY (2005) Beyond counting photons: trials and trends in vertebrate visual transduction. Neuron 48:387–401. https://doi.org/10.1016/j.neuron.2005.10.014
20. Ryan SJ, Wilkinson CP (2006 (i.e. 2005)) Retina, 4th ed. Elsevier/Mosby, Philadelphia
21. Amara SG (2006) Reviews of Physiology, Biochemistry and Pharmacology. Reviews of Physiology, Biochemistry and Pharmacology Ser. Springer, New York
22. Soucy E, Wang Y, Nirenberg S et al. (1998) A novel signaling pathway from rod photoreceptors to ganglion cells in mammalian retina. Neuron 21:481–493. https://doi.org/10.1016/s0896-6273(00)80560-7
23. Mannu GS (2014) Retinal phototransduction. Neurosciences (Riyadh) 19:275–280
24. Lamb TD (2022) Photoreceptor physiology and evolution: cellular and molecular basis of rod and cone phototransduction. J Physiol 600:4585–4601. https://doi.org/10.1113/JP282058
25. Lamb TD, Heck M, Kraft TW (2018) Implications of dimeric activation of PDE6 for rod phototransduction. Open Biol 8. https://doi.org/10.1098/rsob.180076
26. Cote RH (2004) Characteristics of photoreceptor PDE (PDE6): similarities and differences to PDE5. Int J Impot Res 16 Suppl 1:S28-33. https://doi.org/10.1038/sj.ijir.3901212
27. Verbakel SK, van Huet RAC, Boon CJF et al. (2018) Non-syndromic retinitis pigmentosa. Prog Retin Eye Res 66:157–186. https://doi.org/10.1016/j.preteyeres.2018.03.005
28. Francis PJ (2006) Genetics of inherited retinal disease. J R Soc Med 99:189–191. https://doi.org/10.1177/014107680609900417
29. Newton F, Megaw R (2020) Mechanisms of Photoreceptor Death in Retinitis Pigmentosa. Genes (Basel) 11. https://doi.org/10.3390/genes11101120
30. Wright AF, Chakarova CF, Abd El-Aziz MM et al. (2010) Photoreceptor degeneration: genetic and mechanistic dissection of a complex trait. Nat Rev Genet 11:273–284. https://doi.org/10.1038/nrg2717
31. Ferrari S, Di Iorio E, Barbaro V et al. (2011) Retinitis pigmentosa: genes and disease mechanisms. Curr Genomics 12:238–249. https://doi.org/10.2174/138920211795860107
32. Menghini M, Cehajic-Kapetanovic J, MacLaren RE (2020) Monitoring progression of retinitis pigmentosa: current recommendations and recent advances. Expert Opin Orphan Drugs 8:67–78. https://doi.org/10.1080/21678707.2020.1735352

33. Campochiaro PA, Mir TA (2018) The mechanism of cone cell death in Retinitis Pigmentosa. Prog Retin Eye Res 62:24–37. https://doi.org/10.1016/j.preteyeres.2017.08.004
34. Krol J, Roska B (2015) Rods Feed Cones to Keep them Alive. Cell 161:706–708. https://doi.org/10.1016/j.cell.2015.04.031
35. Kuehlewein L, Zobor D, Stingl K et al. (2021) Clinical Phenotype of PDE6B-Associated Retinitis Pigmentosa. Int J Mol Sci 22. https://doi.org/10.3390/ijms22052374
36. Li Y, Li R, Dai H et al. (2022) Novel variants in PDE6A and PDE6B genes and its phenotypes in patients with retinitis pigmentosa in Chinese families. BMC Ophthalmol 22:27. https://doi.org/10.1186/s12886-021-02242-5
37. Hartong DT, Berson EL, Dryja TP (2006) Retinitis pigmentosa. Lancet 368:1795–1809. https://doi.org/10.1016/s0140-6736(06)69740-7
38. Hamel C (2006) Retinitis pigmentosa. Orphanet J Rare Dis 1:40. https://doi.org/10.1186/1750-1172-1-40
39. Gao Z, Zhu Q, Zhang Y et al. (2013) Reciprocal modulation between microglia and astrocyte in reactive gliosis following the CNS injury. Mol Neurobiol 48:690–701. https://doi.org/10.1007/s12035-013-8460-4
40. Marc RE, Jones BW (2003) Retinal remodeling in inherited photoreceptor degenerations. Mol Neurobiol 28:139–147. https://doi.org/10.1385/MN:28:2:139
41. Lewis GP, Chapin EA, Luna G et al. (2010) The fate of Müller's glia following experimental retinal detachment: nuclear migration, cell division, and subretinal glial scar formation. Mol Vis 16:1361–1372
42. Fisher SK, Lewis GP (2003) Müller cell and neuronal remodeling in retinal detachment and reattachment and their potential consequences for visual recovery: a review and reconsideration of recent data. Vision Res 43:887–897. https://doi.org/10.1016/S0042-6989(02)00680-6
43. Telias M, Nawy S, Kramer RH (2020) Degeneration-Dependent Retinal Remodeling: Looking for the Molecular Trigger. Front Neurosci 14:618019. https://doi.org/10.3389/fnins.2020.618019
44. Jones BW, Pfeiffer RL, Ferrell WD et al. (2016) Retinal remodeling in human retinitis pigmentosa. Exp Eye Res 150:149–165. https://doi.org/10.1016/j.exer.2016.03.018
45. Jones BW, Kondo M, Terasaki H et al. (2012) Retinal remodeling. Jpn J Ophthalmol 56:289–306. https://doi.org/10.1007/s10384-012-0147-2
46. Marc RE, Jones BW, Watt CB et al. (2003) Neural remodeling in retinal degeneration. Prog Retin Eye Res 22:607–655. https://doi.org/10.1016/s1350-9462(03)00039-9
47. Reichenbach A, Bringmann A (2013) New functions of Müller cells. Glia 61:651–678. https://doi.org/10.1002/glia.22477

48. Goldman D (2014) Müller glia cell reprogramming and retina regeneration. Nat Rev Neurosci 15:431–442. https://doi.org/10.1038/nrn3723
49. Kobat SG, Turgut B (2020) Importance of Müller Cells. Beyoglu Eye J 5:59–63. https://doi.org/10.14744/bej.2020.28290
50. Bringmann A, Pannicke T, Grosche J et al. (2006) Müller cells in the healthy and diseased retina. Prog Retin Eye Res 25:397–424. https://doi.org/10.1016/j.preteyeres.2006.05.003
51. Wang M, Wong WT (2014) Microglia-Müller cell interactions in the retina. Adv Exp Med Biol 801:333–338. https://doi.org/10.1007/978-1-4614-3209-8_42
52. Bejarano-Escobar R, Sánchez-Calderón H, Otero-Arenas J et al. (2017) Müller glia and phagocytosis of cell debris in retinal tissue. J Anat 231:471–483. https://doi.org/10.1111/joa.12653
53. Franze K, Grosche J, Skatchkov SN et al. (2007) Muller cells are living optical fibers in the vertebrate retina. Proc Natl Acad Sci U S A 104:8287–8292. https://doi.org/10.1073/pnas.0611180104
54. Reichenbach A, Bringmann A (2020) Glia of the human retina. Glia 68:768–796. https://doi.org/10.1002/glia.23727
55. Tworig JM, Feller MB (2021) Müller Glia in Retinal Development: From Specification to Circuit Integration. Front Neural Circuits 15:815923. https://doi.org/10.3389/fncir.2021.815923
56. Rich KA, Figueroa SL, Zhan Y et al. (1995) Effects of Müller cell disruption on mouse photoreceptor cell development. Exp Eye Res 61:235–248. https://doi.org/10.1016/S0014-4835(05)80043-0
57. Newman EA (1987) Regulation of potassium levels by Müller cells in the vertebrate retina. Can J Physiol Pharmacol 65:1028–1032. https://doi.org/10.1139/y87-162
58. Boal AM, McGrady NR, Risner ML et al. (2022) Sensitivity to extracellular potassium underlies type-intrinsic differences in retinal ganglion cell excitability. Front Cell Neurosci 16:966425. https://doi.org/10.3389/fncel.2022.966425
59. Li X, Lv J, Li J et al. (2021) Kir4.1 may represent a novel therapeutic target for diabetic retinopathy (Review). Exp Ther Med 22:1021. https://doi.org/10.3892/etm.2021.10453
60. Bringmann A, Grosche A, Pannicke T et al. (2013) GABA and Glutamate Uptake and Metabolism in Retinal Glial (Müller) Cells. Front Endocrinol (Lausanne) 4:48. https://doi.org/10.3389/fendo.2013.00048
61. Toft-Kehler AK, Skytt DM, Kolko M (2018) A Perspective on the Müller Cell-Neuron Metabolic Partnership in the Inner Retina. Mol Neurobiol 55:5353–5361. https://doi.org/10.1007/s12035-017-0760-7

62. Pfeiffer RL, Marc RE, Jones BW (2020) Müller Cell Metabolic Signatures: Evolutionary Conservation and Disruption in Disease. Trends Endocrinol Metab 31:320–329. https://doi.org/10.1016/j.tem.2020.01.005
63. Wang M, Wong WT (2014) Microglia-Müller Cell Interactions in the Retina. Adv Exp Med Biol 801:333–338. https://doi.org/10.1007/978-1-4614-3209-8_42
64. (2001) Role of Müller cells in retinal degenerations
65. Graca AB, Hippert C, Pearson RA (2018) Müller Glia Reactivity and Development of Gliosis in Response to Pathological Conditions. Adv Exp Med Biol 1074:303–308. https://doi.org/10.1007/978-3-319-75402-4_37
66. Iandiev I, Biedermann B, Bringmann A et al. (2006) Atypical gliosis in Müller cells of the slowly degenerating rds mutant mouse retina. Exp Eye Res 82:449–457. https://doi.org/10.1016/j.exer.2005.07.018
67. Bringmann A, Iandiev I, Pannicke T et al. (2009) Cellular signaling and factors involved in Müller cell gliosis: neuroprotective and detrimental effects. Prog Retin Eye Res 28:423–451. https://doi.org/10.1016/j.preteyeres.2009.07.001
68. Liu Y, Li L, Pan N et al. (2021) TNF-α released from retinal Müller cells aggravates retinal pigment epithelium cell apoptosis by upregulating mitophagy during diabetic retinopathy. Biochem Biophys Res Commun 561:143–150. https://doi.org/10.1016/j.bbrc.2021.05.027
69. Eastlake K, Banerjee PJ, Angbohang A et al. (2015) Müller glia as an important source of cytokines and inflammatory factors present in the gliotic retina during proliferative vitreoretinopathy. Glia 64:495–506. https://doi.org/10.1002/glia.22942
70. Palazzo I, Todd LJ, Hoang TV et al. (2022) NFkB-signaling promotes glial reactivity and suppresses Müller glia-mediated neuron regeneration in the mammalian retina. Glia 70:1380–1401. https://doi.org/10.1002/glia.24181
71. Reichenbach A, Wurm A, Pannicke T et al. (2007) Müller cells as players in retinal degeneration and edema. Graefes Arch Clin Exp Ophthalmol 245:627–636. https://doi.org/10.1007/s00417-006-0516-y
72. Hu X, Zhao G-L, Xu M-X et al. (2021) Interplay between Müller cells and microglia aggravates retinal inflammatory response in experimental glaucoma. J Neuroinflammation 18:303. https://doi.org/10.1186/s12974-021-02366-x
73. Fernández-Sánchez L, Lax P, Campello L et al. (2015) Astrocytes and Müller Cell Alterations During Retinal Degeneration in a Transgenic Rat Model of Retinitis Pigmentosa. Front Cell Neurosci 9:484. https://doi.org/10.3389/fncel.2015.00484

74. Roche SL, Ruiz-Lopez AM, Moloney JN et al. (2018) Microglial-induced Müller cell gliosis is attenuated by progesterone in a mouse model of retinitis pigmentosa. Glia 66:295–310. https://doi.org/10.1002/glia.23243
75. Díaz-Lezama N, Kajtna J, Wu J et al. (2023) Microglial and macroglial dynamics in a model of retinitis pigmentosa. Vision Res 210:108268. https://doi.org/10.1016/j.visres.2023.108268
76. Sherpa T, Fimbel SM, Mallory DE et al. (2008) Ganglion cell regeneration following whole-retina destruction in zebrafish. Dev Neurobiol 68:166–181. https://doi.org/10.1002/dneu.20568
77. Lindsey AE, Powers MK (2007) Visual behavior of adult goldfish with regenerating retina. Vis Neurosci 24:247–255. https://doi.org/10.1017/S0952523806230207
78. Chaitin MH, Ankrum MT, Wortham HS (1996) Distribution of CD44 in the retina during development and the rds degeneration. Brain Res Dev Brain Res 94:92–98. https://doi.org/10.1016/0165-3806(96)00046-6
79. Krishnamoorthy R, Agarwal N, Chaitin MH (2000) Upregulation of CD44 expression in the retina during the rds degeneration. Brain Res Mol Brain Res 77:125–130. https://doi.org/10.1016/s0169-328x(00)00035-8
80. Borland G, Ross JA, Guy K (1998) Forms and functions of CD44. Immunology 93:139–148. https://doi.org/10.1046/j.1365-2567.1998.00431.x
81. Sneath RJ, Mangham DC (1998) The normal structure and function of CD44 and its role in neoplasia. Mol Pathol 51:191–200. https://doi.org/10.1136/mp.51.4.191
82. Chen C, Zhao S, Karnad A et al. (2018) The biology and role of CD44 in cancer progression: therapeutic implications. J Hematol Oncol 11:64. https://doi.org/10.1186/s13045-018-0605-5
83. Ponta H, Sherman L, Herrlich PA (2003) CD44: from adhesion molecules to signalling regulators. Nat Rev Mol Cell Biol 4:33–45. https://doi.org/10.1038/nrm1004
84. Hassn Mesrati M, Syafruddin SE, Mohtar MA et al. (2021) CD44: A Multifunctional Mediator of Cancer Progression. Biomolecules 11:1850. https://doi.org/10.3390/biom11121850
85. Szatanek R, Baj-Krzyworzeka M (2021) CD44 and Tumor-Derived Extracellular Vesicles (TEVs). Possible Gateway to Cancer Metastasis. Int J Mol Sci 22. https://doi.org/10.3390/ijms22031463
86. Cichy J, Puré E (2004) Cytokines regulate the affinity of soluble CD44 for hyaluronan. FEBS Lett 556:69–74. https://doi.org/10.1016/S0014-5793(03)01370-X
87. Too LK, Gracie G, Hasic E et al. (2017) Adult human retinal Müller glia display distinct peripheral and macular expression of CD117 and CD44 stem cell-associated proteins. Acta Histochem 119:142–149. https://doi.org/10.1016/j.acthis.2016.12.003
88. Chaitin MH, Wortham HS, Brun-Zinkernagel AM (1994) Immunocytochemical localization of CD44 in the mouse retina. Exp Eye Res 58:359–365. https://doi.org/10.1006/exer.1994.1026

89. Hollyfield JG, Rayborn ME, Tammi M et al. (1998) Hyaluronan in the interphotoreceptor matrix of the eye: species differences in content, distribution, ligand binding and degradation. Exp Eye Res 66:241–248. https://doi.org/10.1006/exer.1997.0422
90. Shinoe T, Kuribayashi H, Saya H et al. (2010) Identification of CD44 as a cell surface marker for Müller glia precursor cells. J Neurochem 115:1633–1642. https://doi.org/10.1111/j.1471-4159.2010.07072.x
91. Chaitin MH, Brun-Zinkernagel AM (1998) Immunolocalization of CD44 in the dystrophic rat retina. Exp Eye Res 67:283–292. https://doi.org/10.1006/exer.1998.0510
92. Davis RJ, Hsu C-W, Tsai Y-T et al. (2013) Therapeutic margins in a novel preclinical model of retinitis pigmentosa. J Neurosci 33:13475–13483. https://doi.org/10.1523/JNEUROSCI.0419-13.2013
93. Protin U, Schweighoffer T, Jochum W et al. (1999) CD44-deficient mice develop normally with changes in subpopulations and recirculation of lymphocyte subsets. J Immunol 163:4917–4923
94. Wiśniewski JR, Zougman A, Nagaraj N et al. (2009) Universal sample preparation method for proteome analysis. Nat Methods 6:359–362. https://doi.org/10.1038/nmeth.1322
95. Grosche A, Hauser A, Lepper MF et al. (2016) The Proteome of Native Adult Müller Glial Cells From Murine Retina. Mol Cell Proteomics 15:462–480. https://doi.org/10.1074/mcp.M115.052183
96. Käll L, Canterbury JD, Weston J et al. (2007) Semi-supervised learning for peptide identification from shotgun proteomics datasets. Nat Methods 4:923–925. https://doi.org/10.1038/NMETH1113
97. Navarro P, Trevisan-Herraz M, Bonzon-Kulichenko E et al. (2014) General statistical framework for quantitative proteomics by stable isotope labeling. J Proteome Res 13:1234–1247. https://doi.org/10.1021/pr4006958
98. Davis RJ, Tosi J, Janisch KM et al. (2008) Functional rescue of degenerating photoreceptors in mice homozygous for a hypomorphic cGMP phosphodiesterase 6 b allele (Pde6bH620Q). Invest Ophthalmol Vis Sci 49:5067–5076. https://doi.org/10.1167/iovs.07-1422
99. Sakami S, Maeda T, Bereta G et al. (2011) Probing mechanisms of photoreceptor degeneration in a new mouse model of the common form of autosomal dominant retinitis pigmentosa due to P23H opsin mutations. J Biol Chem 286:10551–10567. https://doi.org/10.1074/jbc.M110.209759
100. Claes E, Seeliger M, Michalakis S et al. (2004) Morphological characterization of the retina of the CNGA3(-/-)Rho(-/-) mutant mouse lacking functional cones and rods. Invest Ophthalmol Vis Sci 45:2039–2048. https://doi.org/10.1167/iovs.03-0741
101. Laprell L, Tochitsky I, Kaur K et al. (2017) Photopharmacological control of bipolar cells restores visual function in blind mice. J Clin Invest 127:2598–2611. https://doi.org/10.1172/JCI92156

102. Hippert C, Graca AB, Barber AC et al. (2015) Müller glia activation in response to inherited retinal degeneration is highly varied and disease-specific. PLoS One 10:e0120415. https://doi.org/10.1371/journal.pone.0120415
103. Germer A, Jahnke C, Mack A et al. (1997) Modification of glutamine synthetase expression by mammalian Müller (glial) cells in retinal organ cultures. Neuroreport 8:3067–3072. https://doi.org/10.1097/00001756-199709290-00012
104. Fu Y, Yau K-W (2007) Phototransduction in mouse rods and cones. Pflugers Arch 454:805–819. https://doi.org/10.1007/s00424-006-0194-y
105. Ruether K, Feigenspan A, Pirngruber J et al. (2010) PKC{alpha} is essential for the proper activation and termination of rod bipolar cell response. Invest Ophthalmol Vis Sci 51:6051–6058. https://doi.org/10.1167/iovs.09-4704
106. Puthussery T, Gayet-Primo J, Taylor WR (2010) Localization of the calcium-binding protein secretagogin in cone bipolar cells of the mammalian retina. J Comp Neurol 518:513–525. https://doi.org/10.1002/cne.22234
107. Haverkamp S, Wässle H (2000) Immunocytochemical analysis of the mouse retina. J Comp Neurol 424:1–23
108. Ortega JT, Jastrzebska B (2021) Neuroinflammation as a Therapeutic Target in Retinitis Pigmentosa and Quercetin as Its Potential Modulator. Pharmaceutics 13. https://doi.org/10.3390/pharmaceutics13111935
109. Chang B, Hawes NL, Hurd RE et al. (2002) Retinal degeneration mutants in the mouse. Vision Res 42:517–525. https://doi.org/10.1016/S0042-6989(01)00146-8
110. Zhao L, Hou C, Yan N (2022) Neuroinflammation in retinitis pigmentosa: Therapies targeting the innate immune system. Front Immunol 13:1059947. https://doi.org/10.3389/fimmu.2022.1059947
111. Noailles A, Maneu V, Campello L et al. (2016) Persistent inflammatory state after photoreceptor loss in an animal model of retinal degeneration. Sci Rep 6:33356. https://doi.org/10.1038/srep33356
112. Fan W, Huang W, Chen J et al. (2022) Retinal microglia: Functions and diseases. Immunology 166:268–286. https://doi.org/10.1111/imm.13479
113. Imai Y, Ibata I, Ito D et al. (1996) A novel gene iba1 in the major histocompatibility complex class III region encoding an EF hand protein expressed in a monocytic lineage. Biochem Biophys Res Commun 224:855–862. https://doi.org/10.1006/bbrc.1996.1112
114. Waller R, Baxter L, Fillingham DJ et al. (2019) Iba-1-/CD68+ microglia are a prominent feature of age-associated deep subcortical white matter lesions. PLoS One 14:e0210888. https://doi.org/10.1371/journal.pone.0210888

115. Liu T, Zhang L, Joo D et al. (2017) NF-κB signaling in inflammation. Signal Transduct Target Ther 2:17023-. https://doi.org/10.1038/sigtrans.2017.23
116. Benchorin G, Calton MA, Beaulieu MO et al. (2017) Assessment of Murine Retinal Function by Electroretinography. Bio Protoc 7. https://doi.org/10.21769/BioProtoc.2218
117. Pinto LH, Invergo B, Shimomura K et al. (2007) Interpretation of the mouse electroretinogram. Doc Ophthalmol 115:127–136. https://doi.org/10.1007/s10633-007-9064-y
118. Tanimoto N, Sothilingam V, Kondo M et al. (2015) Electroretinographic assessment of rod- and cone-mediated bipolar cell pathways using flicker stimuli in mice. Sci Rep 5:10731. https://doi.org/10.1038/srep10731
119. Barbur JL, Stockman A (2010) Photopic, Mesopic and Scotopic Vision and Changes in Visual Performance. In: Encyclopedia of the Eye. Elsevier, pp 323–331
120. Fiorentino A, Sharp SI, McQuillin A (2015) Association of rare variation in the glutamate receptor gene SLC1A2 with susceptibility to bipolar disorder and schizophrenia. Eur J Hum Genet 23:1200–1206. https://doi.org/10.1038/ejhg.2014.261
121. Wubben TJ, Pawar M, Smith A et al. (2017) Photoreceptor metabolic reprogramming provides survival advantage in acute stress while causing chronic degeneration. Sci Rep 7:17863. https://doi.org/10.1038/s41598-017-18098-z
122. Zhang E, Ryu J, Levi SR et al. (2020) PKM2 ablation enhanced retinal function and survival in a preclinical model of retinitis pigmentosa. Mamm Genome 31:77–85. https://doi.org/10.1007/s00335-020-09837-1
123. Wang SK, Xue Y, Rana P et al. (2019) Soluble CX3CL1 gene therapy improves cone survival and function in mouse models of retinitis pigmentosa. Proc Natl Acad Sci U S A 116:10140–10149. https://doi.org/10.1073/pnas.1901787116
124. Freude KK, Saruhanian S, McCauley A et al. (2020) Enrichment of retinal ganglion and Müller glia progenitors from retinal organoids derived from human induced pluripotent stem cells - possibilities and current limitations. World J Stem Cells 12:1171–1183. https://doi.org/10.4252/wjsc.v12.i10.1171
125. Eastlake K, Luis J, Wang W et al. (2023) Transcriptomics of CD29+/CD44+ cells isolated from hPSC retinal organoids reveals a single cell population with retinal progenitor and Müller glia characteristics. Sci Rep 13:5081. https://doi.org/10.1038/s41598-023-32058-w
126. Lesley J, Hyman R, Kincade PW (1993) CD44 and its interaction with extracellular matrix. Adv Immunol 54:271–335. https://doi.org/10.1016/s0065-2776(08)60537-4
127. Hubmacher D, Apte SS (2013) The biology of the extracellular matrix: novel insights. Curr Opin Rheumatol 25:65–70. https://doi.org/10.1097/BOR.0b013e32835b137b

128. Al-Ubaidi MR, Naash MI, Conley SM (2013) A perspective on the role of the extracellular matrix in progressive retinal degenerative disorders. Invest Ophthalmol Vis Sci 54:8119–8124. https://doi.org/10.1167/iovs.13-13536
129. Izumi Y, Shimamoto K, Benz AM et al. (2002) Glutamate transporters and retinal excitotoxicity. Glia 39:58–68. https://doi.org/10.1002/glia.10082
130. Rodríguez Villanueva J, Martín Esteban J, Rodríguez Villanueva LJ (2020) Retinal Cell Protection in Ocular Excitotoxicity Diseases. Possible Alternatives Offered by Microparticulate Drug Delivery Systems and Future Prospects. Pharmaceutics 12. https://doi.org/10.3390/pharmaceutics12020094
131. Vorwerk CK, Naskar R, Schuettauf F et al. (2000) Depression of retinal glutamate transporter function leads to elevated intravitreal glutamate levels and ganglion cell death. Invest Ophthalmol Vis Sci 41:3615–3621
132. Haroon E, Miller AH, Sanacora G (2017) Inflammation, Glutamate, and Glia: A Trio of Trouble in Mood Disorders. Neuropsychopharmacology 42:193–215. https://doi.org/10.1038/npp.2016.199
133. Fogal B, Hewett SJ (2008) Interleukin-1beta: a bridge between inflammation and excitotoxicity? J Neurochem 106:1–23. https://doi.org/10.1111/j.1471-4159.2008.05315.x
134. Howe ML, Barres BA (2012) A novel role for microglia in minimizing excitotoxicity. BMC Biol 10:7. https://doi.org/10.1186/1741-7007-10-7
135. Vinet J, van Weering HRJ, Heinrich A et al. (2012) Neuroprotective function for ramified microglia in hippocampal excitotoxicity. J Neuroinflammation 9:27. https://doi.org/10.1186/1742-2094-9-27
136. Rauen T, Wiessner M (2000) Fine tuning of glutamate uptake and degradation in glial cells: common transcriptional regulation of GLAST1 and GS. Neurochem Int 37:179–189. https://doi.org/10.1016/S0197-0186(00)00021-8
137. Harada T, Harada C, Watanabe M et al. (1998) Functions of the two glutamate transporters GLAST and GLT-1 in the retina. Proc Natl Acad Sci U S A 95:4663–4666. https://doi.org/10.1073/pnas.95.8.4663
138. Ishikawa M (2013) Abnormalities in glutamate metabolism and excitotoxicity in the retinal diseases. Scientifica (Cairo) 2013:528940. https://doi.org/10.1155/2013/528940
139. Boccuni I, Fairless R (2022) Retinal Glutamate Neurotransmission: From Physiology to Pathophysiological Mechanisms of Retinal Ganglion Cell Degeneration. Life (Basel) 12. https://doi.org/10.3390/life12050638
140. Rhoads TW, Anderson RM (2020) Alpha-Ketoglutarate, the Metabolite that Regulates Aging in Mice. Cell Metab 32:323–325. https://doi.org/10.1016/j.cmet.2020.08.009

141. Poitry S, Poitry-Yamate C, Ueberfeld J et al. (2000) Mechanisms of Glutamate Metabolic Signaling in Retinal Glial (Müller) Cells. The Journal of Neuroscience 20:1809–1821. https://doi.org/10.1523/JNEUROSCI.20-05-01809.2000
142. Zahra K, Dey T, Ashish et al. (2020) Pyruvate Kinase M2 and Cancer: The Role of PKM2 in Promoting Tumorigenesis. Front Oncol 10:159. https://doi.org/10.3389/fonc.2020.00159
143. Nolan ND, Caruso SM, Cui X et al. (2022) Renormalization of metabolic coupling treats age-related degenerative disorders: an oxidative RPE niche fuels the more glycolytic photoreceptors. Eye 36:278–283. https://doi.org/10.1038/s41433-021-01726-4
144. Tao J, Deng NT, Ramnarayanan K et al. (2011) CD44-SLC1A2 gene fusions in gastric cancer. Science Translational Medicine 3:77ra30. https://doi.org/10.1126/scitranslmed.3001423
145. Shinmura K, Kato H, Igarashi H et al. (2015) CD44-SLC1A2 fusion transcripts in primary colorectal cancer. Pathol Oncol Res 21:759–764. https://doi.org/10.1007/s12253-014-9887-2
146. Ng SK, Wood JPM, Chidlow G et al. (2015) Cancer-like metabolism of the mammalian retina. Clin Exp Ophthalmol 43:367–376. https://doi.org/10.1111/ceo.12462